



Experimental study of the sensitivity of global properties of turbulent bluff body wakes using steady disturbance methods

Vladimir Parezanovic

► To cite this version:

Vladimir Parezanovic. Experimental study of the sensitivity of global properties of turbulent bluff body wakes using steady disturbance methods. Fluid mechanics [physics.class-ph]. Ecole Polytechnique X, 2011. English. NNT: . tel-00670537

HAL Id: tel-00670537

<https://theses.hal.science/tel-00670537>

Submitted on 15 Feb 2012

HAL is a multi-disciplinary open access archive for the deposit and dissemination of scientific research documents, whether they are published or not. The documents may come from teaching and research institutions in France or abroad, or from public or private research centers.

L'archive ouverte pluridisciplinaire **HAL**, est destinée au dépôt et à la diffusion de documents scientifiques de niveau recherche, publiés ou non, émanant des établissements d'enseignement et de recherche français ou étrangers, des laboratoires publics ou privés.

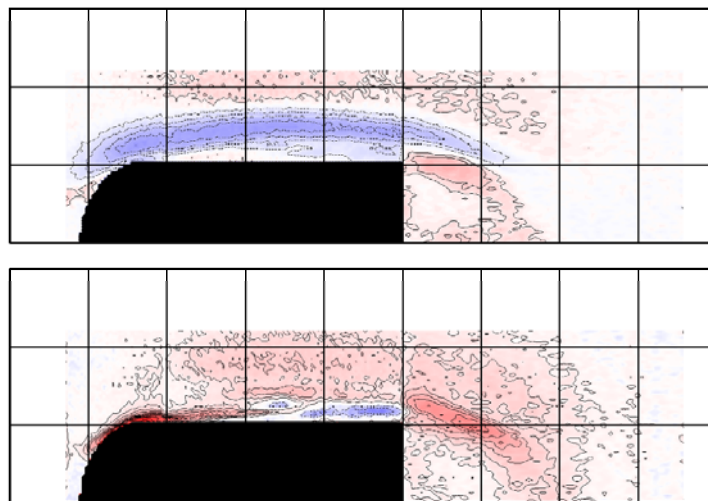
Thèse de Doctorat de l'Ecole Polytechnique
Spécialité: Mécanique des fluides

Fait à
Unité de Mécanique, ENSTA-ParisTech

Présentée par
Vladimir Parezanović

Pour obtenir le grade de
Docteur de l'Ecole Polytechnique

**Experimental study of the sensitivity of global
properties of turbulent bluff body wakes using
steady disturbance methods**



Thèse soutenue le 7 décembre 2011 devant le jury composé de:

Laurent JACQUIN
Bernd NOACK
Patrick HUERRE
José Eduardo WESFREID
Philippe MELIGA
Olivier CADOT

ONERA, Meudon
PPprime, Poitiers
Ladhyx, Palaiseau
ESPCI, Paris
M2P2, Marseille
ENSTA, Palaiseau

Rapporteur
Rapporteur
Examineur
Examineur
Examineur
Directeur de thèse

Za deku.

"When you make the finding yourself - even if you're the last person on Earth to
see the light - you'll never forget it."

-Carl Sagan (1934 - 1996)

Acknowledgements

It is impossible not to begin by acknowledging the immense effort and kindness of my thesis director Olivier Cadot. Olivier has guided me patiently and expertly during these past three years, and I look forward to applying what I learned from him in my future research. Sometimes he played the role of a teacher, filling the gaps in my knowledge, and at other times he was a colleague, discussing ideas and results. These discussions are the most precious memory that I will take away from the whole experience of the doctoral dissertation; it was truly a most wonderful aspect of being a scientist. For all of this I am deeply thankful to Olivier. On the other hand, I wouldn't have had the opportunity to enjoy this experience without several extraordinary people, who made it all possible and who I have the pleasure of mentioning and thanking here. Going back chronologically, it was Patrick Huerre who first welcomed me at Ecole Polytechnique and then showed continuous faith and support for me, throughout my time here. I am also sincerely thankful to Jean-Mari Guastavino who actually made it possible for me to come to France for the first time, visit Ladhyx and meet Patrick. Finally, it all starts with my dear professor Boško Rašuo who's guidance has set me on this path and without which I would not be where I am today. My gratitude for their help and inspiration will never diminish.

I also have the pleasure to thank two of ENSTA's finest: engineer Thierry Pichon and technician Nicolas Baudet. They were always very helpful and supportive with every kind of demand I had. Finally I have to specially thank my colleague and office mate Romain Monchaux, for countless discussions and advice. He is an amazing person and a superb researcher, and I am proud to call him my friend.

Any work would be hard and terrible if there weren't people close to you, who love and support you; in this I was very fortunate to have Malika by my side. Thank you for loving and enduring me.

Most important of all, my love and gratitude go to my wonderful parents. They have sacrificed everything for me and asked nothing in return, except for me to be happy. Mom, dad, I love you.

Vladimir Parezanović

Paris, 15.12.2011.

Abstract

The sensitivity of the global properties of a turbulent wake behind a D-shaped bluff cylinder is investigated experimentally by introducing a much smaller control cylinder of various shapes and diameters as a local disturbance. Hot-wire anemometry and particle image velocimetry are used to obtain local and global measurements of the turbulent wake. Aerodynamic forces acting on the main cylinder are derived from pressure measurements around its perimeter. The results are presented in the form of sensitivity maps of the Strouhal number and base pressure. The sensitivity of global properties is interpreted on the basis of the ability of the control cylinder to change the size of the formation region of the Kármán vortex street mainly through the turbulent properties modification of the perturbed detached shear layer. The corresponding physical mechanisms are discussed with regard to the origins of drag reduction and global frequency modification. The impact of the perturbation on the 3D properties of the wake is investigated through two-point velocity correlation and wake visualization. Bi-stable flow configurations for some positions of the control cylinder are examined.

La sensibilité des propriétés globales d'un sillage turbulent derrière un cylindre en forme de "D" est étudiée expérimentalement. Un petit cylindre de contrôle (de forme et de diamètre variable) est inséré dans le sillage pour créer une perturbation locale. Un ensemble de mesures basé sur de l'anémométrie à fil chaud et vélocimétrie par images de particules est mis en oeuvre pour obtenir des informations locales et globales du sillage turbulent. Les forces aérodynamiques agissant sur le cylindre principal sont dérivées de mesures de pression autour de son périmètre. Les résultats sont présentés sous la forme de cartes de sensibilité du nombre de Strouhal et la pression de base. La sensibilité des propriétés globales est interprétée par la capacité de la perturbation locale à changer la taille de la région de formation de l'allée de Kármán en agissant principalement sur les propriétés turbulentes de la couche de mélange perturbée. Les mécanismes physiques correspondants sont discutés pour interpréter les origines de réduction de traînée et la modification de fréquence globale. L'impact de la perturbation sur les propriétés 3D du sillage est examiné par corrélation de vitesse à deux points et visualisation. Les configurations bi-stable de l'écoulement pour certaines positions du cylindre de contrôle sont étudiées.

Nomenclature

D - main bluff cylinder height

S - main bluff cylinder span

L - perimeter of the main cylinder cross-section

d - control cylinder diameter

U - modulus of mean wind tunnel velocity

U_0 - mean free-stream velocity

u, v - (x, y) components of velocity

ω_z - vorticity in xOy plane

f - global mode frequency

δ_{min} - shear layer thickness at the trailing edge

\vec{n} - unit vector normal to the bluff-body surface

Re - Reynolds number, $\frac{DU_0}{\nu}$

St - Strouhal number, $\frac{fD}{U_0}$

L_b - mean recirculation bubble length

D^* - mean detached shear separating distance (bubble height)

C_{pb} - base pressure coefficient

C_d - drag coefficient, $\frac{2F_d}{\rho v^2 A}$

C_l - lift coefficient, $\frac{2F_l}{\rho v^2 A}$

$C_{pb(rms)}$ - rms of the base pressure coefficient

$C_{l(rms)}$ - rms of the lift coefficient

Δp_{head} - differential pressure at the head of the main cylinder

Δp_{base} - differential pressure at the base of the main cylinder

p_{ref} - reference static pressure

r - linear correlation coefficient

\tilde{f} - global frequency change, $\frac{f-f_n}{f_n}$

$X_{\overline{v'^2}Max}, X_{\overline{u'v'}Max}, X_{\overline{u'v'}Min}$ - streamwise locations of Reynolds stresses extrema

$\delta_{\overline{v'^2}}, \delta_{\overline{u'v'}}$ - quality definition of Reynolds stress extrema

Contents

| | |
|--|-----------|
| Contents | 7 |
| 1 Introduction | 9 |
| 2 Experimental setup | 19 |
| 2.1 Test facility | 19 |
| 2.2 Experimental geometry | 22 |
| 2.2.1 Main bluff cylinder | 22 |
| 2.2.2 Control cylinders | 23 |
| 2.2.3 Displacement of the control cylinder | 25 |
| 2.3 Measurements and instrumentation | 26 |
| 2.3.1 Local velocity measurements | 26 |
| 2.3.2 PIV measurements | 27 |
| 2.3.3 Pressure measurements | 29 |
| 2.4 Experimental problems | 30 |
| 2.4.1 Ambient temperature variations | 30 |
| 2.4.2 Shear layer asymmetry | 32 |
| 3 Natural flow around the bluff cylinder | 33 |
| 3.1 Boundary layer evolution | 33 |
| 3.2 The mean natural wake and the dynamics in the wake | 39 |
| 4 Wake with a circular control cylinder | 43 |
| 4.1 Mapping of global properties | 43 |
| 4.1.1 Global frequency change | 43 |
| 4.1.2 Base pressure and drag | 44 |
| 4.1.3 Effects on lift | 48 |
| 4.1.4 Additional sensitivity maps for $d = 3mm$ | 51 |
| 4.2 Turbulent wake modification with a control cylinder at $x_c/D = 0.4$ | 52 |
| 4.2.1 Local velocity measurements | 52 |
| 4.2.2 Mean flow measurements | 54 |

CONTENTS

| | | |
|----------|---|------------|
| 4.2.3 | Reynolds stress envelope | 56 |
| 4.3 | Turbulent wake modifications with a control cylinder at $y_c/D = 0$ | 64 |
| 4.3.1 | Mean wake and Reynolds stress measurements | 64 |
| 4.4 | The mechanisms of wake modification | 68 |
| 4.4.1 | Global frequency selection | 68 |
| 4.4.2 | Global mode structure and drag reduction | 76 |
| 4.4.3 | Summary of the observed flow configurations | 83 |
| 5 | Bi-stable flow regime and 3D effects | 85 |
| 5.1 | Fluctuations of base pressure and lift | 85 |
| 5.2 | Bi-stable flow regime | 87 |
| 5.3 | Hysteresis of shear layer re-attachment | 96 |
| 5.4 | Spatial correlations of hot-wires local measurements | 96 |
| 5.5 | Effects on the 3D properties of the wake | 98 |
| 6 | Sensitivity maps | 109 |
| 6.1 | Anatomy of the sensitivity maps | 109 |
| 6.2 | Impact of the control cylinder size and the Reynolds number | 114 |
| 6.3 | Impact of control cylinder shape | 114 |
| 6.4 | Extended sensitivity map for $d = 1mm$ circular cylinder | 119 |
| 7 | Conclusion | 125 |
| A | Jet | 129 |
| B | Trailing edge flap | 133 |
| C | End plates | 139 |
| | Bibliography | 145 |

Chapter 1

Introduction

The problem of a separated flow created by a bluff body at high Reynolds numbers is one of the oldest problems in fluid dynamics. A major consequence of such a strong flow separation is a high drag coefficient caused, for the most part, by a wide wake and a large difference between the head and base pressure. This is accompanied by the phenomenon of vortex shedding in the form of a Kármán vortex street.

The question of predicting drag in such flows is of a great practical importance. This has inspired attempts to create a mathematical formulation, starting perhaps with Newton, who formulated the force on a flat plate, imposed by a stream of particles moving in a perpendicular direction to the plate, shown in figure 1.1(a). With the assumption that the entirety of momentum of the particles is absorbed by the plate, Newton obtained a drag force coefficient of $C_d = 2$. However, the actual flow field and pressure distribution in an incompressible flow is very different and yields a drag coefficient of $C_d = 1.1$. In 1896, Kirchhoff published his model (1869) based on the free-streamline method of Helmholtz, which included important effects of flow separation: detached shear layers and a low base pressure (figure 1.1b). This model gave a drag coefficient of $C_d = 0.88$, with the base pressure coefficient fixed to $C_{pb} = 0$. In actual flows however, the wake does not extend to infinity as in Kirchhoff's model, but is closed by laminar or turbulent diffusion. As a consequence, the base pressure coefficient is always negative, ie. lower than in the model, and thus, the real drag of a flat plate is higher. An improvement in obtained drag and base pressure coefficients can be obtained by the use of the model of Riabouchinsky (1921), which introduces an "image body" as the wake closure (figure 1.1c). This, in turn, introduces the length of the wake and the height of the wake as values which depend on the base pressure coefficient. This relationship is one of the major ingredients of the bluff-body problem.

In the past century, the problems of a bluff body has mostly been addressed by the example of a circular cylinder. The simplicity and unquestionable practical importance of this shape made it very popular for experimental investigations throughout a large range of Reynolds

1. INTRODUCTION

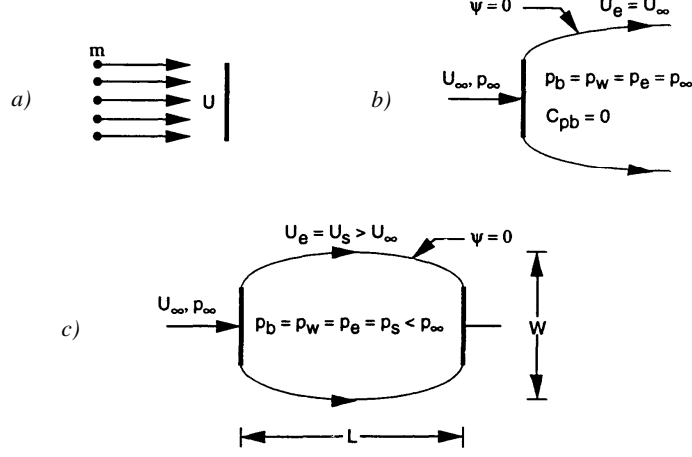


Figure 1.1: Mathematical models of a separated flow in a bluff-body wake by (a) Newton, (b) Kirchhoff and (c) Ryabouchinsky.

numbers. The compiled results for the base pressure by [Roshko \(1993\)](#) in figure 1.2 and a recent law of Strouhal and Reynolds number relationship by [Fey *et al.* \(1998\)](#), shown in figure 1.3 illustrate this. An open question still remains regarding the true nature of the proposed $St - C_d$ relationship ([Ahlborn *et al.*, 2002](#); [Roshko, 1954a](#)).

However, the circular cylinder has an additional complexity built into its simple and elegant shape: a boundary layer detachment which is not fixed, but heavily dependable on the flow conditions and other factors. This confounds the issue by adding a degree of freedom into the problem, and is one of the reasons why we have opted to use a D-shaped cylinder in our study presented in this thesis. An excellent compilation of experimental and theoretical work on the circular cylinder flow and control methods can be found in [Zdravkovich \(1997\)](#) and [Zdravkovich \(2003\)](#).

On the issue of bluff-body wake control, one of the most investigated methods is the use of the splitter plates, which is interesting since it prevents the coupling of the free shear layers and so inhibits the vortex shedding, in an effort to reduce drag of the main cylinder. Some of the studies of splitter plates have been done by [Roshko \(1954b\)](#), [Bearman \(1965\)](#), [Apelt *et al.* \(1973\)](#) and [Apelt & West \(1975\)](#). The base pressure is drastically increased and consequently the drag reduced (by almost 30%) and the global frequency can be affected by about +30% to -50% depending on the cylinder's shape ([Apelt & West, 1975](#))(figure 1.4). Another approach is to place a rod or a plate upstream of the bluff body ([Igarashi & Terachi, 2002](#); [Lee *et al.*, 2004](#); [Prasad & Williamson, 1997](#); [Tsutsui & Igarashi, 2002](#)). The main cylinder is then in the wake of the smaller cylinder, and the drag reductions are reported taking into account the drag of both cylinders.

The seminal work of [Strykowski & Sreenivasan \(1985, 1990\)](#) investigates the flow around

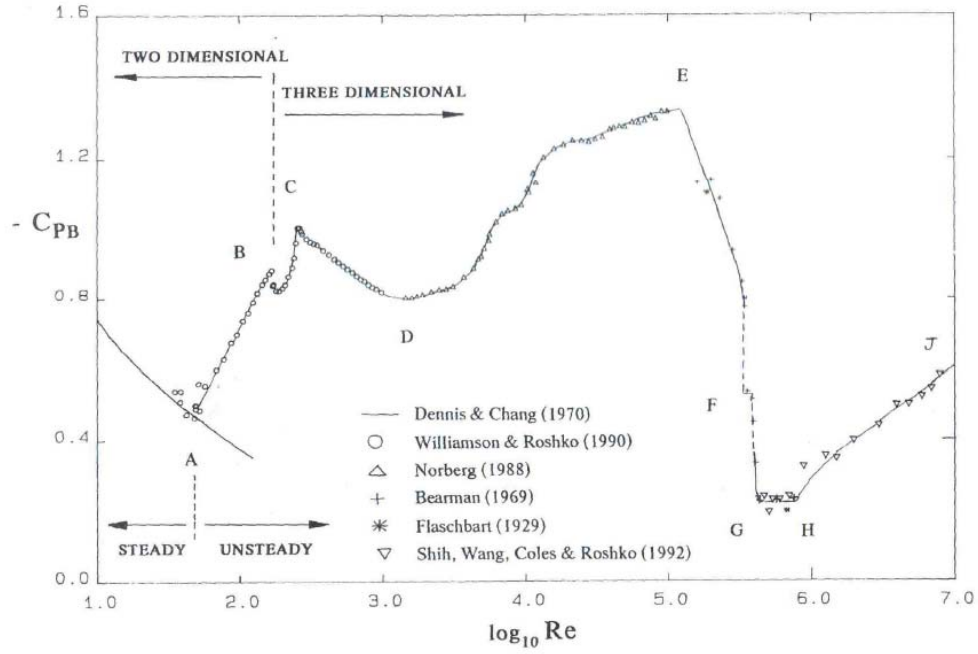


Figure 1.2: Compilation of experimental results on the base pressure coefficient of a circular cylinder with respect to the Reynolds number (Roshko, 1993).

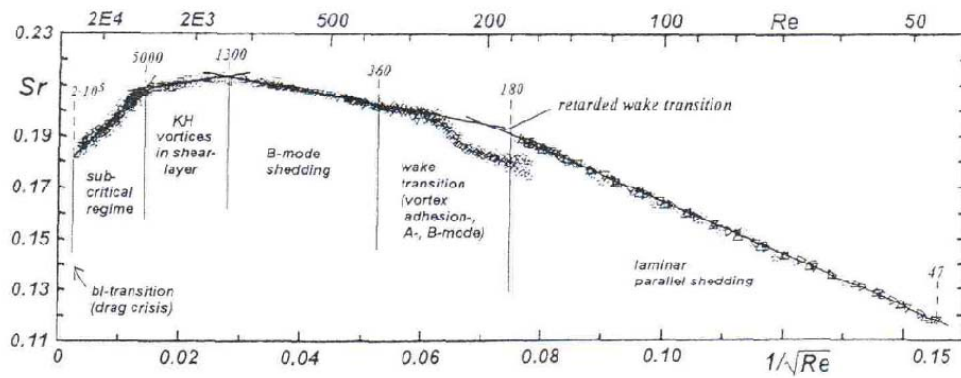


Figure 1.3: Experimental results on the Strouhal number of a circular cylinder with respect to the Reynolds number (Fey et al., 1998).

1. INTRODUCTION

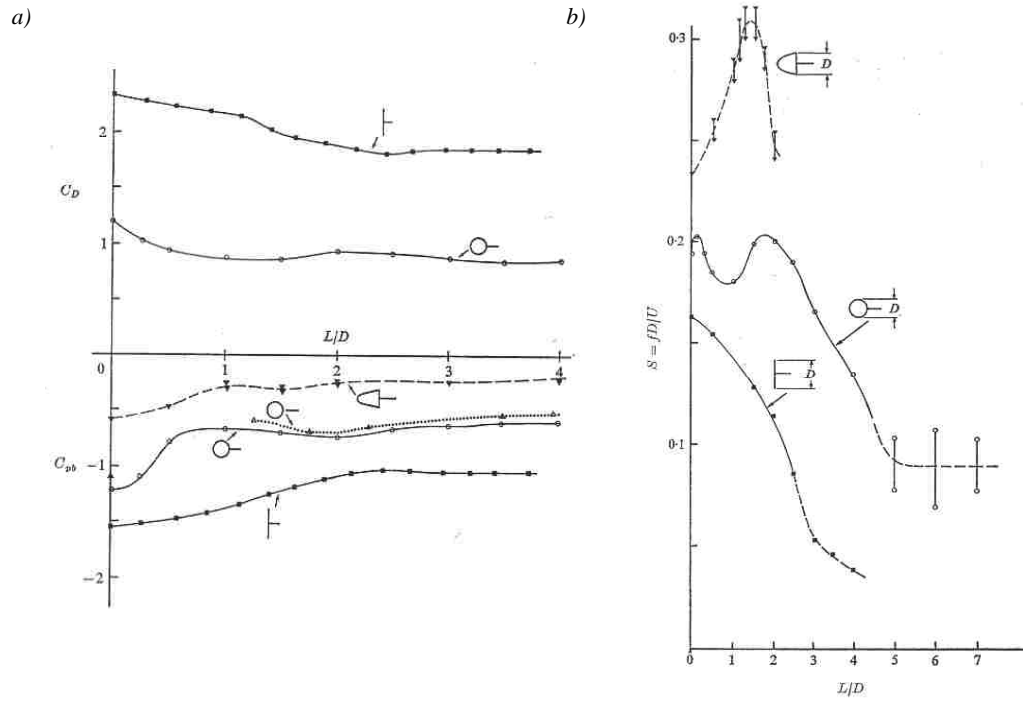


Figure 1.4: Effects of the splitter plates on (a) base pressure and drag, and (b) Strouhal number, for different bluff body shapes, by Apelt & West (1975).

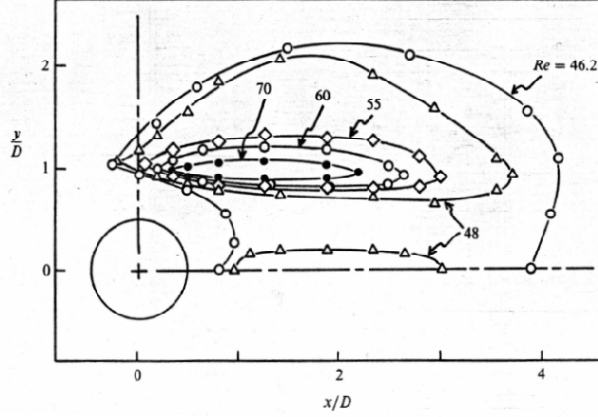


Figure 1.5: Sensitivity map of Strykowski & Sreenivasan (1990) at low Reynolds numbers.

a circular cylinder disturbed by a much smaller secondary cylinder in the neighborhood of the first instability threshold. For certain locations of the secondary cylinder the authors find a wake stabilization effect systematically accompanied by a global frequency reduction that could go toward the complete unsteadiness suppression, shown in figure 1.6(b). Their results are represented in terms of spatial sensitivity map (figure 1.5) showing the regions around the primary cylinder in which the global mode instability is mostly affected. They proposed a stabilization mechanism based on the interaction and modification of the shear layers in the frame of the model of Gerrard (1966), although the physical mechanism involves vortex shedding at larger Reynolds numbers. This model takes into account Roshko's universal Strouhal number (1954b) $S^* = \frac{d'}{U_s}$ (see figure 1.7a) and Gerrard's notion of the dependence of the formation region length on the equilibrium of the detached shear layer entrainment and replenishment of fluid into the recirculation region (see figure 1.7b).

Since then, numerous studies have investigated this flow at about the same Reynolds number but only for the most effective positions of the control cylinder that suppress vortex shedding. The numerical simulations of Mittal (2001) and Mittal & Raghuvanshi (2001) at $Re = 100$ are in fairly good agreement with the Strykowski & Sreenivasan (1985, 1990) results. The authors argued that a favorable pressure gradient locally introduced by the control cylinder might stabilize one of the shear layers. The consequences of this passive control on drag and lift have been studied numerically and experimentally by Dalton *et al.* (2001) for larger, but still moderate Reynolds numbers of 100 to 3000 where mean drag and fluid force fluctuations are found to be reduced. The recent numerical study of Yildirim *et al.* (2010) at $Re = 80$ also confirms the force reduction. In addition, it shows how the vorticity introduced by the secondary cylinder in the vicinity of the shear layers of the primary cylinder affects vortex dynamics and vortex arrangements in its wake. Kuo *et al.* (2007) have performed numerical investigation of a configuration with two small cylinders in the wake at Re from 80 to 300.

1. INTRODUCTION

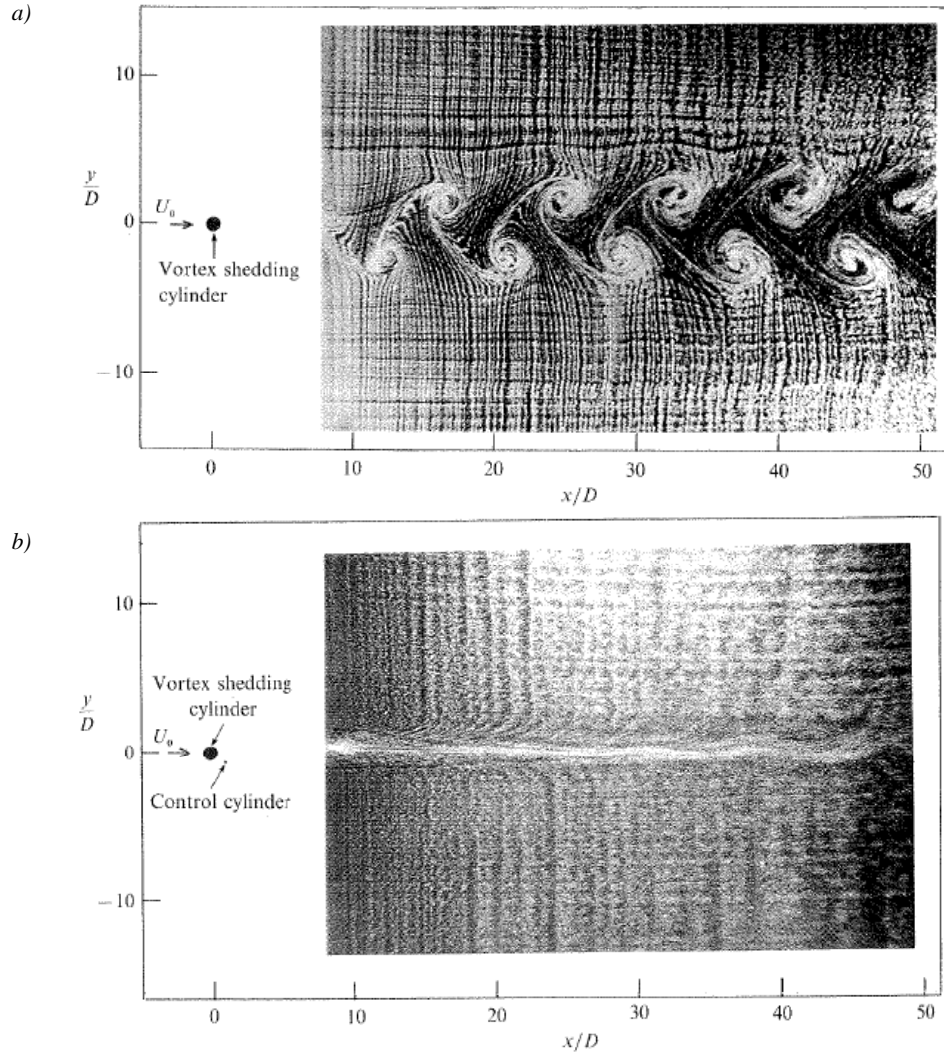


Figure 1.6: Hydrogen-bubble picture of (a) vortex shedding behind a circular cylinder at $Re = 80$, and (b) vortex shedding suppression using a control cylinder of $D/d = 7$ (Strykowski & Sreenivasan, 1990).

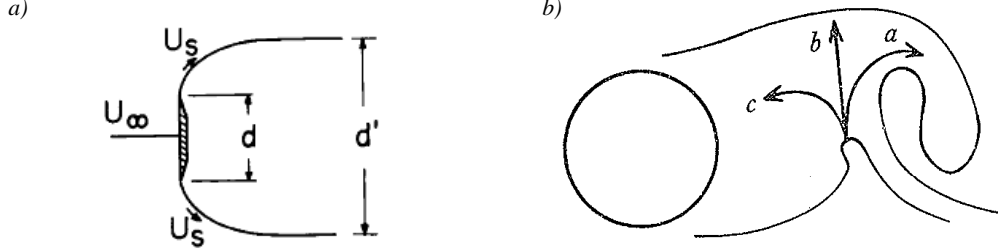


Figure 1.7: Free shears separating distance d' by Roshko (1954b) (a), and the filament-line sketch of the formation region fluxes by Gerrard (1966).

They also observed wake stabilization with associated reduction in fluctuating aerodynamic forces. In both Strykowski & Sreenivasan (1990) and Kuo *et al.* (2007), flow displacement from the outside flow into the recirculation region due to the presence of the control cylinder(s) is observed, which will be shown as an important feature in our interpretation of drag reduction.

On the theoretical background, the effects of a local perturbation on the global mode of 2D wakes (Chomaz, 2005; Hill, 1992) has received much attention since the work of Giannetti & Luchini (2007); Luchini *et al.* (2008). For Reynolds number close to the first instability ($Re < 150$), the computation of the direct and adjoint global modes of the base flow is able to retrieve the spatial structure of the sensitivity (figure 1.8) of the Bénard von Kármán instability obtained experimentally by Strykowski & Sreenivasan (1985, 1990). Recent theoretical developments (Luchini *et al.*, 2008, 2009; Marquet *et al.*, 2008; Pralits *et al.*, 2010) have shown that the basic flow modification introduced by the local perturbation represents the dominant contribution to the global mode sensitivity. The theory offers new tools for aerodynamicist to predict optimal location for flow modification. However, at the present stage it only concerns flows at low Reynolds numbers near the threshold of a global instability. For the numerous industrial applications of large Reynolds flows, one may ask whether similar theoretical development can be made for flows that are still governed by global mode dynamics. Such attempts for compressible flows have been successfully investigated by Crouch *et al.* (2009), which gives hopes for this research field.

While splitter plates are generally very intrusive, small control cylinders, similar to local 2D steady disturbances, lead to the same order of magnitude for the global quantities modifications. Experimentally, the method of introducing a small control cylinder is very successful in reducing aerodynamic forces for large Reynolds number flows (Sakamoto & Haniu, 1994; Sakamoto *et al.*, 1991; Shao & Wei, 2008). Sakamoto investigated in detail the method applied to square and circular primary cylinders for $Re > 10,000$. Similarly to Strykowski & Sreenivasan (1985, 1990), their results are displayed in sensitivity maps of global quantities such as drag (figure 1.9a), lift (figure 1.9b), and Strouhal number. For certain positions of the control cylinder the drag can be reduced by up to 40% for the circular cylinder and 30% for the square cylinder and the global

1. INTRODUCTION

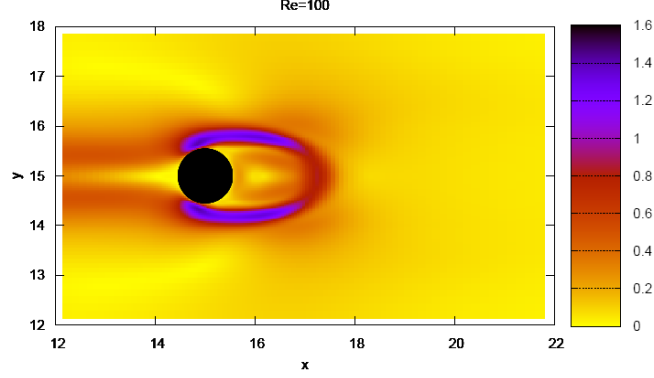


Figure 1.8: Structural sensitivity of the periodic wake at $Re = 100$ by (Luchini *et al.*, 2008).

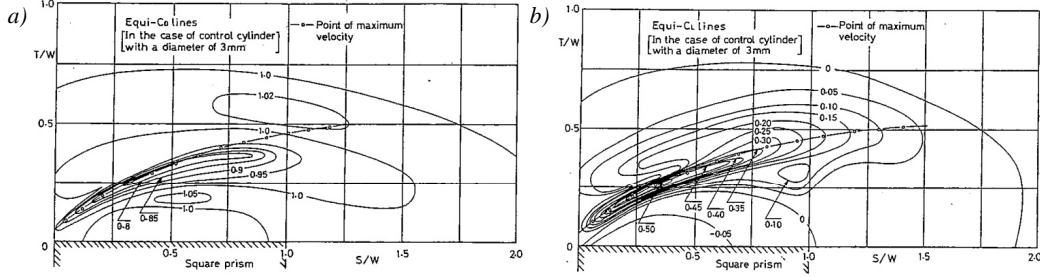


Figure 1.9: Experimental sensitivity maps of drag (a) and lift (b), for a square prism with a circular control cylinder at high Re , obtained by Sakamoto *et al.* (1991).

frequency can be either increased or decreased. The differences between the two geometries are essentially due to the separation point displacements, which are only possible for the circular cylinder. When the separation points are fixed, which is the case for the square cylinder, the maximum reduction occurs when the control cylinder is located near the outer boundary of the separated shear layer in the vicinity of the bluff body. This position at large Re is very similar to the position for shedding suppression observed at low Reynolds number by Strykowski & Sreenivasan (1990).

In the works of Sakamoto & Haniu (1994); Sakamoto *et al.* (1991), the wake topologies have not been studied in detail and some positions of the control cylinder related to the region inside the recirculating bubble have not been explored. In order to avoid the effect of flow reattachment on the primary bluff body, Thiria *et al.* (2009) investigated the controlled wake at large Reynolds number of a "D" shaped cylinder. Their study was restricted to the position of the control cylinder for which drag is substantially reduced. They found the maximum of the global mode spatial structure, called "the global mode envelope" in Zielinska & Wesfreid (1995), to be strongly inhibited and shifted downstream (figure 1.10). Similarly to Sakamoto

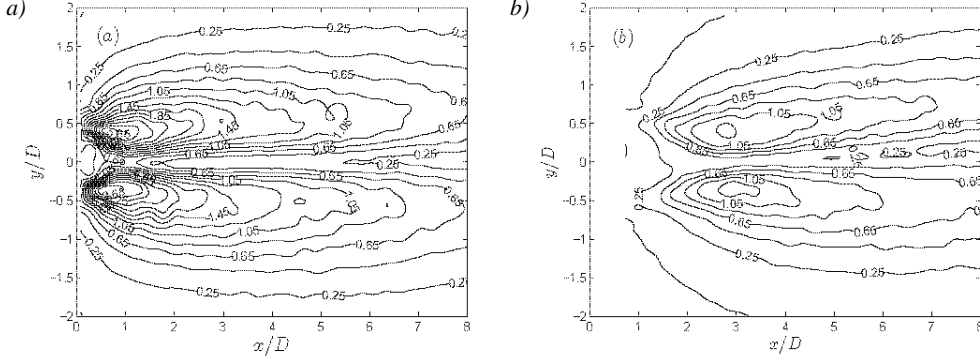


Figure 1.10: Modification of the global mode envelope by a circular control cylinder obtained by Cadot *et al.* (2009). Envelope of the fundamental synchronization frequency is given in (a) for the natural wake and (b) for the controlled wake.

et al. (1991), the effect on the base pressure of one and two control cylinders in the "D" cylinder wake have been investigated by Cadot *et al.* (2009). For the optimum position of the control cylinder that produces the maximum increase of base pressure (reduction of drag), it is found that there is an optimal position for a second control cylinder, which is able to further increase the base pressure (to additionally reduce drag). The global mode envelope is shifted downstream more than in the case of one control cylinder.

This doctoral thesis aims at clarifying the effect of the local 2D disturbance in a turbulent wake of a cylinder, in order to understand the origin of the global properties sensitivity. Our goal is to reveal the nature of mechanisms responsible for the modification of the global mode and its relationship to the mean flow modification. The presented experiments feature (among other) the use of a small control cylinder, which can be associated to the term "disturbance". We hope that these results will be especially useful for theoretical and numerical modeling of wake sensitivity at high Reynolds numbers. We will focus on the modifications of the mean wake, as well as on the impact of the control cylinder on the spatial structure of the Reynolds stresses. The 3D properties of the disturbed turbulent wake are investigated through two-point velocity correlation and wake visualization. Most importantly, we try to answer the following questions: why is the global mode spatial structure shifted downstream and damped? How to explain the frequency change and the drag reduction? How do these effects behave, as the control cylinder diameter decreases? What are the consequences of the steady 2D disturbance on the 3D properties of the wake?

Some chapters in this thesis have been published (as presented here or in modified form) in several publications: Parezanović & Cadot (2009a), Parezanović & Cadot (2009b) and Parezanović & Cadot (2011).

The structure of this thesis will be the following: we will first present the experimental setup and measurement equipment in chapter 2. The study of the natural flow will be pre-

1. INTRODUCTION

sented in chapter 3. Wake modification by a circular control cylinder will be presented in chapter 4, in terms of global mode frequency measurements, PIV measurements as global mode envelope characterization and base pressure measurements. As a conclusion of this chapter we will propose some physical mechanisms that are involved in the sensitivity of the global mode envelope and frequency to the presence of the 2D disturbance. A drag reduction mechanism is also described. Chapter 5 will describe circular control cylinder influence on the fluctuating aerodynamic forces, the phenomenon of the bi-stable flow configuration and give characterization of the 3D features of the wake by two-point velocity correlation in the spanwise direction. Chapter 6 will give a complete compilation of sensitivity maps for various types and sizes of control cylinders and Reynolds numbers. The thesis finalizes with a brief recapitulation and conclusion in section 7.

Chapter 2

Experimental setup

2.1 Test facility

The experimental test facility is an Eiffel type, open-circuit wind tunnel. The tunnel is 8.835m long from the intake to the outlet. All segments of the wind tunnel have a square cross-section, similar to the intake shown in figure 2.1(a). Only outlet has a circular cross-section since it houses the fan shown, in figure 2.1(b). Figure 2.1(c) shows the experimental area enclosed in a wooden chamber. The chamber dimensions are $2.03m \times 1.56m \times 1.5m$, and it allows complete access to the experiment via doors on each side. These doors are closed and sealed during the wind tunnel activity, allowing the chamber to maintain constant pressure and temperature environment in and around the test section. Figure 2.1 also shows the test section (d), with some of its details: the main bluff cylinder (e), equipment for the control cylinder including the support frame (f) and the displacement consoles (g), pressure measurement electronics and tubing (h), and support and displacement equipment for the hot-wire probes (i). Depending on the experiment, the test section may contain imaging cameras for PIV acquisitions (not seen here), and mounted on the roof is an optical table (j) used for precise positioning of the laser sheet optics and mirrors (not shown). Complete layout and dimensions of the wind tunnel are given in the manufacturer's technical drawing in figure 2.2, and a more detailed description of the experimental geometry itself will be given in the next section.

The wind tunnel is capable of producing speeds up to $33m/s$; with less than 0.3% of turbulence intensity, and velocity homogeneity of $\pm 0.4\%$. The velocity in the wind tunnel is set by controlling the revolutions of the electrical fan which is creating the under-pressure at the outlet, and are ranging from 0 to 1506 (*RPM*). As a standard velocity of the experiments, we have selected the setting of 400 (*RPM*). This setting gives a sufficiently high Reynolds number of the experiment, while allowing us to maintain reasonable seeding quality for the PIV measurements. Tunnel velocity a linear function of the revolutions per minute of the fan, and is given in the figure 2.3(a), based on manufacturer's specifications.

2. EXPERIMENTAL SETUP

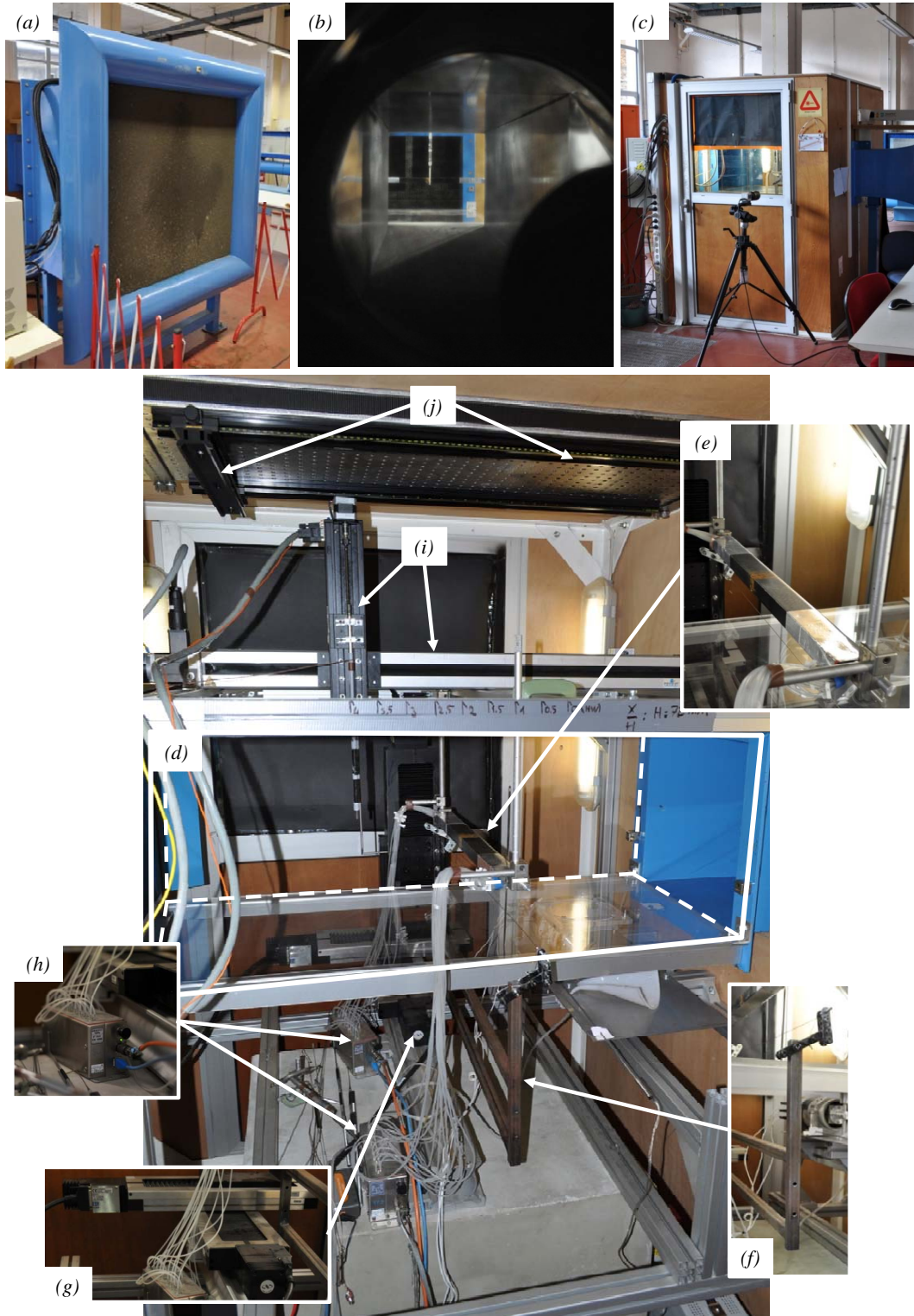


Figure 2.1: Wind tunnel and details of the experimental setup.

2. EXPERIMENTAL SETUP

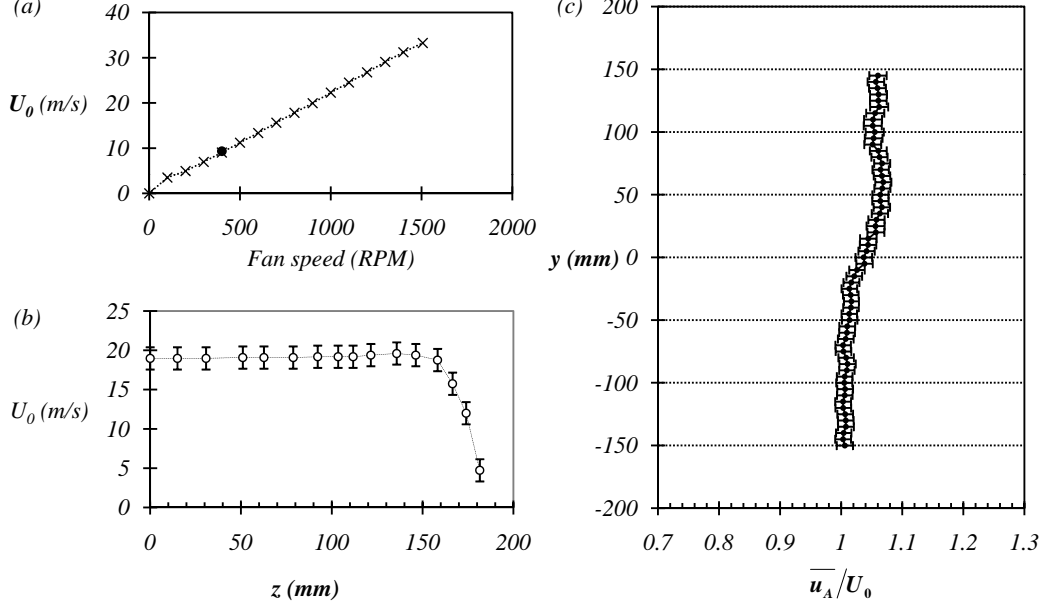


Figure 2.3: The wind tunnel velocity information: (a) manufacturers data on the mean velocity versus the control input; (b) experimentally measured spanwise velocity profile and (c) experimentally measured vertical velocity profile.

The test section has a square cross-section of $400\text{mm} \times 400\text{mm}$, with open sides. Its length, from the inlet to the outlet, is 960mm . The spanwise profile of velocity $U(z)$ is shown in figure 2.3(b). We can see that the flow is uniform over a length of 300mm , after which the velocity decreases to zero on a typical length of 20mm . The vertical profile of velocity at 400rpm speed setting is shown in figure 2.3(c). The streamwise velocity is changing by about 2.5% across the height of the test section, and it is slightly lower in the bottom part and slightly higher in the upper half of the tunnel. This is due to a temperature gradient in the air in front of the intake of the tunnel.

2.2 Experimental geometry

2.2.1 Main bluff cylinder

The primary cylinder (shown in figure 2.4b) has a semi-circular leading edge which continues into a rectangular aft section, for a combined length of $2D = 50\text{mm}$. The diameter of the semi-circle, and thus the height of the main cylinder, is $D = 25\text{mm}$. This is the characteristic length of the experiment, and will be used to define Reynolds and Strouhal numbers. It can be noted that contrary to slender bodies, for bluff bodies this height is much more important than the cord length, since it (among other factors) determines the size of the wake. Therefore,

this elongated "D" shape has been chosen in order to have a constant height of the wake, for a wide range of Reynolds numbers. This requirement is fulfilled by the fact that the flow is detached at the blunt trailing edge, and that the shear layers are parallel before roll-up. This will be described in detail in section 3.

As shown in figure 2.4(a), the main cylinder is fixed at the edges of its span to the floor of the wind tunnel. The span of the body is $S = 600mm$. Therefore, in the spanwise direction, the edges of the main cylinder go beyond the width of the test section.

In the streamwise direction, the leading edge of the main cylinder is located at $\approx 1/5$ of the test section length from the inlet. Vertically, it is exactly in the middle of the test section. Before each experiment, it is thoroughly verified that the span of bluff cylinder is parallel to the upper and lower wall of the test section, and also that it is at an angle of attack of $\alpha = 0^\circ$ with regard to the incoming flow.

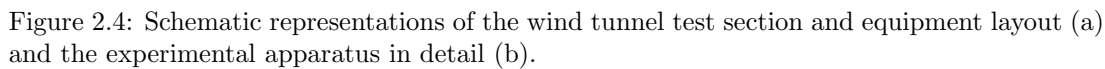
The main cylinder is made of metal, with highly polished surfaces. The inside is hollow, allowing access to ports for pressure measurements. The tubing that is connecting the ports to the measurements devices is running inside the cylinder, starting from both edges and finishing at the center section. As can be seen in figure 2.4(b), the pressure measurement ports are located at the center span cross-section. Figure 2.5 shows in detail the number and distribution of pressure ports around the perimeter of the main cylinder center section. Each port is connected to the measurement device with a plastic tube of $\phi 3mm$ and an average length of $1.5m \pm 5cm$.

2.2.2 Control cylinders

The requirements of the experiment dictate that the control cylinder needs to be moved easily between various positions downstream of the main cylinder. It is also imperative that while changing the position, the control cylinder doesn't change its orientation relative to the main cylinder. Therefore, the control cylinder is connected by a rigid supporting frame to a displacement console. The supporting frame does not obstruct the flow, since it is located on the sides of the tunnel, outside of the steady flow, and below the tunnel floor. Some details of this setup can be seen in figure 2.4(a).

The common span of all types of control cylinders used is $s = 800mm$. Due to different thickness and rigidity of the control cylinders, it was necessary to be able to stretch them in the spanwise direction, in order to eliminate slacking or vibrations. At the same time it was verified that the cylinders were not overstretched which could lead to deformations in the opposite sense. Additionally, absence of flow induced vibrations was verified visually, usually by the aid of a high speed camera used for the PIV acquisitions. Figure 2.6 shows the different cross-section shapes and sizes of the control cylinders.

The circular control cylinders were usually a metal wire of a specific diameter, except in the case of the $d = 0.1mm$ cylinder, which was made out of a nylon string. The flat plate control cylinder is a metal plate of $1mm \times 3mm$, with slightly chamfered edges, the effect of which can be neglected. The experiments with the flat plate required a change in angle of attack of the



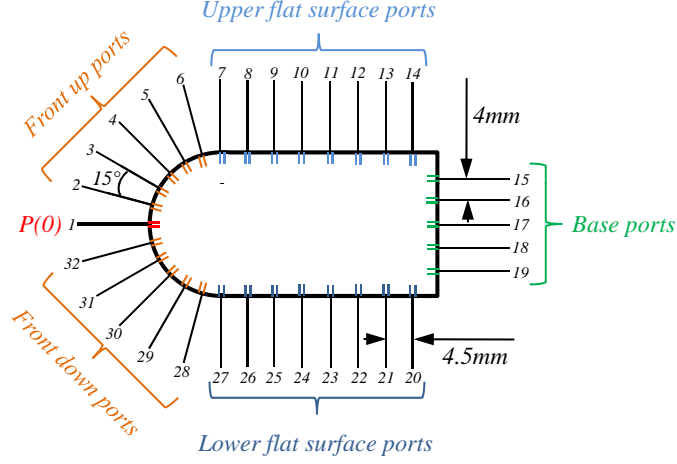


Figure 2.5: locations, grouping and numbering of the pressure ports on the main cylinder.

flat plate. This was done visually, since there was no possibility of measuring accurately the angle of the plate. In addition to this, the plate itself was slightly undulated along its span, and all of this has to be taken into account when analyzing the results of these experiments.

2.2.3 Displacement of the control cylinder

The supporting frame of the control cylinder is connected to three Newport (M-)MTM long travel consoles, which are controlled by the Newport Motion Controller ESP301. These consoles are used to accurately position the control cylinder in Ox and Oy directions. The Oz direction hasn't been used in our experiments, since both the main and secondary cylinders are $2D$. The displacement console has accuracy better than $0.1mm$.

The experiments are performed by moving the control cylinder through a set of pre-determined positions (x_c, y_c) , and measuring local velocity in the wake and pressure distribution on the main cylinder, for each position. The area of interest is shown in figure 2.4(b) as the green rectangular area, which extends $1.8D$ downstream from the base of the bluff body, and $\pm 1.1D$ above and below the horizontal axis of symmetry of the bluff body. The control cylinder is displaced in $0.04D$ ($1mm$) steps in the horizontal direction, and in $0.02D$ ($0.5mm$) steps in the vertical direction, except when noted otherwise. The origin $(x_c = 0, y_c = 0)$ is defined as the intersection between the horizontal axis of symmetry and the trailing edge of the bluff cylinder.

The movement sequence of the control cylinder is as follows: from the starting position $(x_c = 0, y_c = -1.1D)$ the control cylinder is moved through 111 steps in the $+Oy$ direction then by 1 step in $+Ox$ direction, continued by 111 steps in the $-Oy$ direction and finally by 1 step in $+Ox$ direction. This pattern is repeated so to cover the area of interest of $1.8D \times 2.2D$, with a resolution of 45×111 positions of the control cylinder. At each position, the control cylinder

2. EXPERIMENTAL SETUP

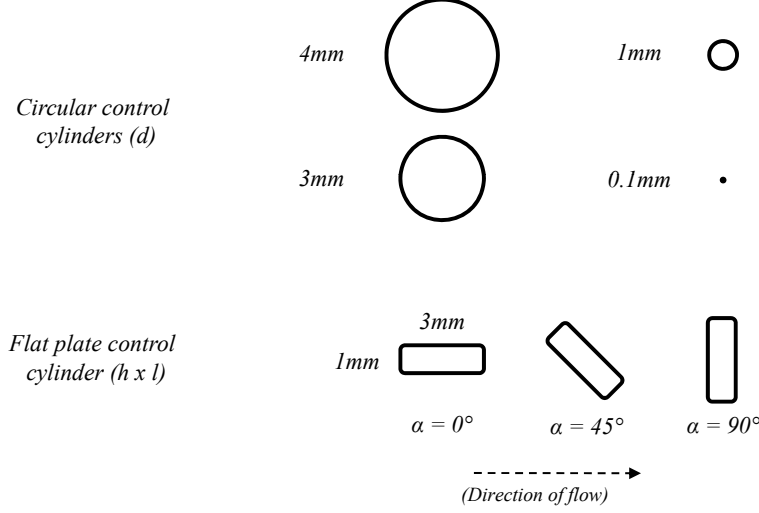


Figure 2.6: Sizes and shapes of the control cylinders used in the experiments.

remains stationary, for a specified time interval, during which measurements are obtained. The whole experiment, taking into account short delays between the starting and stopping of the movement (for each step) and the measurements, lasts 48 hours.

When it is necessary to place the control cylinder at a single, specific position, it is done by placing it first at the origin, then moving it relatively from the origin position to the desired location. This ensures that the obtained location is not the absolute position in space with respect to the frame of the wind tunnel and the test section, but that it is accurate with respect to the exact position of the main cylinder, which is crucial. This was necessary because both the main cylinder and the control cylinders had to be dismantled and taken out frequently in order to make the wind tunnel available for other users.

2.3 Measurements and instrumentation

The experimental data presented in this thesis was obtained from three principal sources: hot-wire anemometry, differential pressure measurements and PIV acquisitions. The following sections will describe in detail the main measurement techniques and the post-processing of obtained data.

2.3.1 Local velocity measurements

Hot-wire measurements of local velocity in the wake is an accurate and unobtrusive way of recording the frequency of the global mode. The frequency is measured from the frequency of

the velocity fluctuations characteristic of the Kármán vortex street. The hot-wire probes are placed so that the passing of vortices from the vortex street is clearly registered.

Figure 2.4(b) shows the placement of the four hot wire probes, marked A0 through A3, in the wake. The hot wire probes measure the modulus of local velocity in the xOy plane and will be denoted as $u_{Ai}(t)$, where i refers to the label of the hot wire probe. They are all located at $x = 6D$ downstream of the trailing edge of the main cylinder, and at the same vertical level as its lower horizontal edge, at $y = -0.5D$, or its upper horizontal edge at $y = +0.5D$. In the spanwise direction, they are located at $z = -2D$, $z = 0$ and $z = +2D$. Not all of these positions have been used in every experiment. Therefore, for each presented experiment we will define the locations of the hot-wire probes for that particular instance, by referring to the labeling convention of Ai .

We use two DISA Type 55M10 and two DANTEC constant temperature anemometry units, connected to a PC with Labview software, as the control platform, to perform simultaneous acquisition of the signals. The hot-wire probes are DANTEC, and use an overheat ratio of 1.5. For more details about hot-wire anemometry theory please refer to Lomas (1986).

The acquisition of each velocity signal is performed at a rate of $1kHz$ during the acquisition period t_{acq} . The acquisition period is usually 30s or 60s. The power spectrum $P_{u_{Ai}}(f) = \frac{1}{2\pi} \int < u_{Ai}(t)u_{Ai}(t+\tau) >_T \exp(-2\pi if\tau) d\tau$, computed from the velocity time series, is averaged over a window of $T = 4$ seconds. Hence the frequency resolution of the spectra is $\Delta f = 0.25Hz$. In order to find the frequency of the global mode, we use the peak detection subroutine, based on an algorithm that fits a quadratic polynomial to sequential groups of data points, where a group of points corresponds to a bandwidth of $10Hz$. Strouhal number is the calculated as $St = \frac{fD}{U_0}$.

In order to characterize the 3D structure of the wake, spatial correlations are obtained from cross correlations between the local velocity measurements. The measurements of hot wire probes Ai are used to compute three spanwise correlation coefficients: $r_{[0-1]}$, $r_{[1-2]}$, $r_{[0-2]}$, and a vertical correlation coefficient $r_{[1-3]}$ defined as:

$$r_{[i-j]} = \frac{\overline{u'_{Ai}u'_{Aj}}}{\sqrt{\overline{u'^2_{Ai}} \overline{u'^2_{Aj}}}}, \quad (2.1)$$

where primes denote the fluctuating part of the velocity following the classical Reynolds decomposition $X'(t) = X(t) - \overline{X}$. This notation will be used throughout the paper.

2.3.2 PIV measurements

Particle Image Velocimetry is used to visualize and obtain the velocity field around the bluff body and the control cylinder. A useful review of PIV principles and techniques may be found in Adrian (1991). Two separate PIV systems were used: a standard and a high-speed system. Both have been engaged into revealing the mean and fluctuating wake topology near the base

2. EXPERIMENTAL SETUP

of the main cylinder. The standard setup was also used in visualization experiments of the 3D properties of the wake in the horizontal plane (xOy) behind the main cylinder.

The standard system is comprised of a Litron LP4550, dual pulse 200mJ Nd:YAG laser, and a Lavision Imager PRO camera. The setup acquires images at a rate of 11Hz, and Lavision software DaVis 7 has been used to calculate the velocity fields. The vector calculation is done using single-pass, dual frame cross-correlation on constant window size. The interrogation window size is 32×32 pixels, and the entire image is 1600×1400 pixels. The time delay between the two frames is $75\mu s$, for both experiments. Each acquisition records 200 image pairs.

The Hi-speed system uses a Pegasus dual pulse laser with a wavelength of 527nm and output energy of 10mJ, with a pulse rate of up to 20,000Hz. A Photron Fastcam high speed camera is used for imaging, with an acquisition rate of 3,000Hz at 1024×1024 pixel resolution. A special version of DaVis 7 is used to process high speed PIV data. Standard acquisition is 500 image pairs, at a rate of 3,000Hz. The image sizes are 768×480 pixels in the case of the $d = 4mm$ experiment, and 640×368 pixels for the $d = 3mm$ experiment. The vector calculation is done using multi-pass, dual frame cross-correlation on changing window size. The interrogation window size is changing from 128×128 pixels to 16×16 pixels, with a 50% overlap.

The data from our PIV measurements will be presented in the form of: i) component of mean velocity in Ox direction, $\bar{u}(x, y)$, ii) mean vorticity component in xOy plane, $\bar{\omega}_z(x, y) = \overline{(\frac{\partial v}{\partial x} - \frac{\partial u}{\partial y})}$, and iii) Reynolds Stress components $\overline{v'^2}(x, y)$ and $\overline{u'v'}(x, y)$.

We will use $\bar{u}(x, y)$ to measure the length of the recirculation bubble L_b/D as the horizontal distance from the trailing edge, of the main cylinder, to the point where the iso-contour of $\bar{u} = 0$ intersects Ox . The uncertainty of the L_b/D is measured manually from stagnation point definition of the velocity field streamlines.

Phase-averaged flows

From the instantaneous flow fields of PIV measurements, we can obtain phase averaged flows (see Perrin *et al.*, 2007). This technique allows us to observe the flow dynamics at the frequency of the global mode, without noise of other scales typical of turbulent flows. One position in the vector field is chosen as a reference point, and the velocity time series are extracted for that point for the duration of the entire acquisition. The resulting time series are processed through bandpass filter, shown in figure 2.7(a), and are used to make a time basis for the averaging. The reference point is usually chosen at a point, in the flow, where the Kármán street vortices can be clearly seen, and the each phase is well resolved. Using a Hilbert transform, we are separating the velocity signal from the time series into amplitude and phase which is shown in figure 2.7(b). The Hilbert transform is obtained by performing a Fast Fourier Transform (FFT) on our velocity signal, removing half of the obtained data, and then performing an inverse FFT on the remaining signal. The FFT and inverse FFT transformations have been performed using the appropriate modules in LabView software. From the extracted phase signal, we can choose a phase, and perform averaging of velocities in all other points in the flow, on the same basis,

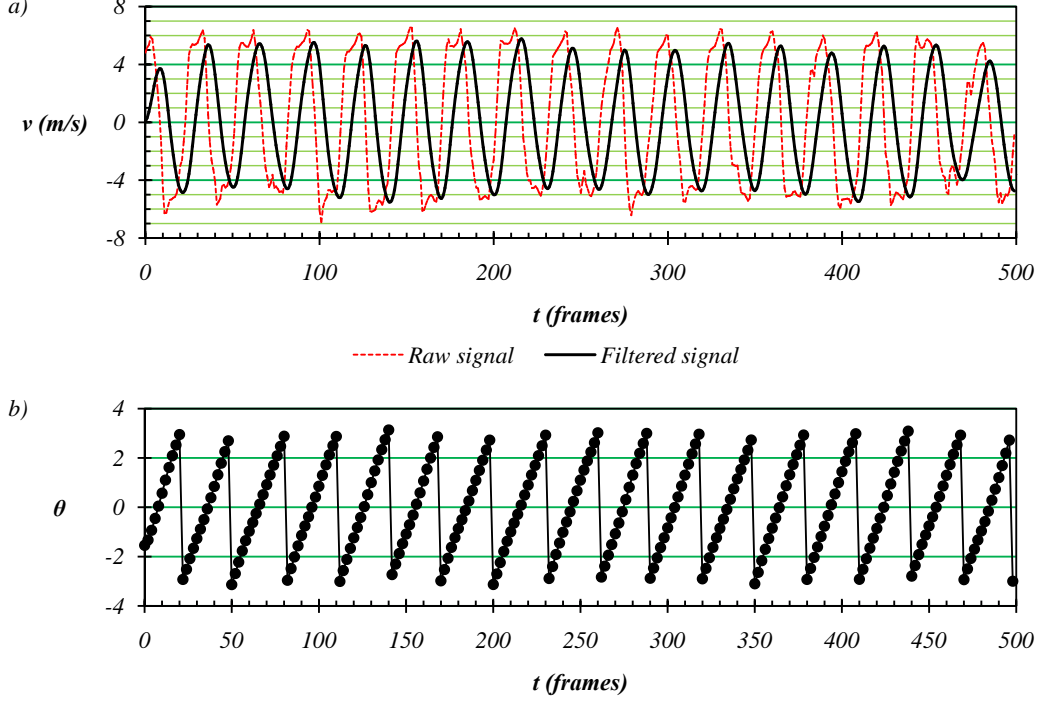


Figure 2.7: Local transversal velocity $v(t)$ from instantaneous high-speed PIV fields, used to build the phase-averaged signal: (a) raw (red) and filtered (black) velocity signal and (b) phase $\theta(t)$ of the velocity signal.

i.e. on the same phase. Since vorticity in two dimension acts as a scalar it is simple to calculate and is the most convenient form of result presentation, in our case.

2.3.3 Pressure measurements

The main cylinder is equipped with 32 pressure taps (figure 2.4b and figure 2.5), distributed along the entire perimeter of its cross-section at mid-span ($z = 0$). They are connected to two Scanivalve DSA 3217/16px differential pressure measurement arrays, capable of taking 100 samples of pressure per second. These samples are automatically averaged and a mean pressure is given as an output. In our mapping experiments, we have performed 30s and 40s long measurements of pressure for each position of the control cylinder. From these measurements, we obtain a mean pressure coefficient $C_p(s)$:

$$C_p(s) = \frac{p(s) - p_{ref}}{p(0) - p_{ref}}, \quad (2.2)$$

where p_{ref} is a reference static pressure, measured at the inlet of the wind tunnel test area, and $p(0)$ is the pressure measured at the head of the main cylinder. In some instances, in this

2. EXPERIMENTAL SETUP

thesis, we will refer to the pressure in arbitrary units ($A.U.$), which is an unscaled unit given by the output of the Scanivalve devices, where $100 A.U. = 9.7 Pa$.

In our study, we take into account only the pressure drag, since the Reynolds numbers of this magnitude and the shape of the main cylinder render the viscous drag contribution to the drag coefficient to be negligible. The total drag can be given as $C_d = C_{d(p)} + C_{d(\nu)}$; since the flow around our main cylinder is strongly separated, the pressure part of the drag has an order of magnitude $O(1)$ and the viscous part $O(\frac{1}{\sqrt{Re}})$ (Batchelor, 1967). The viscous drag surely is changed by the control cylinder, but this change is negligible compared to the changes in pressure drag, for the Reynolds numbers investigated in this work. The sectional form drag C_d is then classically estimated by integrating the projected pressure stress over the cylinder perimeter, as in:

$$C_d = \frac{1}{D} \oint C_p(s) \vec{n} \cdot \vec{e}_x ds. \quad (2.3)$$

The lift is computed by integrating the y component of pressure:

$$C_l = \frac{1}{D} \oint C_p(s) \vec{n} \cdot \vec{e}_y ds. \quad (2.4)$$

The base pressure coefficient C_{pb} is computed from the spatial average of the 5 pressure taps that are distributed on the blunt base of the cylinder:

$$C_{pb} = \frac{1}{D} \int_{base} C_p(s) ds. \quad (2.5)$$

The DSA devices are not able to recover the true rate of fluctuation of the pressure, but we can still build the $C_{pb(rms)}$ from those 40s of measurements, which gives an image of the fluctuation levels.

2.4 Experimental problems

Two main difficulties were encountered during the long mapping experiments: variations of the environment temperature and the asymmetry of the flow around the main cylinder. Next two sections will describe and discuss both effects in detail.

2.4.1 Ambient temperature variations

In order to investigate this occurrence which has plagued more or less each of our experiments, we have performed an experiment in which we measured the pressure around the bluff cylinder, for the duration of a typical mapping experiment, except that there was no control cylinder present in the wake, and no velocity in the tunnel ($U_0 = 0$). The goal was simply to see how does the pressure change purely with time. The results are presented in figure 2.8(a) for the pressure at the head of the main cylinder and in (b) for the pressure at the base. The definitions

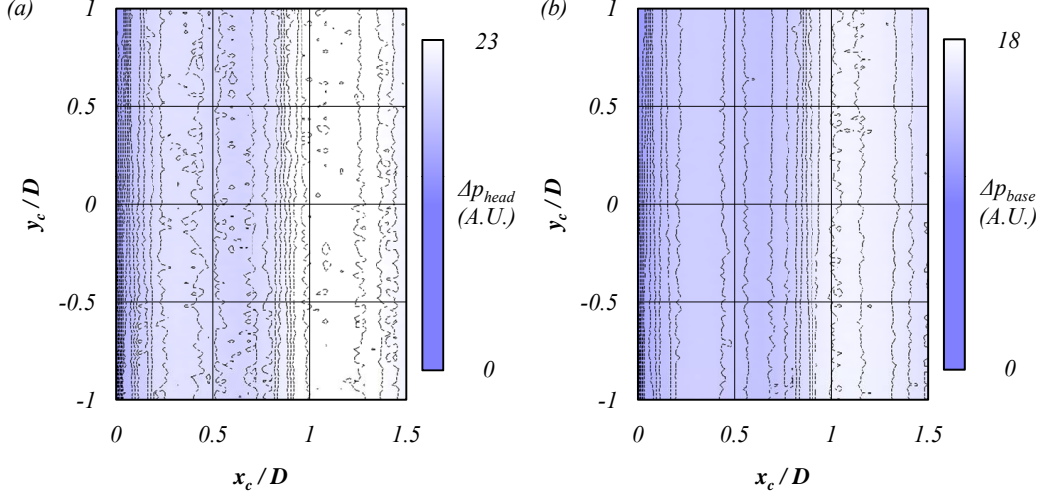


Figure 2.8: Maps of the ambient variations of (a) pressure at the head and (b) pressure at the base of the main cylinder, when no control cylinder is present and the velocity is $U_0 = 0$. Pressure is given in arbitrary units (see section 2.3.3).

for these are given by equations 2.6 and 2.7:

$$\Delta p_{head} = p(i = 0) - p_{ref}, \quad (2.6)$$

$$\Delta p_{base} = \frac{1}{5} \sum_{i=15}^{19} p(i) - p_{ref}, \quad (2.7)$$

where index i denotes the pressure port as per numbering given in figure 2.5. The pressure here is presented in arbitrary units, which we will refer to simply as "units" in further text.

If we plot the pressure in these two maps on an absolute time scale we obtain figure 2.9. Here we can see a time span of the experiment to be roughly two days, starting at 14h on day 1 and ending at 12h on day 3. We see pressure increase until midnight between day 1 and day 2, then slight decrease during the morning hours of day 2, followed by sharp increase in the afternoon period and again a plateau in the evening to midnight. Morning hours of day 3 again see a decrease in pressure. Based on the above, we can conclude that the pressure variation is closely correlated with the time of day, ie. with the daily temperature variations. Months of April and May can be very hot during the day and very cold during the night, and this drastic change has left its imprint on our experiment.

We can observe actually two types of pressure variations: one is described above and is of the order of 20 units, but another is the difference between the pressure at the head and at the base when there is no velocity in the tunnel, and when this pressure difference should be

2. EXPERIMENTAL SETUP

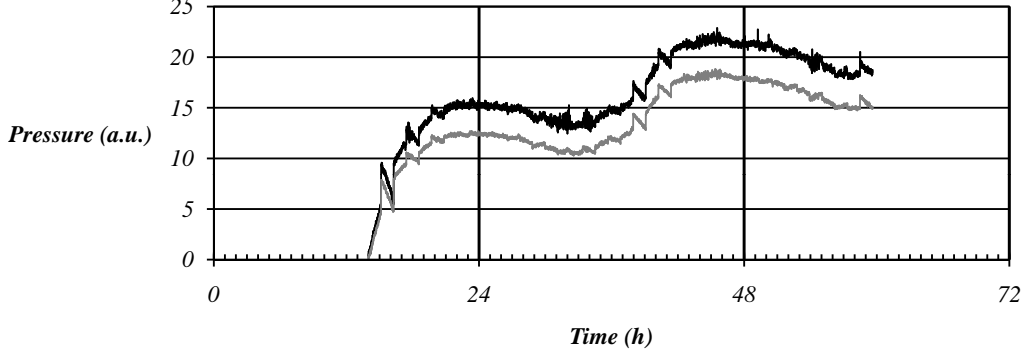


Figure 2.9: Evolution in time of pressure at the head of the main cylinder (black) and at the base (grey), when no control cylinder is present and the velocity is $U_0 = 0$. Pressure is given in arbitrary units (see section 2.3.3).

constant. This is clearly visible in figure 2.9; both pressures start at 0, but as time evolves, the pressures diverge and we can see a drift of about 5 units, between these two measurements. This pressure drift is probably caused by the Scanivalve devices.

In order to quantify the significance of these variations, we need to compare them with normal working conditions for the mapping experiments. As a reference, the pressure in arbitrary units for the natural flow at $Re = 13,000$ is $p_{head} \approx 447$ and $p_{base} \approx 275$. Therefore, the ambient pressure variations are at most around 7% of the natural values for the standard mapping experiment. This poses a serious difficulty when smaller control cylinders of $0.1mm$ and $1mm$ are used, since the variations are of the same order as some of the effects of those control cylinder. However, the variation occurs in good correlation with the time of day, and is relatively easy to filter out from the resulting map. The variation caused by the Scanivalve devices is on the order of 1%, and poses no significant impact on our results.

2.4.2 Shear layer asymmetry

If one looks at figure 3.2, it is clear after a careful check that the the pressure distribution for the natural flow around the main cylinder is not exactly symmetric with regard to the Ox axis. There are many small imperfections in our experimental setup who influence this; starting from the air that is entering the inlet of the tunnel up to the setup of zero inclination of the bluff cylinder, which is done by hand and level. The lift maps in many experiments which will be presented in further text betray this asymmetry by the fact that the natural lift is always slightly biased. However, usual lift bias and pressure asymmetry is not big enough to significantly change the results. We have performed many experiments and find that the structure of the sensitive regions is very robust. If we compare the maps of base pressure for the $3mm$ circular control cylinder in figures 4.3(b) and 4.9(b) we can see an obvious difference in the shapes, but all of the different regions of pressure sensitivity are present in both examples.

Chapter 3

Natural flow around the bluff cylinder

3.1 Boundary layer evolution

We will first describe the basic properties of the "natural" flow around the main cylinder (when no control cylinder is present). The immediate question is: how does the boundary layer evolve along the surface of the main cylinder, for a wide range of Reynolds numbers around the one used in our experiments? The free stream velocity of is measured at the inlet of the tunnel test area, and the Reynolds number is calculated, with the main cylinder height D as the characteristic length, as $Re = \frac{DU_0}{\nu}$. We have used PIV acquisitions to obtain mean velocity fields for several different Reynolds numbers and the resulting velocity streamlines can be observed in figure 3.1. First, we see a laminar flow for $Re = 4300$ with no detachment; the flow speed is very low and the PIV imaging was barely adequate to resolve the streamlines, but it is apparent that there is no flow detachment until the trailing edge. For a $Re = 6100$ we can see that the boundary layer is detached at the junction between the semi-circular front and the upper flat surface. Flow visualization (not shown here) reveals that the detached shear layer stays laminar for some distance after the detachment and never re-attaches, producing a wide wake. For $Re = 8700$ the shear layer undergoes a transition to turbulent and starts to re-attach at the trailing edge of the main cylinder. Since the transition to turbulence of the detached boundary layer occurs progressively earlier when we increase from $Re = 13500$ to $Re = 57500$, we can observe how the detachment bubble gets smaller and the re-attachment point moves upstream. So, from a detachment bubble that covers the entire length of the main cylinder's flat surface, for $Re = 8700$, we arrive at a very small bubble that would ultimately disappear if we could increase Re further. This case is not shown here, but it would have a completely attached, fully turbulent boundary layer. The pressure distribution around the main cylinder at different Reynolds numbers is shown in figure 3.2. We can observe that the pressure

3. NATURAL FLOW AROUND THE BLUFF CYLINDER

coefficient is constant at the front of the main cylinder, and slightly affected near the junctions with the upper and lower flat part. The level of the base pressure is changing with the Re , and this change is approximately uniform for all five base pressure ports. The radical change in the pressure distribution on the upper and lower flat surfaces confirms the PIV images of the boundary layer change, shown earlier.

Figure 3.3(a) shows how the natural Strouhal number changes when we change the Reynolds number of the experiment. The relationship between the Reynolds number and the vortex shedding frequency is consistent with the work for a similarly shaped bluff cylinder by [Rowe et al. \(2001\)](#). This is not the case with the base pressure which in our case is also increased with increasing Re as can be seen in figures 3.2 and 3.3(b).

The standard flow conditions of the experiment are defined by a free stream velocity of $U_0 = 8m/s$, and the Reynolds number is calculated to be $Re = 13000$. These conditions are used for all of the experiments, except where noted differently. Figure 3.4 summarizes the main properties of the natural flow at $Re = 13000$. The color map in Figure 3.4(a) shows the instantaneous modulus of velocity obtained from PIV acquisitions at $z = 0$. The boundary layer, that is initiated at the stagnation point $x = -2D$ separates at the junction with the flat wall at $x = -1.5D$. The laminar separation becomes turbulent, as shown by the presence of periodic regions of high velocities in Figure 3.4(a), revealing a transition mechanism due to the Kelvin-Helmholtz instability. The detached boundary layer re-attaches at about $x = -0.4D$. The turbulent boundary layer finally breaks away at the sharp trailing edge $x = 0$ of the main body. From hot-wire probe measurements of the boundary layer, at $x = -0.1mm$, just upstream of the trailing edge (shown in figure 3.5), we have obtained a boundary layer thickness of $\delta_{99} = 0.12$, momentum deficit thickness of $\delta_2 = 0.014$ and the form factor of $H_{12} = 1.24$. The boundary layer properties are similar to the compiled results in the recent work of [Pastoor et al. \(2008\)](#) involving blunt trailing edge cylinders. However, the base pressure in our case $C_{pbn} = -0.60$, is lower compared to previous studies (-0.57 to -0.51). The difference might be attributed to end conditions, that are free in our case and bounded by walls in [Pastoor et al. \(2008\)](#). The form drag computed from equation (2.3) is $C_{dn} = 0.74$.

The properties of the turbulent mixing layers just after the detachment from the trailing edge are analyzed using flying hot wire measurements performed at $x = 0.1mm$ and traversed in the vertical direction through $-2D < y < +2D$ (in steps of $0.02D$). The curves in figure 3.4(b) show the mean velocity profile, \bar{u}_A (thick black line); and the fluctuation profile, $\sigma = \sqrt{u_A'^2}$ (dashed line). The maximum fluctuation rate in the mixing layer is 25%. The turbulent mixing layer thickness $\delta_{1/2}$ can be deduced from the vertical gradient of the mean velocity $\frac{\partial \bar{u}_A}{\partial y}$. This gradient is shown, as thin black line, in the inset of Figure 3.4(b). Defining $\delta_{1/2}$ as the width of the velocity gradient peak at half of its height, we find a turbulent layer thickness of $\delta_{1/2} = 0.05D = 1.25mm$. The vertical component of the velocity being negligible at the trailing edge, the mean velocity gradient there is also a good estimate of the mean vorticity: $\frac{\partial \bar{u}_A}{\partial y} \approx \bar{\omega}_z$. Mean vorticity profile $\bar{\omega}_z$, measured by PIV, is represented with circles in the inset of

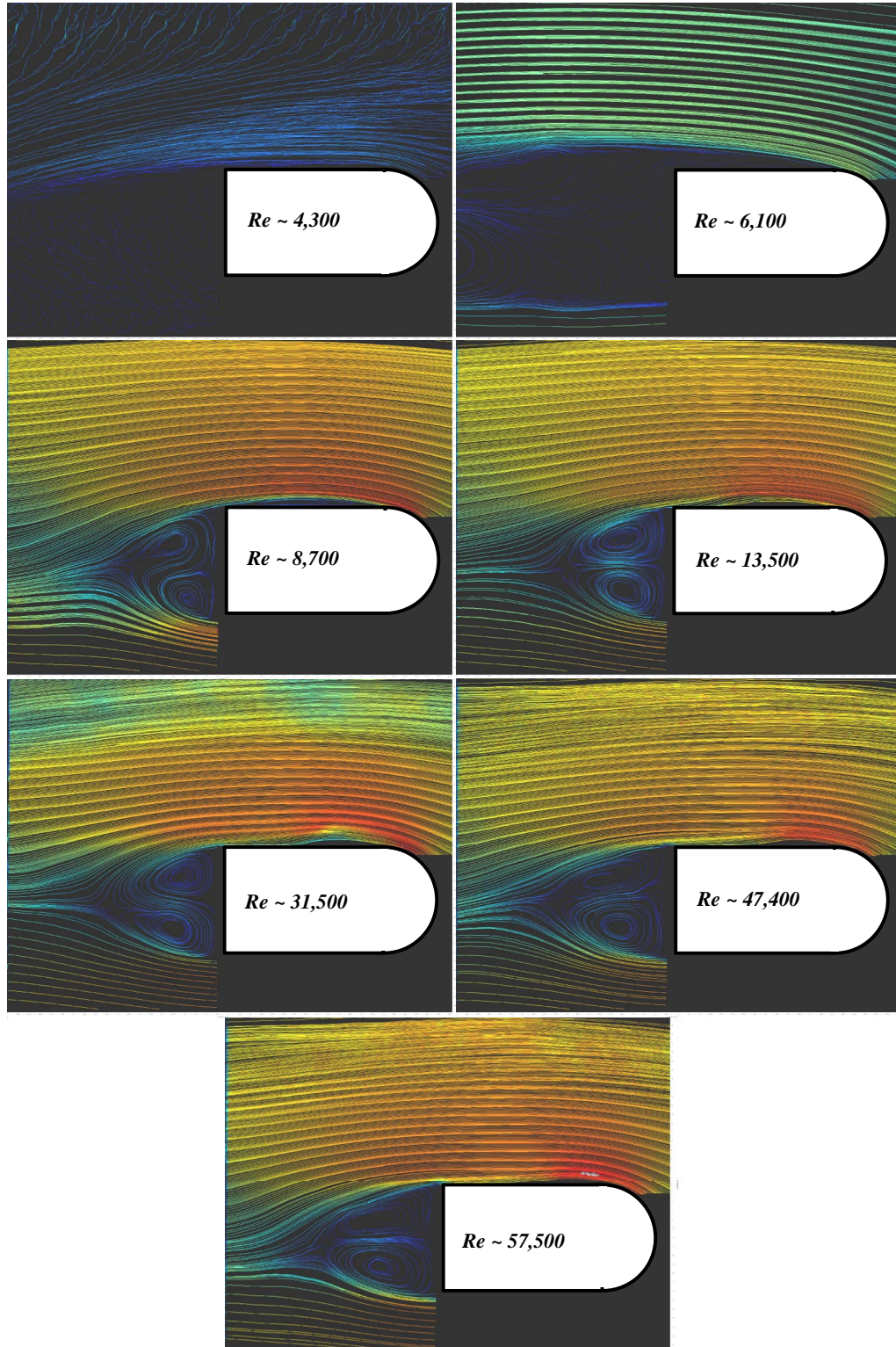


Figure 3.1: Streamlines of the mean velocity for the natural flow around the main cylinder for different Re .

3. NATURAL FLOW AROUND THE BLUFF CYLINDER

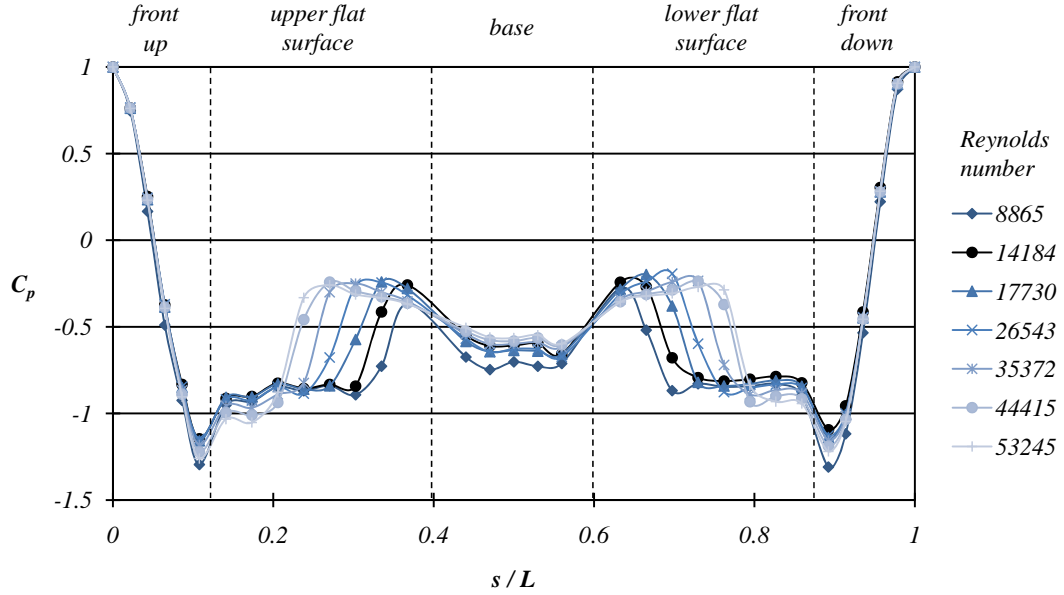


Figure 3.2: Pressure coefficient $C_p(s)$ distribution around the perimeter of the main cylinder for different Re .

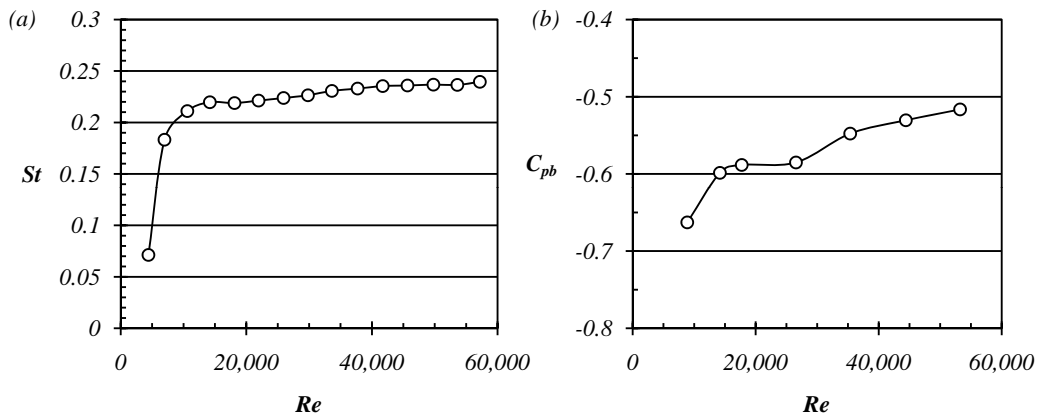


Figure 3.3: Evolution of (a) Strouhal number St and (b) base pressure coefficient C_{pb} of the main cylinder with increasing Reynolds number.

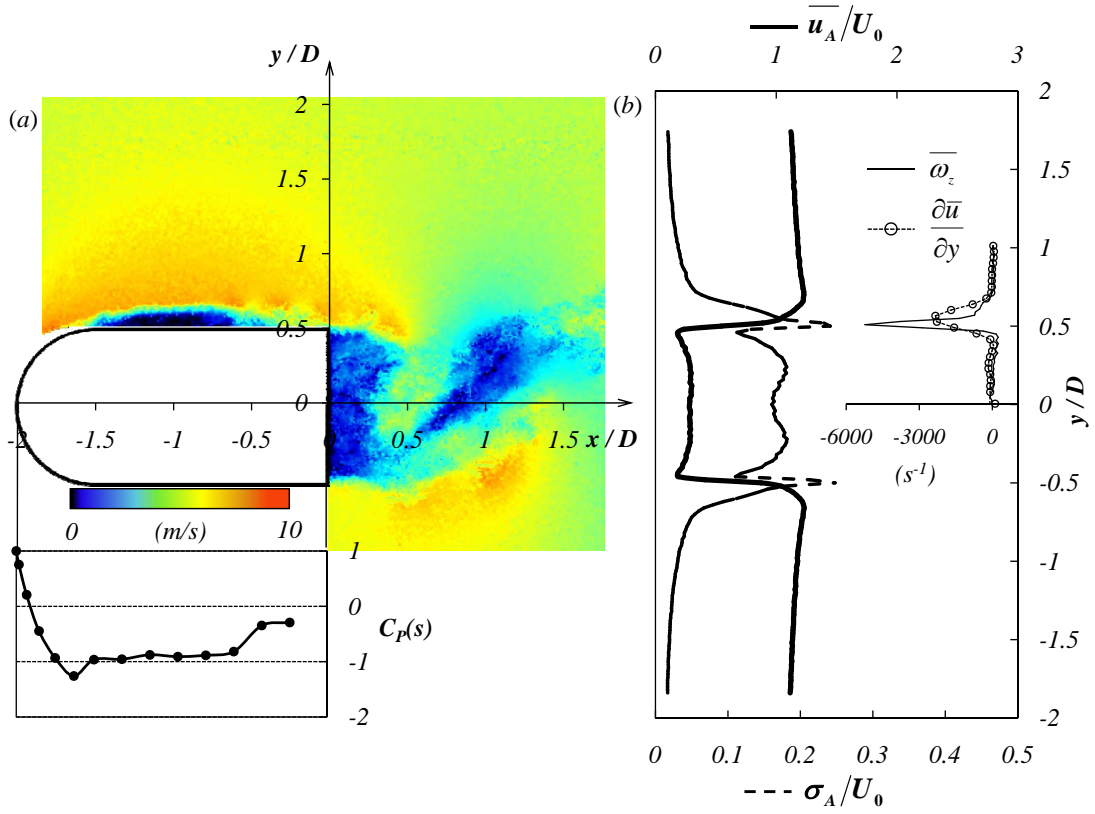


Figure 3.4: Natural flow around the bluff body at $Re = 13000$; the color map (a) shows an instantaneous field of the modulus $\sqrt{u^2 + v^2}$, with velocities ranging from 0m/s for black, up to 10m/s for orange, with the $C_p(s)$ distribution shown below. The diagram on the right (b) depicts the vertical profile measured with the flying hot wire just behind the rear of the blunt body at $x = 0.1\text{mm}$. The mean $\overline{u_A}$ (thick line) and the fluctuation σ of velocity (dashed line) are normalized by U_0 . The inset diagram in (b) is a plot of the vorticity $\overline{\omega_z}$ measured from PIV (circles), and estimated (see text) from local velocity measurements (thin line). The plot shares the primary y/D axis.

3. NATURAL FLOW AROUND THE BLUFF CYLINDER

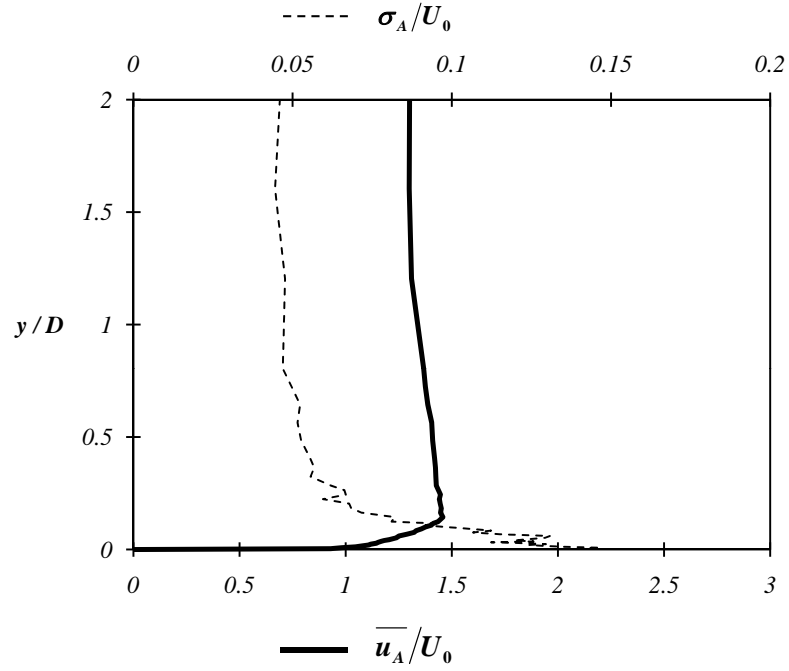


Figure 3.5: Boundary layer for $Re = 13000$ at $x = -0.1mm$, just before detachment from the trailing edge. Mean velocity $\overline{u_A}$ (thick line) and the fluctuation of velocity σ_A (dashed line) are normalized by U_0 .

figure 3.4(b). If we compare the two curves in the inset, we can see that the PIV interrogation window, with its size of $0.04D \times 0.04D$, induces a clear coarse graining effect, which has to be taken into account while analyzing the PIV results that will be presented in the following sections.

3.2 The mean natural wake and the dynamics in the wake

Now that we have described the flow in the vicinity of the body, we turn to some properties of the wake. The mean wake consists of a recirculation bubble, which is a region of reversed flow, and is shown in figure 3.6(a). The recirculation bubble is bounded by the two detached turbulent shear layers described above, and the vortex formation region produced by the shear layers roll-up. The detached shear layers are nicely visualized by the contours of z component of mean vorticity $\overline{\omega_z}$ in figure 3.6(b). A characteristic size of the formation region is the mean bubble length, measured to be $L_{bn}/D = 0.82 \pm 0.04$ in the case of the natural flow.

The wake dynamics are dominated by a global mode, known as the Kármán vortex street. The detached shear layers roll up and meet each other at a characteristic distance downstream from the trailing edge of the main cylinder, and vortex are shed at a selected frequency. The PIV measurements of Reynolds stresses in the natural wake, shown in figure 3.6(c) and (d), give a good reference of the dynamic part of the wake. We can observe one maximum of $\overline{v'^2}$, and a maximum and a minimum for $\overline{u'v'}$. These extrema are located at the points in the wake where the global mode originates, as we will see in later chapters. For now, we should note the streamwise locations of the extrema as $X_{\overline{v'^2}_{Max}}$, $X_{\overline{u'v'}_{Max}}$ and $X_{\overline{u'v'}_{Min}}$ and the streamwise size of the first contour around each extrema, marked as $\delta_{\overline{v'^2}}$ and $\delta_{\overline{u'v'}}$. A detailed analysis of how these values are affected by the control cylinders will be shown in chapter 4.

The global mode frequency is clearly observed in Figure 3.7, where the local spectra, from four hot wire probes, all display the peak in amplitude around the same frequency. This is identified as the natural frequency of $f_n = 70.75 \pm 0.25 Hz$, at the $Re = 13000$. The natural Strouhal number is calculated as $St = 0.221$. The large width of the peaks are related to the three dimensional disturbances of the turbulent wake, such as oblique vortex shedding and vortex dislocations (Prasad & Williamson, 1997; Williamson, 1996a). Between the three spectra obtained at different spanwise locations, we can observe slight differences: the peaks of the two centerline wires (A1 and A3) have larger amplitude, and better definitions. The peak of the first harmonic are better seen in the spectra of the wires on the right (A0) and left (A2) of the centerline. The differences in the peak definition are also indicating 3D properties of the wake, partly induced by the ends effect. The similarity of the spectra (A2) and (A0) is a consequence of the experimental symmetry with respect to the central plane $z = 0$.

The correlation coefficient values computed from Eq.2.1 for the natural case are $r_{n[0-1]} = 0.204$, $r_{n[1-2]} = 0.190$, $r_{n[0-2]} = 0.089$ and $r_{n[1-3]} = -0.31$. Three-dimensionality disturbances of the wake have direct impact on the spanwise correlation (Norberg, 2001). The correlation

3. NATURAL FLOW AROUND THE BLUFF CYLINDER

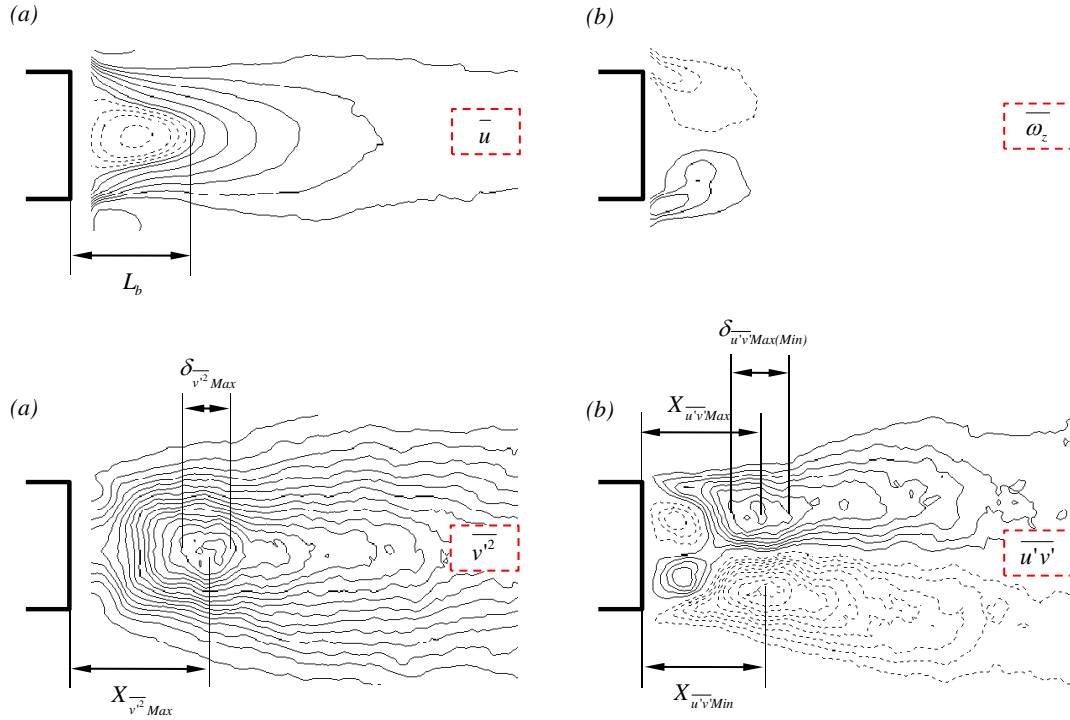


Figure 3.6: Mean and dynamic components of the natural wake: (a) mean streamwise velocity \bar{u} , with continuous lines for positive and dashed lines for negative values, from the list $[-3, -2, -1, -0.5, 0, 0.5, 1, 2 \dots 8] m/s$; (b) mean vorticity $\bar{\omega}_z$, where lines are at $\pm 500, \pm 1000$ and $\pm 1500 s^{-1}$ (continuous for positive, and dashed for negative vorticity) and Reynolds stress components (c) $\bar{v'^2}$, in range of $0(m/s)^2$ to $15(m/s)^2$ and (d) $\bar{u'v'}$, in range of $\pm 5(m/s)^2$ (b). The isolines are in the interval of $1(m/s)^2$ (continuous lines for positive and dashed for negative values).

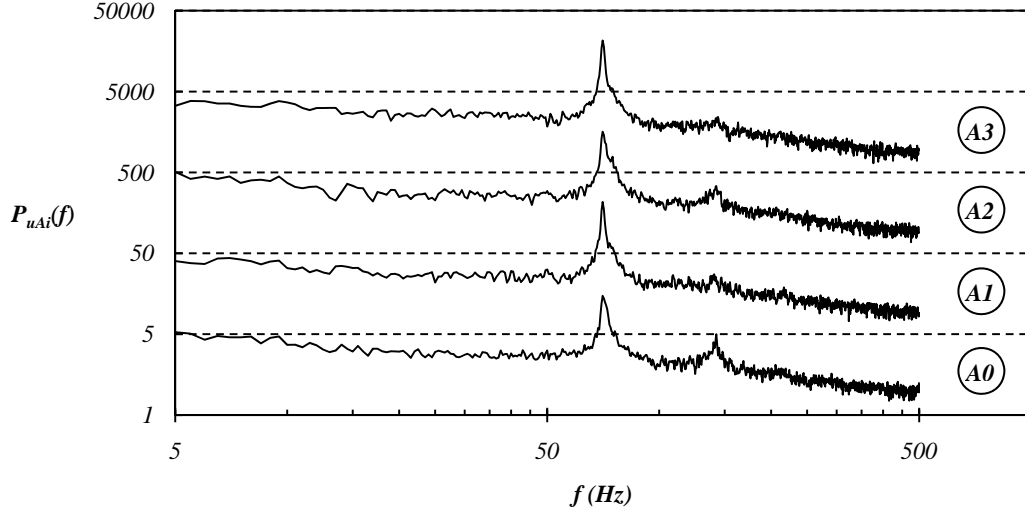


Figure 3.7: The power spectra of the velocity signals for the natural flow measured at the three spanwise locations (see figure 2.4b). Starting from A0, each subsequent spectrum is shifted by a decade, for visibility purposes.

values of $r_{n[0-1]}$ and $r_{n[1-2]}$, performed on a distance $2D$, on either side of the wake centerline, are quite similar. Once again, this is a consequence of the experimental symmetry with respect to the centerplane $z = 0$. For the spanwise distance of $4D$, the correlation coefficient $r_{n[0-2]}$ is reduced by a factor of 2.

3. NATURAL FLOW AROUND THE BLUFF CYLINDER

Chapter 4

Wake with a circular control cylinder

In the following sections, we will present the results of experiments when a small circular control cylinder is placed in the wake. Two diameters of control cylinder will be tested, the control cylinder of diameter $d = 1mm$, which is always smaller than the mixing layer thickness at the trailing edge detachment (see chapter 3). The other control cylinder diameter is $d = 3mm$. We will show the maps of sensitivity of the wake for both control cylinders, as well as focus in detail on what happens when a control cylinder is displaced vertically across the wake at a chosen downstream distance from the main cylinder, as well as when it is placed at some key positions on the horizontal axis of the wake.

4.1 Mapping of global properties

4.1.1 Global frequency change

If we assemble the detected global mode frequency (see section 2.3.1) for each position of the control cylinder (see section 2.2.3), we obtain a map of the sensitivity for the global mode frequency to the presence of the control cylinder, as shown in figure 4.1 for $d = 1mm$, and in figure 4.2 for $d = 3mm$. The selected global mode frequency is represented as the Strouhal number, with the natural frequency for each map depicted in white. We present four maps for each control cylinder size, obtained from the four hot-wire probes placed in the wake. We can confirm that the detected frequency is changing in an identical fashion all along the span of the main cylinder, because there are no noticeable differences in structure if we compare the appropriate maps between probes A0, A1 and A2. This is true for both $1mm$ and $3mm$ control cylinders. Also, maps for wires A1 and A3 are identical, which is expected from the vertical symmetry of the Kármán vortex street (see positions of wires A1 and A3 in figure 2.4). We

4. WAKE WITH A CIRCULAR CONTROL CYLINDER

can see slight differences in the natural value around which the frequency change envelope is correspondingly shifted. As explained before, these maps are assembled from hot wire probe signals which are taken simultaneously, therefore, we can conclude that the selected frequency is not constant along the span of the body, but that it changes in a constant manner due to the control cylinder. This also brings another clue to the 3D properties of the flow around the main cylinder, which will be addressed in later chapters.

The analysis of the envelope of the frequency change shows that it ranges from -7% to $+4.5\%$, for the $1mm$ and -12% to $+20\%$, for the $3mm$ control cylinder, with regard to respective natural values. For the $3mm$ control cylinder, the increase of frequency is stronger than the decrease. Comparison of the structure of sensitive regions shows significant differences in the topology of the maps between the $1mm$ and $3mm$ cases. If we superimpose the natural mean recirculation bubble shape over the map (plotted with the dashed line), we can observe how in the case of $1mm$, the effects follow the contour of the mean bubble. This is not true for the $3mm$ case, which indicates strong modifications of the mean flow. The $3mm$ control cylinder is able to change the frequency much farther downstream than the $1mm$, especially in two very distinct regions adjacent to the $y_c = \pm 0.5D$ lines. The regions of frequency reduction are smaller, but the effect is almost double in the $3mm$ case. For the $d = 3mm$ case, we also observe a frequency increase in two regions symmetric to the Ox axis and centered at $x_c = 0.75D$, $y_c = -0.70D$ and $x_c = 0.75D$, $y_c = +0.70D$, and a single local maximum located around $x_c/D = 0.4$, $y_c/D = 0$. These are not clearly observable for the $1mm$ case. All of these differences will be analyzed in detail using PIV measurements of the wake in section 4.2.2.

4.1.2 Base pressure and drag

The base pressure as a function of the position of the control cylinder is shown in figure 4.3. The registered base pressure change for $1mm$ case ranges from -1% to $+20\%$, and from -8% to $+56\%$, for the $3mm$ control cylinder. For both control cylinders, the major effect of base pressure increase is when the control cylinder is near the outline of the recirculation bubble. Again, in the $3mm$ case, the effects extend further downstream than the natural bubble limit, while for $1mm$ the effects follow the outline. For both cylinders there is a secondary region of base pressure increase, roughly centered around $x_c/D = 0.8$, $y_c/D = \pm 0.60$. This region is much more pronounced for the $3mm$ control cylinder. The middle of the wake shows very small increase by the $1mm$, but for the $3mm$ case we see a reduction in base pressure in two small regions symmetric to Ox axis, centered around $x_c/D = 0.4$, $y_c/D = \pm 0.025$. Finally we can see a base pressure increase for both maps at the wake centerline for positions $0.75 < x_c/D < 1.2$, at $y_c/D = 0$. Figure 4.4(a) and (b) show base pressure maps for $1mm$ and $3mm$ respectively, with an overlay of the contours of Strouhal number sensitivity. Comparing with global frequency for both cases, we can see that base pressure increase occurring at the outer boundary of the recirculating bubble can be achieved with either frequency increase or decrease. This result excludes the role of the Strouhal number in the drag reduction mechanism.

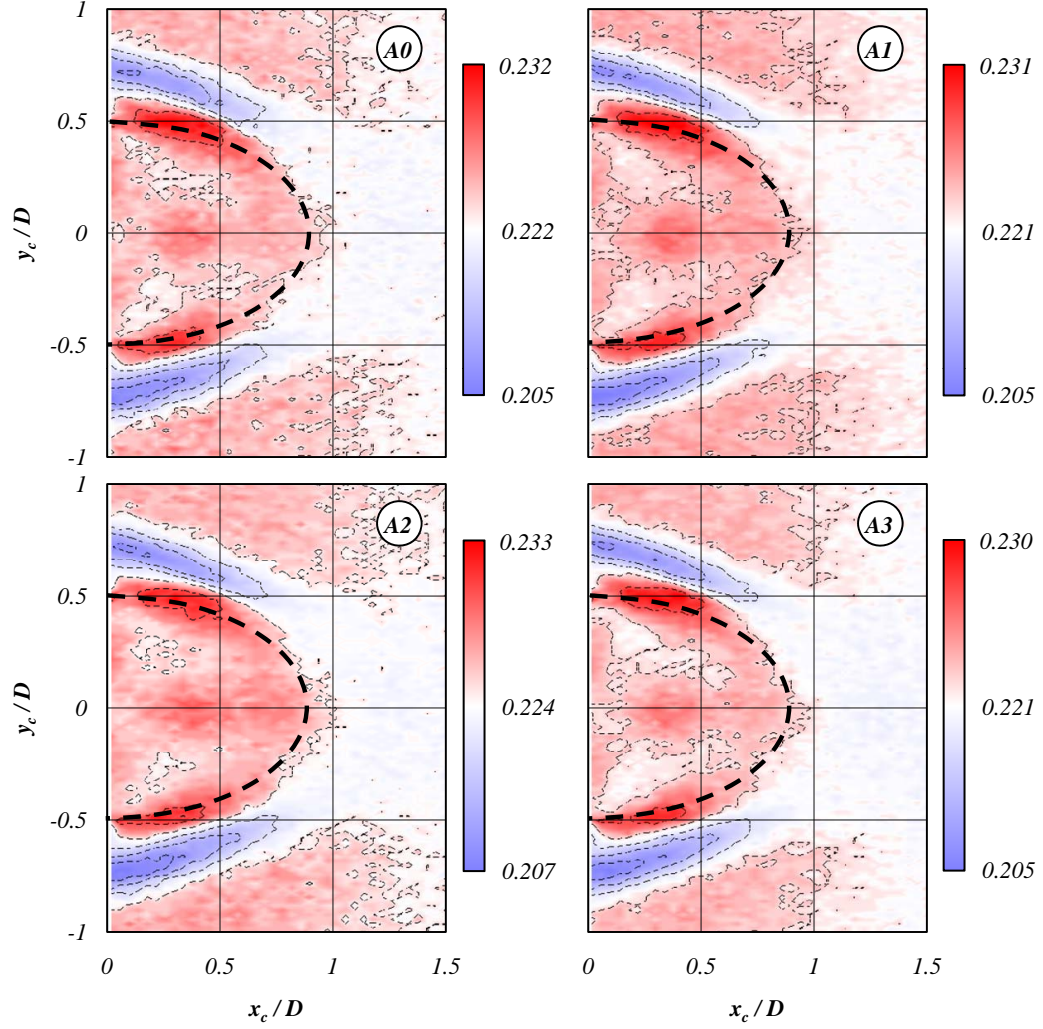


Figure 4.1: Global mode frequency sensitivity maps $S_t(x_c, y_c)$ for $d = 1mm$ control cylinder. The hot wire probe, from which the map is built, is indicated in the top right corner of each map. Blue color designates a decrease and red an increase in frequency compared to that of the natural frequency, which is given in white for each map. Dashed line depicts the shape of the natural flow recirculation bubble. The isolines are in the intervals of 0.005.

4. WAKE WITH A CIRCULAR CONTROL CYLINDER

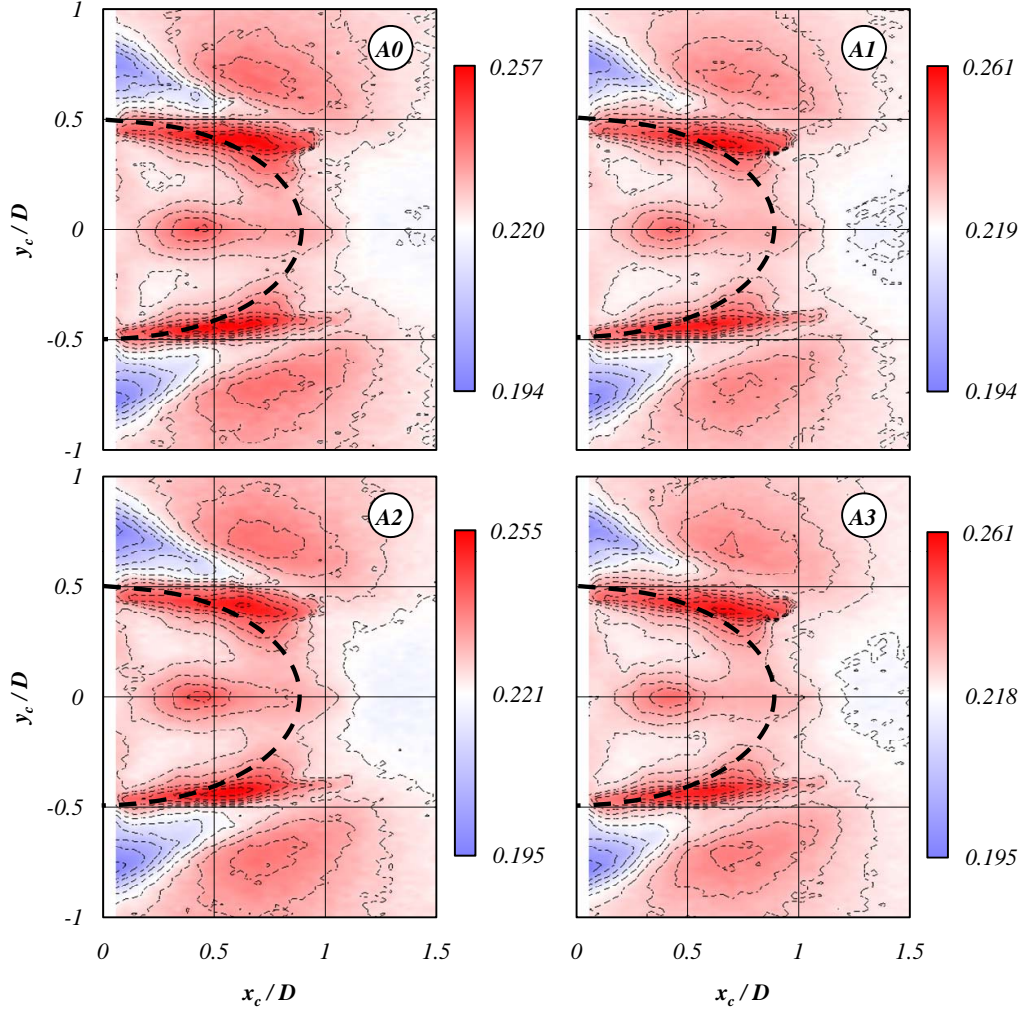


Figure 4.2: Global mode frequency sensitivity maps $S_t(x_c, y_c)$ for $d = 3mm$ control cylinder. The hot wire probe, from which the map is built, is indicated in the top right corner of each map. Blue color designates a decrease and red an increase in frequency compared to that of the natural frequency, which is given in white for each map. Dashed line depicts the shape of the natural flow recirculation bubble. The isolines are in the intervals of 0.005.

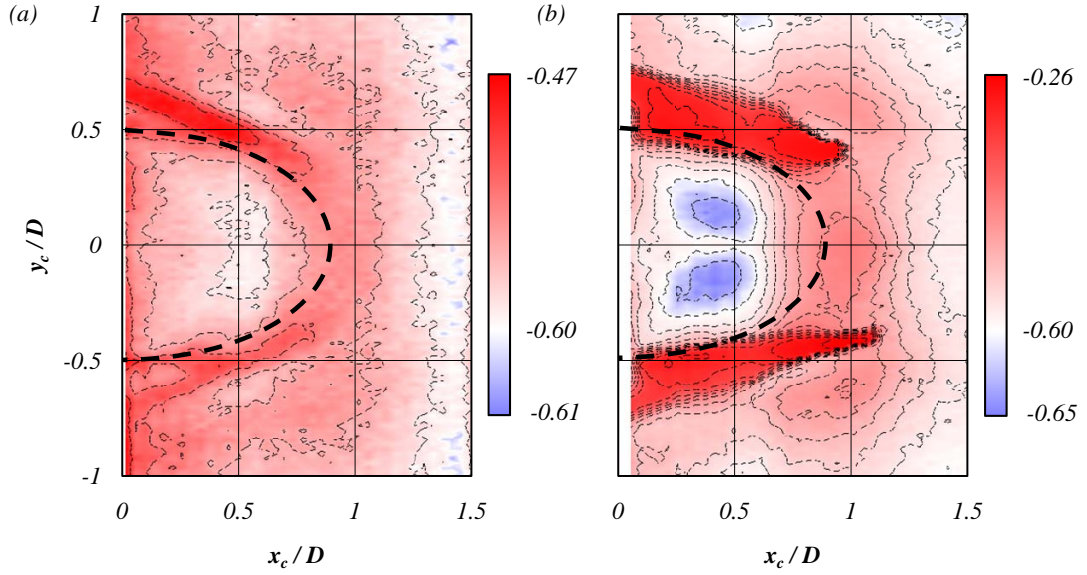


Figure 4.3: Base pressure sensitivity maps for (a) the $1mm$ and (b) the $3mm$ control cylinder. Isolines are in intervals of 0.03 . Blue color designates a decrease and red an increase in base pressure compared to that of the natural base pressure, which is given in white. Dashed line depicts the shape of the natural flow recirculation bubble.

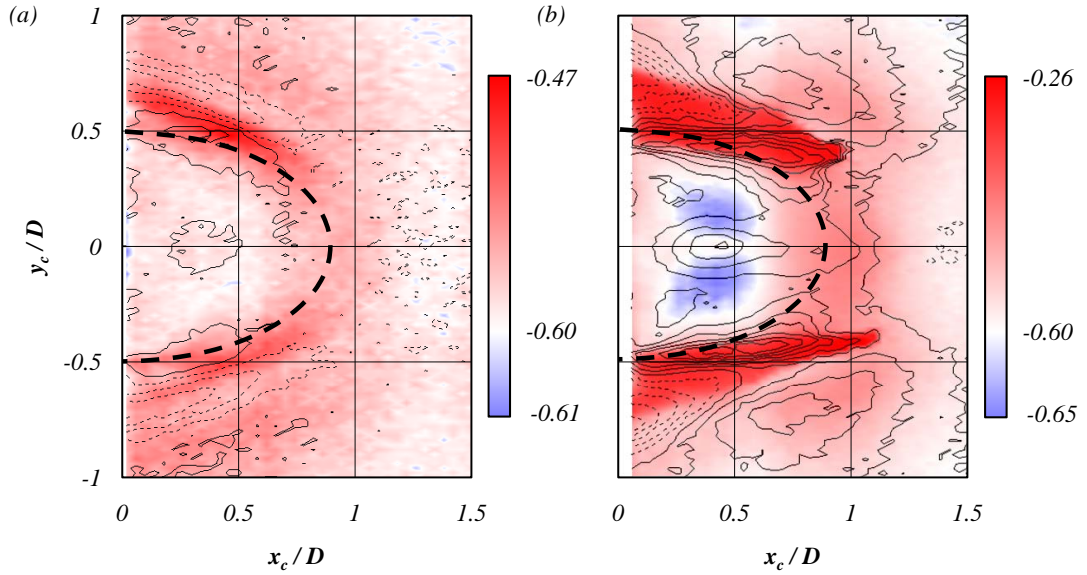


Figure 4.4: Base pressure sensitivity maps for (a) the $1mm$ and (b) the $3mm$ control cylinder with an overlay of contours of Strouhal number change. The isolines are identical as in figures 4.1 and 4.2, for wires A0.

4. WAKE WITH A CIRCULAR CONTROL CYLINDER

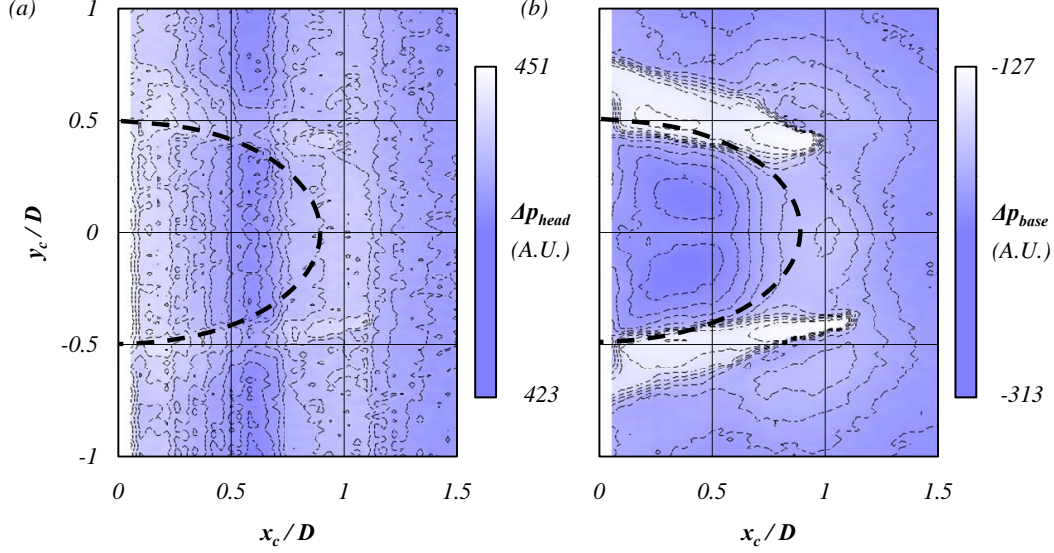


Figure 4.5: Impact of the 3mm control cylinder on (a) pressure at the head of the main cylinder Δp_{head} and (b) pressure at the base of the main cylinder Δp_{base} . Isolines depict 10 equidistant pressure levels in the given ranges. Pressure is in arbitrary units (see chapter 2).

A question can be posed at this time as to what is the relationship of base pressure and drag in our case? The pressure drag is dependent on the difference in pressure at the head and at the base of the body, and in our experiments we have found that the control cylinder only changes the base pressure significantly. This can be confirmed if we look at the pressure at the head of the main cylinder in figure 4.5(a) for each position of the control cylinder. In terms of arbitrary units (see section 2.3.3), the pressure at the head is in the range of $423 < \Delta p_{head} < 451$. This means that the head pressure is indeed susceptible to the presence of the control cylinder, but this change is very small ($\Delta_{head} = 27 A.U.$) when compared to the drastic change we see in the pressure at the base of the main cylinder, in figure 4.5(b), which is in range $-313 < \Delta p_{base} < -127$ and is several times greater ($\Delta_{base} = 186 A.U.$). From these figures, it clearly appears that the control cylinders change the base pressure without significantly influencing the pressure distribution on the frontal area of the body. Hence, the frontal contribution to the drag coefficient, denoted by C_{d0} , is constant leading to the simple formula $C_d = C_{d0} - C_{pb}$. This brings on the conclusion that the drag coefficient in our case is an affine function of base pressure, which is confirmed by scatter plots shown in figure 4.6.

4.1.3 Effects on lift

The control cylinders have also a significant effect on mean lift, as can be seen in figure 4.7 for (a) $d = 1mm$ and (b) $d = 3mm$ control cylinder. The lift changes between -0.23 and $+0.20$

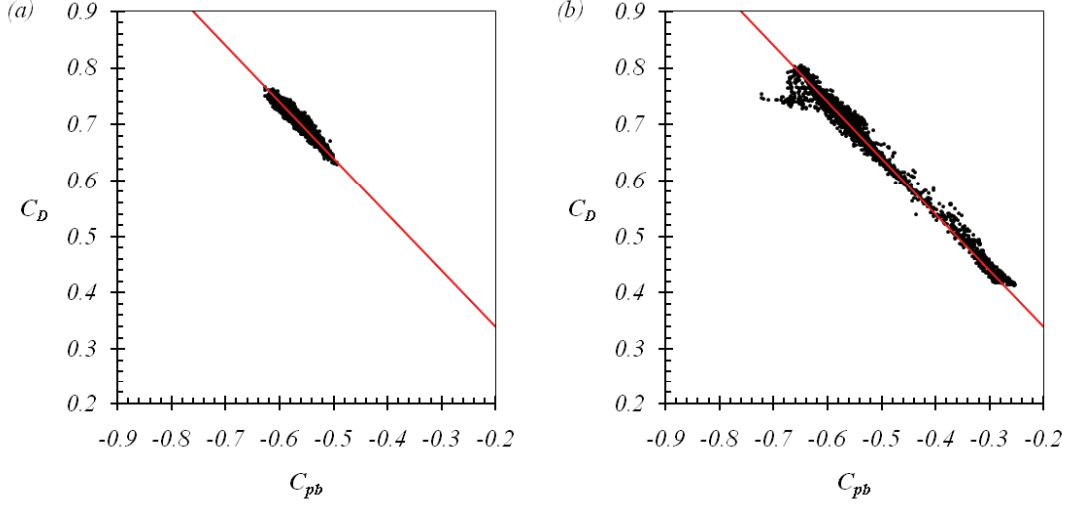


Figure 4.6: Scatter plots of the drag coefficients vs. base pressure coefficients for all the positions (x_c, y_c) of the 1mm (a) and 3mm (b) control cylinders. For both figures the straight line is $C_d = C_{d0} - C_{pb}$ with $C_{d0} = 0.14$.

for $d = 1mm$ and between -0.48 and 0.59 for $d = 3mm$ control cylinder. The maps also show a slight natural bias toward the negative lift coefficient; this comes from the fact that the flow is not completely symmetric, and that lift calculated by integrating the pressure around the main cylinder is very sensitive to these slight differences in the quality of the upper and lower boundary layers. These differences do not significantly alter the main result of these maps, which is that the lift is changed only when the control cylinder is very close to the trailing edge of the main cylinder. This in turn means that the lift is changed by changing the pressure in the boundary layer, before it detaches, and thus, this effect is not interesting for our main study, which focuses on control of the detached flow downstream in the wake.

Figure 4.8 shows how is the pressure distribution changed around the main cylinder, for positions of the control cylinder for which the lift coefficient is substantially changed. We can see that what changes is a global level of pressure imposed on the top or the bottom of the main cylinder, depending on where we put the control cylinder. We do not change the shape of pressure distribution curve, ie. there is no change in the detachment points of the boundary layers. We can see however, that the presence of the control cylinder, for example near the top edge (blue line in figure 4.8), increases the pressure on the whole top side of the main cylinder, but also, it decreases slightly the pressure on the bottom. The pressure increase is related to the presence of a stagnation point on the front of the control cylinder. The pressure difference between the top and the bottom yields a negative lift force.

4. WAKE WITH A CIRCULAR CONTROL CYLINDER

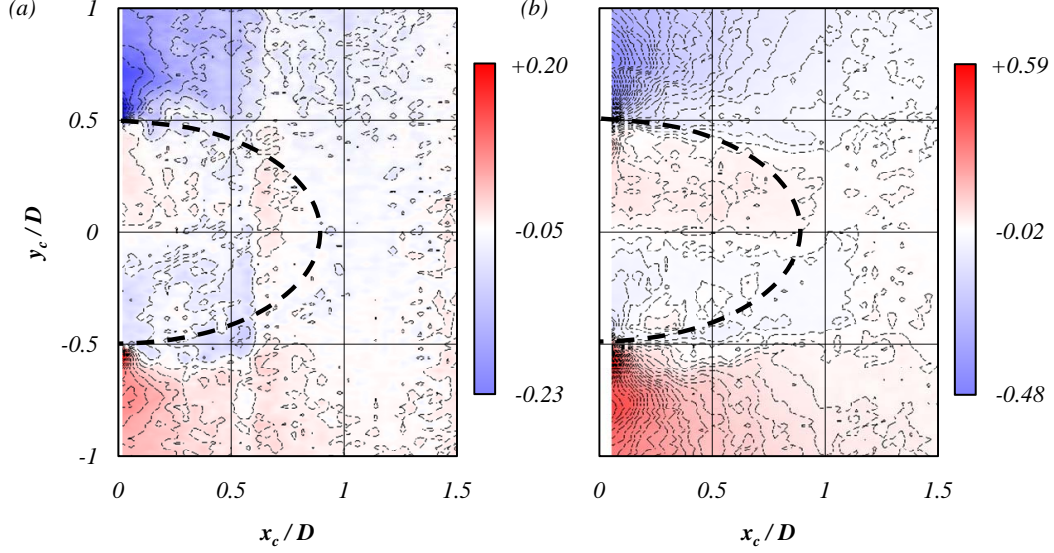


Figure 4.7: Mean lift coefficient sensitivity maps for (a) 1mm and (b) 3mm control cylinder. Isolines are in intervals of 0.02. Blue color designates a negative and red a positive lift. Dashed line depicts the shape of the natural flow recirculation bubble.

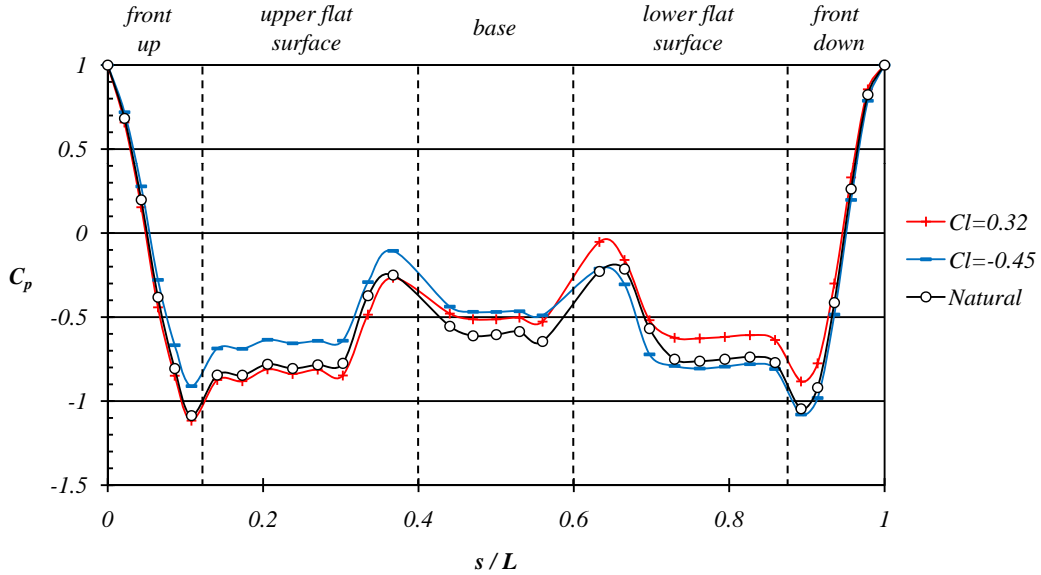


Figure 4.8: Pressure distribution around the main cylinder for three characteristic values of lift. Red line shows a case of positive lift (control cylinder at bottom), blue a case of negative lift (control cylinder at top) and black is the natural case for the same experiment.

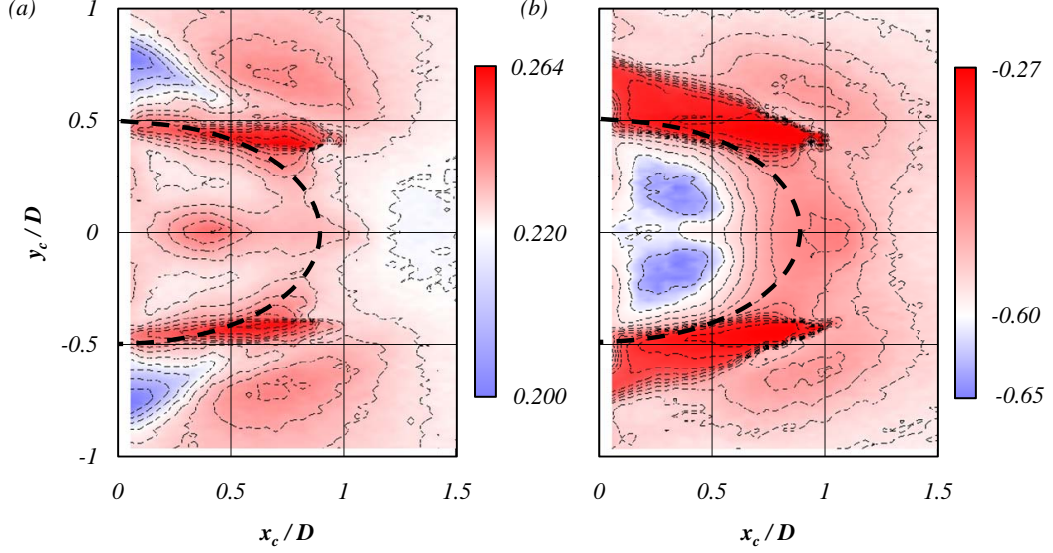


Figure 4.9: Sensitivity maps of (a) Strouhal number and (b) base pressure coefficient, for the $3mm$ control cylinder obtained in April 2009. Isolines are the same as in figures 4.2 and 4.3 for appropriate values.

4.1.4 Additional sensitivity maps for $d = 3mm$

We have performed several mapping experiments with the circular control cylinder of $d = 3mm$. The first experiments were limited to only the lower half of the wake and with less positions of the control cylinder (shown in chapter 6). As the experimental setup evolved with new equipment and new goals, we have also improved the resulting maps. The first experiment that completely mapped the wake sensitivity was performed in April of 2009. The results of this experiment are shown in figure 4.9(a) for the Strouhal number and (b) for the base pressure.

The base pressure map from this experiment was used in the article published in the Journal of Fluid Mechanics (Parezanović & Cadot, 2011). The whole experiment was very successful and as can be seen from the maps, very symmetric with respect to the horizontal axis. However, in mapping the Strouhal number, only three hot wire probes were used in positions A0, A1 and A3. Since we needed the information on the sensitivity of global frequency at several points along the span of the main cylinder, we have repeated the experiment with the same settings, in July 2010. This time all four hot wires were used, and the maps obtained are shown as a main result in figure 4.2. Unfortunately, due to a slight error in the main cylinder placement these maps do not exhibit a good symmetry like all others. This has been noted in section 2.4. However, both Strouhal and base pressure maps from both experiments show no significant differences in their values at the selected vertical line at $x_c/D = 0.4$, on which we have focused our main analysis.

4.2 Turbulent wake modification with a control cylinder at $x_c/D = 0.4$

4.2.1 Local velocity measurements

The sensitivity maps, give plenty of information with regard to localization and magnitude of the effect of the control cylinder on the global frequency selection. Ultimately however, they are only that; maps which tell us where to look for interesting phenomena, but they don't explain anything further about their origins or their mechanics. In order to understand what are the physical processes that define the global properties, and how are they affected by control, we have to focus on a specific position, or rather, a set of positions which are representative of all the observable effects. After reviewing the $1mm$ and $3mm$ maps of global frequency and base pressure, we have decided to focus our investigation on a fixed downstream position of the control cylinder at $x_c/D = 0.4$.

Figure 4.10(a-b) illustrates how the spectra of the velocity signals change, when the control cylinders of (a) $1mm$ and (b) $3mm$, are displaced vertically across the wake, at constant $x_c/D = 0.4$. The spectra, shown here, are measured by the three hot wire probes $A0$, $A1$ and $A2$ as depicted in figure 2.4(b). We will omit the result from wire $A3$ since it doesn't show anything new.

If we compare the spectra between the three spanwise measurements, for both sizes of the control cylinder, we can see very similar changes of both the frequency and the amplitude. We can conclude that the main effects imposed by the control cylinder are obviously 2D. Furthermore, the effects on the selected frequency f (where the spectrum amplitude is the largest) are symmetric with respect to the horizontal axis Oy . Considering that the measurement points are fixed at $y = -0.5D$, the local measurements experiment is never symmetric with regard to the horizontal axis; thus, the frequency symmetry $f(y_c) = f(-y_c)$ confirms that the frequency is a global quantity, and independent of where (in the wake) it is measured. On the other hand, the maximum amplitude of the spectra is not completely symmetric. The most important differences, are observed for positions $y_c/D < -0.5$ and $y_c/D > +0.5$. In the former case, the control cylinder is on the same side of the horizontal axis of the wake as the hot wire probes, while in the latter, they are on the opposite sides, which is clearly affecting the recorded amplitude.

Now we will analyze in more detail the results for each of the control cylinder sizes. In the case of the $1mm$ cylinder presented in figure 4.10(a), the frequency is reduced around $y_c/D = \pm 0.6$ for all three spanwise locations of the measurements. The amplitude, however, is different between the three measurement points and is also changing depending on the vertical position of the control cylinder. We can observe a higher amplitude when the control cylinder is in the range of $[-0.5D, 0.5D]$. The recorded amplitudes are lowest on the wire $A0$ and highest on $A1$. Wire $A2$ shows the worst peak quality.

The $3mm$ control cylinder, in figure 4.10(b), has a much more pronounced impact on all the properties of the spectrum, throughout the range of its positions presented here. Most notably,

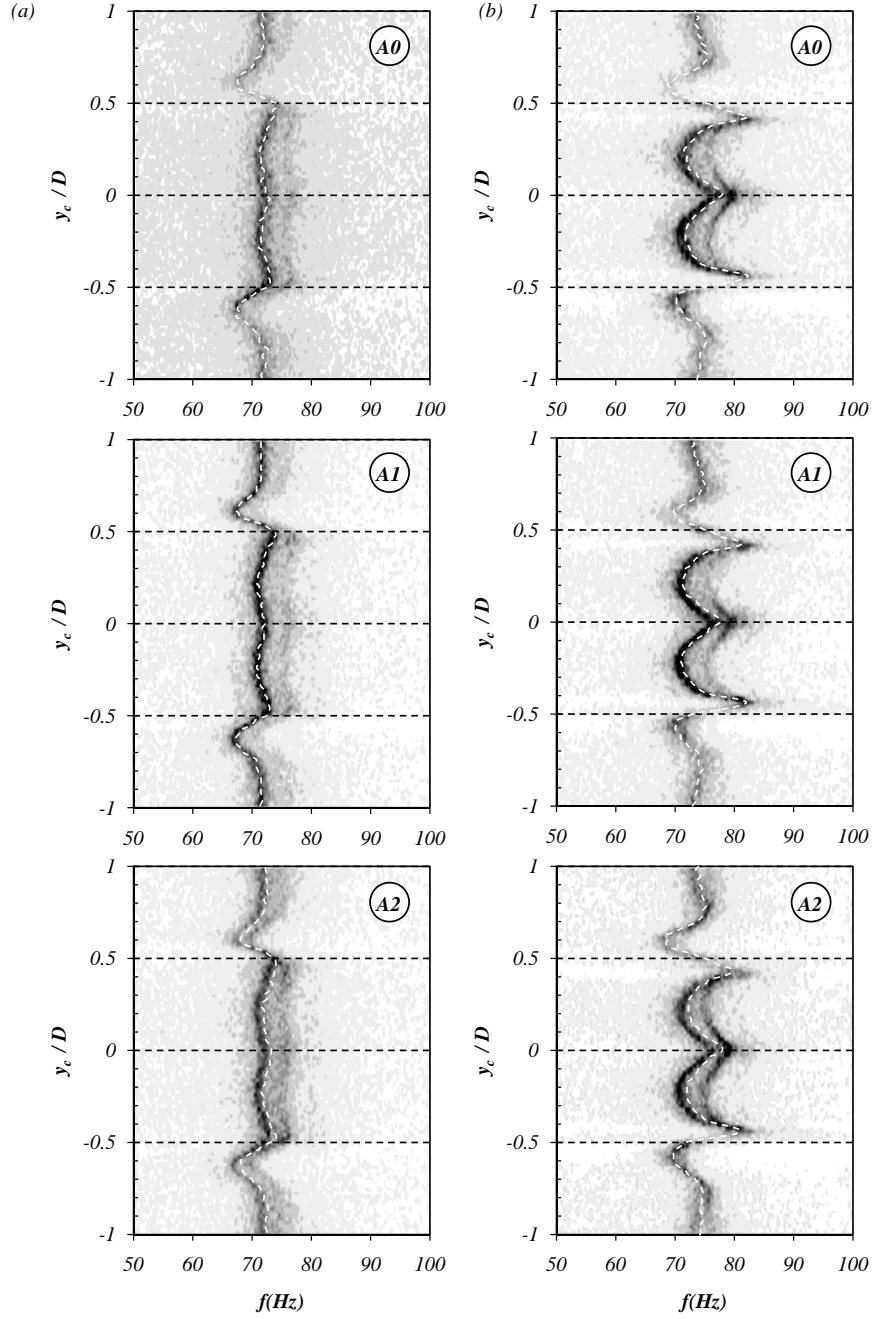


Figure 4.10: Evolution of the power spectra when the control cylinder is displaced along a vertical line at $x_c/D = 0.4$; (a) in the case of $d = 1mm$, (b) in the case of $d = 3mm$; horizontal axis is the frequency, vertical axis is the vertical position of the control cylinder, and the grayscale map shows the intensity of the amplitude of the spectrum; light gray for low, and dark gray for high amplitudes.

4. WAKE WITH A CIRCULAR CONTROL CYLINDER

we can see that the frequency changes much more than in the previous case, again around $y_c/D = \pm 0.5$, but in this case, we have both an increase and a decrease of frequency, where the increase is the stronger effect. The amplitude of the spectrum is completely damped for several positions, while it is greatly increased when the control cylinder is in the middle of the wake in the range of $[-0.4D, 0.4D]$. Additionally, for these positions of the control cylinder, we can observe a strong modulation displayed by a second, well defined energy peak. As shown by Williamson (1992), this modulation is associated to periodic dislocations in the wake.

The actual detected frequency f (as explained in section 2.3.1) which is shown in figure 4.10 as the dashed white line is related to the energy distribution in the spectra. When we have a well defined energy peak, the detected frequency is corresponding very well as in the case of wire A1 in figure 4.10(a). When the spectrum is dominated by the modulation with the two energy peaks, the detected frequency is closer to the frequency of the stronger peak as can be seen for wire A2 in figure 4.10(b). However, regardless of the subtle differences of the energy distribution in the spectra between different hot wire probes, the detected frequencies are in good agreement between each other.

4.2.2 Mean flow measurements

For each vertical position of the control cylinder at $x_c/D = 0.4$, we perform a PIV acquisition and extract the mean streamwise velocity \bar{u} , mean component of vorticity in xOy plane $\bar{\omega}_z$ and the Reynolds stresses $\overline{v'^2}$ and $\overline{u'v'}$. Due to the symmetry of the effects on the global properties, confirmed by the frequency sensitivity maps, we perform PIV measurements only when the control cylinder is placed in the lower half of the wake, $0.08 > y_c/D > -0.82$, in steps of $0.02D$. This gives us the information about 45 flows, corresponding each to a different position of the control cylinder. At the same time, we have frequency and base pressure measurements for each position, obtained from the sensitivity maps.

The study of all of these flows leads to a classification into five typical configurations: *RF* for reversed flow, *IS* for inner shear, *MS* for mid-shear, *OS* for outer shear and *EF* for external flow. A configuration is defined from the longitudinal velocity \bar{u} surrounding the control cylinder at its relative position with regard to the closest detached shear layer from the main cylinder. The figure 4.11 shows the vertical profiles of $\bar{u}(y)$ taken at $x/D = 0.44$ for each position of the control cylinder. In this representation it is easy to distinguish the *RF* configuration where the velocity is negative. The other configurations will be clarified in the following.

Mean fields of the longitudinal velocity \bar{u} and vorticity $\bar{\omega}_z$ are respectively plotted in figures 4.12(a-b) for $d = 1mm$ and in figures 4.13(a-b) for $d = 3mm$. For both cylinders, typical cases of each configuration are shown in these figures, but they are described in the following paragraph independently from the control cylinder's size.

In the *RF* configuration, the control cylinder is surrounded by a negative longitudinal mean velocity. It is located inside the isoline $\bar{u} = 0$ in figures 4.12(a) and 4.13(a) and illustrated by the position $y_c/D = 0$ of the control cylinder. This configuration will be addressed to in

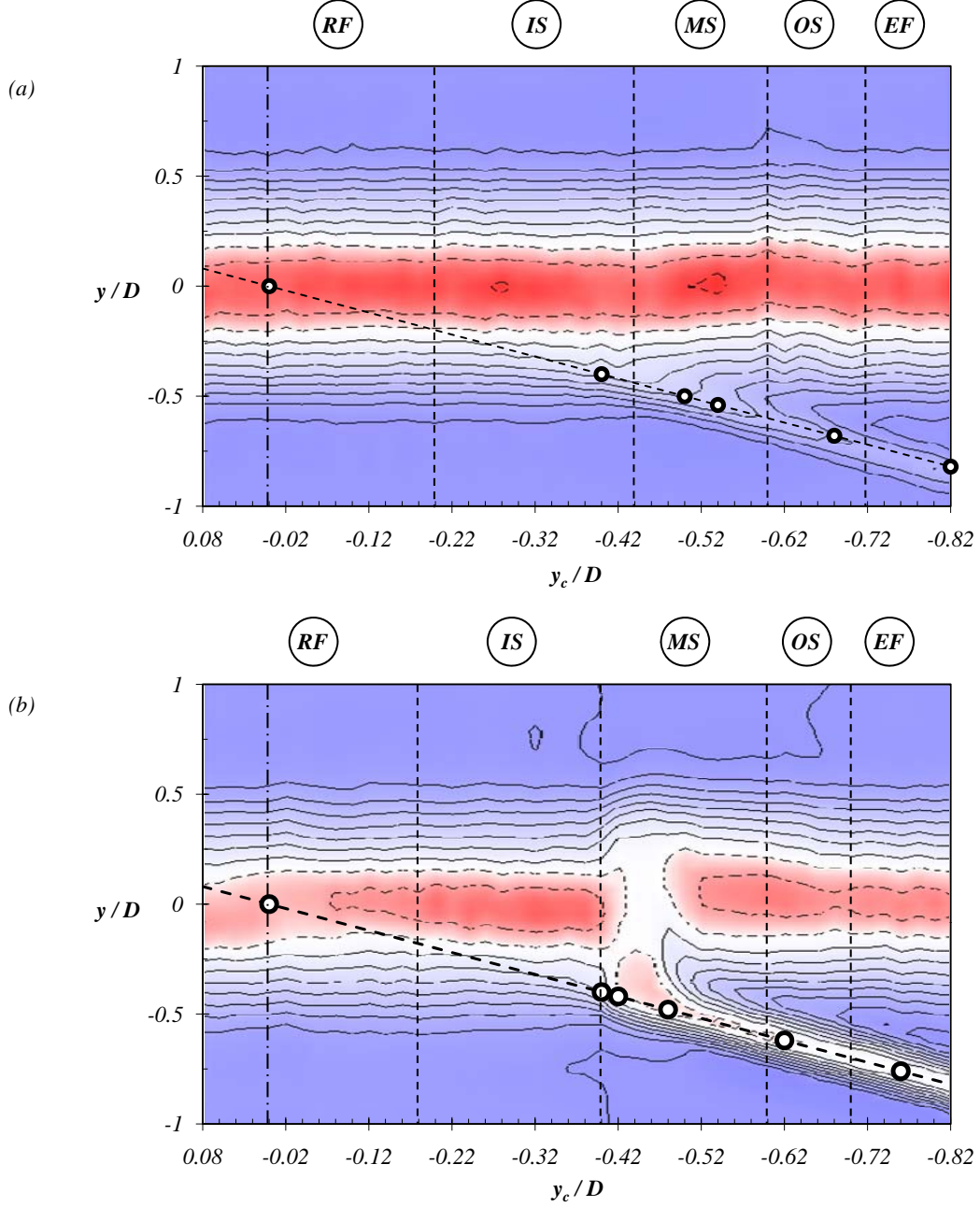


Figure 4.11: Sequence of mean streamwise velocity $\bar{u}(y, x = 0.44D, y_c)$, for the (a) 1mm control cylinder, and (b) 3mm control cylinder, showing the streamwise velocity profile across the wake, downstream of the control cylinder ($x_c/D = 0.4, y_c$). The continuous lines denote positive and dashed lines negative values, from the list $[-3, -2, -1, -0.5, 0, 0.5, 1, 2 \dots 8]m/s$. The thick dashed line denotes the path of the control cylinder across the wake, and circles represent the positions of the control cylinder presented in figures 4.12 and 4.13. Notation *RF*, *IS*, *MS*, *OS* and *EF* refers to configurations defined in section 4.2.2.

4. WAKE WITH A CIRCULAR CONTROL CYLINDER

section 4.3, where we look in detail at what happens when the cylinder is on the horizontal axis of the wake.

In the *IS* configuration, the control cylinder crosses the $\bar{u} = 0$ contour line and starts to see the positive velocity of the recirculation bubble, and partly the high velocity of the shear. A major ingredient of this configuration is that the totality of the shear layer detached from the main cylinder lies on one side of the control cylinder, which is an equivalent of it being reattached. This is depicted in figure 4.12(b) or in figure 4.13(b) for $y_c/D = -0.4$. For this configuration, the control cylinder concentrates the vorticity of the primary shear. This is observable on both figures because the intermediate isoline at $+1000s^{-1}$ of the controlled shear, extends further downstream than the isoline at $-1000s^{-1}$ from the unaffected shear.

In the *MS* configuration, the shear layer detached from the main cylinder is split by the control cylinder. This is case for positions $y_c/D = -0.5$ and $y_c/D = -0.54$ for the *1mm* control cylinder in figure 4.12(b) and for positions $y_c/D = -0.42$ and $y_c/D = -0.48$ for the *3mm* control cylinder in figure 4.13(b). One part of the shear is reattached on the control cylinder, and another part is deviated between the control cylinder and the trailing edge of the main cylinder. In addition to this split, some vorticity of opposite sign is created by the control cylinder. This is best observed for the *3mm* control cylinder at $y_c/D = -0.48$. This shear of opposite sign of vorticity together with the primary shear that is deviated inside the recirculating region creates a jet oriented toward the interior of recirculating region. The jet is also observable in the corresponding field of the longitudinal velocity (figure 4.13a, $y_c/D = -0.48$). The vorticity, contained in the split part of the primary shear that is not deviated, is much more concentrated than that of the unaffected shear. This is observed in the vorticity isolines, similar as for the *IS* configuration.

In the *OS* configuration the primary shear is no longer split, but still interacts with the shear of opposite sign created by the control cylinder, which is now in a region of large streamwise velocity. Due to the interaction, there is some vorticity cancellation in the controlled shear (see $y_c/D = -0.68$ in figure 4.12b and $y_c/D = -0.62$ in figure 4.13b). In case of the *3mm* diameter control cylinder, the recirculation region is significantly deformed, squeezed vertically and elongated horizontally as shown in figure 4.13(a) for $y_c/D = -0.62$.

Finally in the *EF* configuration, the control cylinder is far enough to the primary shear to not have any direct vorticity interaction. However, \bar{u} and $\bar{\omega}_z$ still show slight effects of the control cylinder. For the case of $d = 3mm$, we can observe subtle displacement of the mean bubble upwards, and slight reduction of the $\bar{\omega}_z$ in the bottom primary shear.

4.2.3 Reynolds stress envelope

In this section, we study the main features of the spatial structure of both Reynolds stresses $\overline{v'^2}$ and $\overline{u'v'}$ for each flow configuration. They are presented in figure 4.14 for the *1mm* control cylinder and in figure 4.15 for the *3mm* control cylinder.

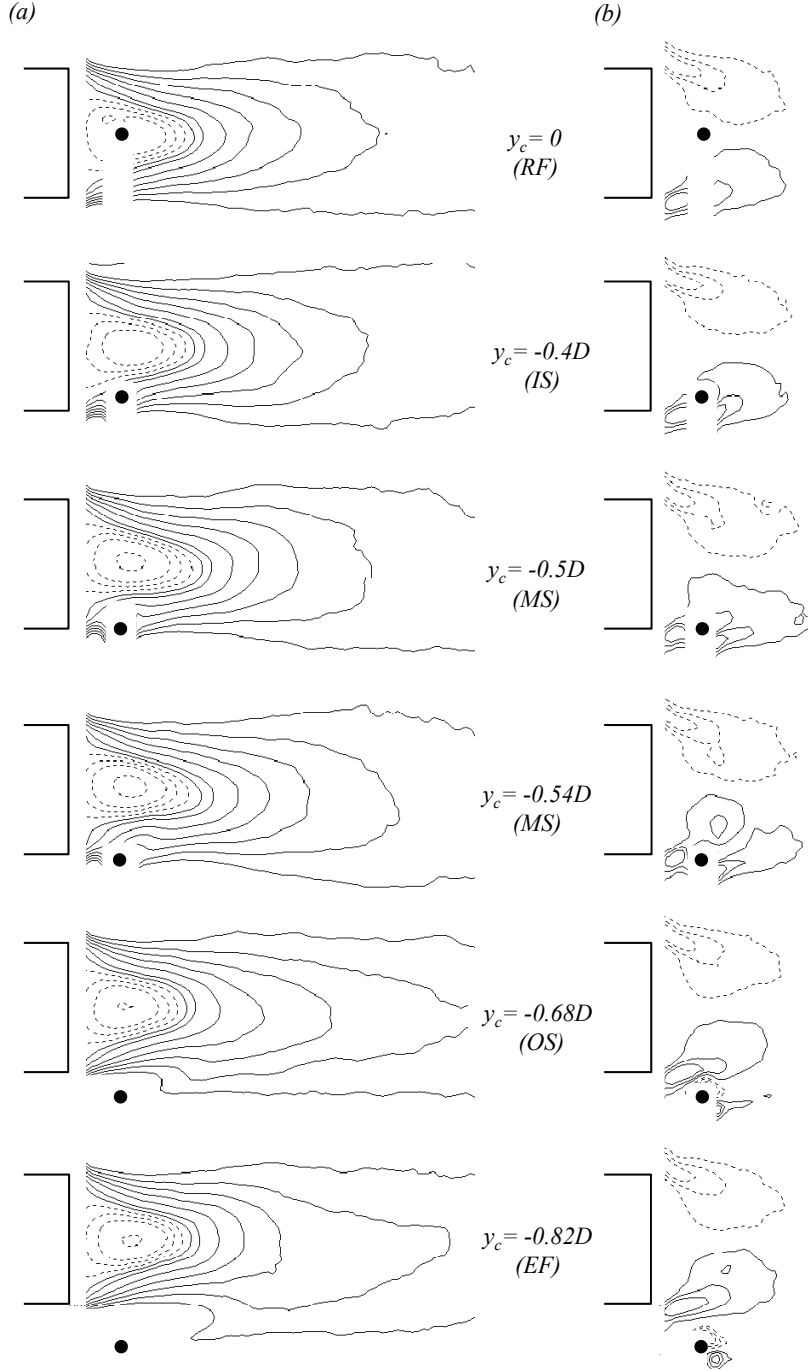


Figure 4.12: Flow for characteristic positions of the 1mm control cylinder, presented as mean streamwise velocity, \bar{u} (a) with continuous lines for positive and dashed lines for negative values, from the list $[-3, -2, -1, -0.5, 0, 0.5, 1, 2 \dots 8] \text{m/s}$; and mean vorticity $\bar{\omega}_z$ (b), where lines are at $\pm 500, \pm 1000$ and $\pm 1500 \text{s}^{-1}$ (continuous for positive, and dashed for negative vorticity). Notation *RF*, *IS*, *MS*, *OS* and *EF* refers to configurations defined in section 4.2.2.

4. WAKE WITH A CIRCULAR CONTROL CYLINDER

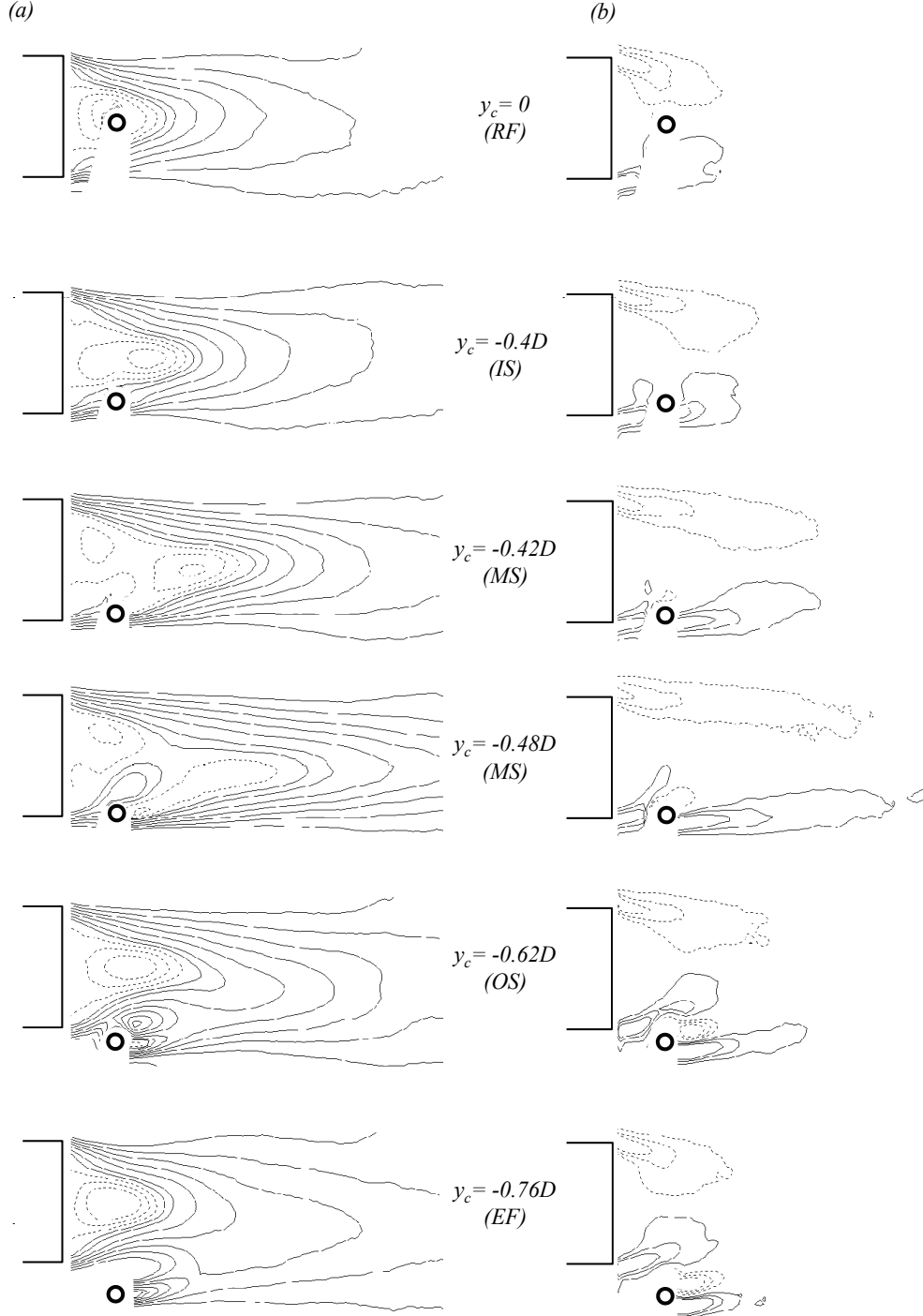


Figure 4.13: Flow for characteristic positions of the 3mm control cylinder, presented as mean streamwise velocity, \bar{u} (a) (a) with continuous lines for positive and dashed lines for negative values, from the list $[-3, -2, -1, -0.5, 0, 0.5, 1, 2 \dots 8] \text{ m/s}$; and mean vorticity, $\bar{\omega}_z$ (b), isolines are at $\pm 500, \pm 1000$ and $\pm 1500 \text{ s}^{-1}$ (continuous for positive, and dashed for negative vorticity). Notation *RF*, *IS*, *MS*, *OS* and *EF* refers to configurations defined in section 4.2.2.

For the case of the $1mm$ control cylinder some subtle changes can be observed in MS configuration for which the maxima of $\overline{v'^2}$ (figure 4.14a) is badly defined and its amplitude reduced. For the same configuration, we can see that the maxima of $\overline{u'v'}$ (figure 4.14b) are slightly shifted downstream and their amplitudes also reduced.

We can observe in figure 4.15(a-b) that the $3mm$ control cylinder makes a much bigger impact on the Reynolds stresses. We can clearly observe that the maximum of $\overline{v'^2}$ starts to shift downstream for configuration IS as for the extrema of $\overline{u'v'}$. In configuration MS , the extrema are shifted even further and we can observe also that the amplitude is being drastically reduced. The whole envelope of the Reynolds stress structure is completely damped and displaced downstream for the flow where the jet is most visible, at $y_c/D = -0.48$. As the control cylinder exits the recirculating bubble for position OS , we can see that the locations of the extrema are gradually returning closer to the trailing edge of the main cylinder and their amplitudes are increasing. Finally, for the configuration EF we can observe only slight modifications to the amplitudes and locations of the extrema compared to the RF case. The secondary vortex street created by the $3mm$ control cylinder is clearly seen which is not the case with the $1mm$ control cylinder because of the PIV coarse graining.

As we can see, some special features relevant for the global spatial structure sensitivity of the Reynolds stresses are the locations of the extrema and their amplitudes. In the case of $\overline{v'^2}(x, y)$, the fluctuations associated to the vortex shedding from the primary cylinder is indicated by the maximum on the center line, while it is indicated by the two extrema of opposite amplitudes symmetrically located with respect to the horizontal axis in the $\overline{u'v'}(x, y)$ fields (see for example, RF configuration for $y_c/D = 0$ in figure 4.14a-b). Their amplitudes, $\overline{v'^2}_{Max}$, $\overline{u'v'}_{Max}$, $\overline{u'v'}_{Min}$ and respective abscissas $X_{\overline{v'^2}_{Max}}$, $X_{\overline{u'v'}_{Max}}$, $X_{\overline{u'v'}_{Min}}$ as well as the recirculation bubble length L_b are plotted in figure 4.16(a-e) for the $1mm$ control cylinder and in figure 4.17(a-e) for the $3mm$ control cylinder.

For all the positions of the $1mm$ control cylinder, the relative positions of the three extrema are always similar (figure 4.16a-b). The only significant change is the slight displacement of these positions in the MS configuration corresponding to a downstream shift of the spatial structure of the Reynolds stresses. It is also correlated to an increase of the mean bubble length L_b (figure 4.16e). Correspondingly, the amplitudes of the Reynolds stresses extrema are damped, very significantly for $\overline{v'^2}_{Max}$ in figure 4.16(c) but only a hint of attenuation is visible for $\overline{u'v'}_{Max}$ and $\overline{u'v'}_{Min}$ in figure 4.16(d). The reduction of the mean bubble length L_b observed in OS configuration in figure 4.16(e), is associated to an upstream shift of the abscissa $X_{\overline{v'^2}_{Max}}$, $X_{\overline{u'v'}_{Max}}$ and $X_{\overline{u'v'}_{Min}}$ (see figure 4.16 a-b). In this case, there is an upstream shift of the spatial structure of the Reynolds stresses. On the other hand, there is no clear corresponding effects to this shift in the amplitudes of the extrema in figure 4.16(c-d).

In the case of the $3mm$ control cylinder in RF and IS configurations, the abscissas of the extrema in figure 4.17(a-b) remain mostly unchanged indicating that the Reynolds stresses structure is conserved. In MS configuration, the abscissas are significantly shifted downstream

4. WAKE WITH A CIRCULAR CONTROL CYLINDER

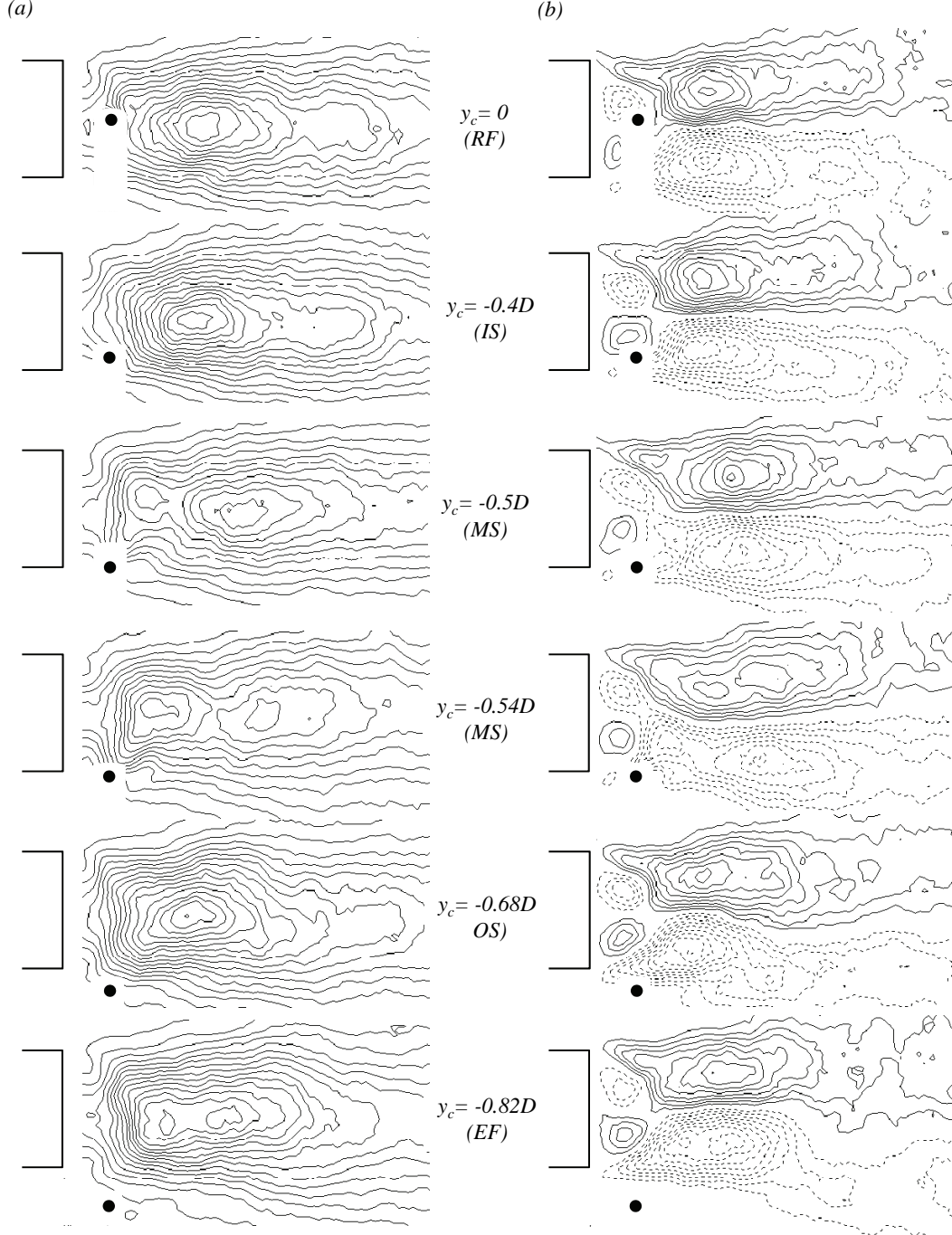


Figure 4.14: Components of the Reynolds stresses for characteristic positions of the 1mm control cylinder: $\overline{v'^2}$, in range of $0(m/s)^2$ to $15(m/s)^2$ (a), and $\overline{u'v'}$, in range of $\pm 5(m/s)^2$ (b). The isolines are in the interval of $1(m/s)^2$ (continuous lines for positive and dashed for negative values). Notation *RF*, *IS*, *MS*, *OS* and *EF* refers to configurations defined in section 4.2.2.

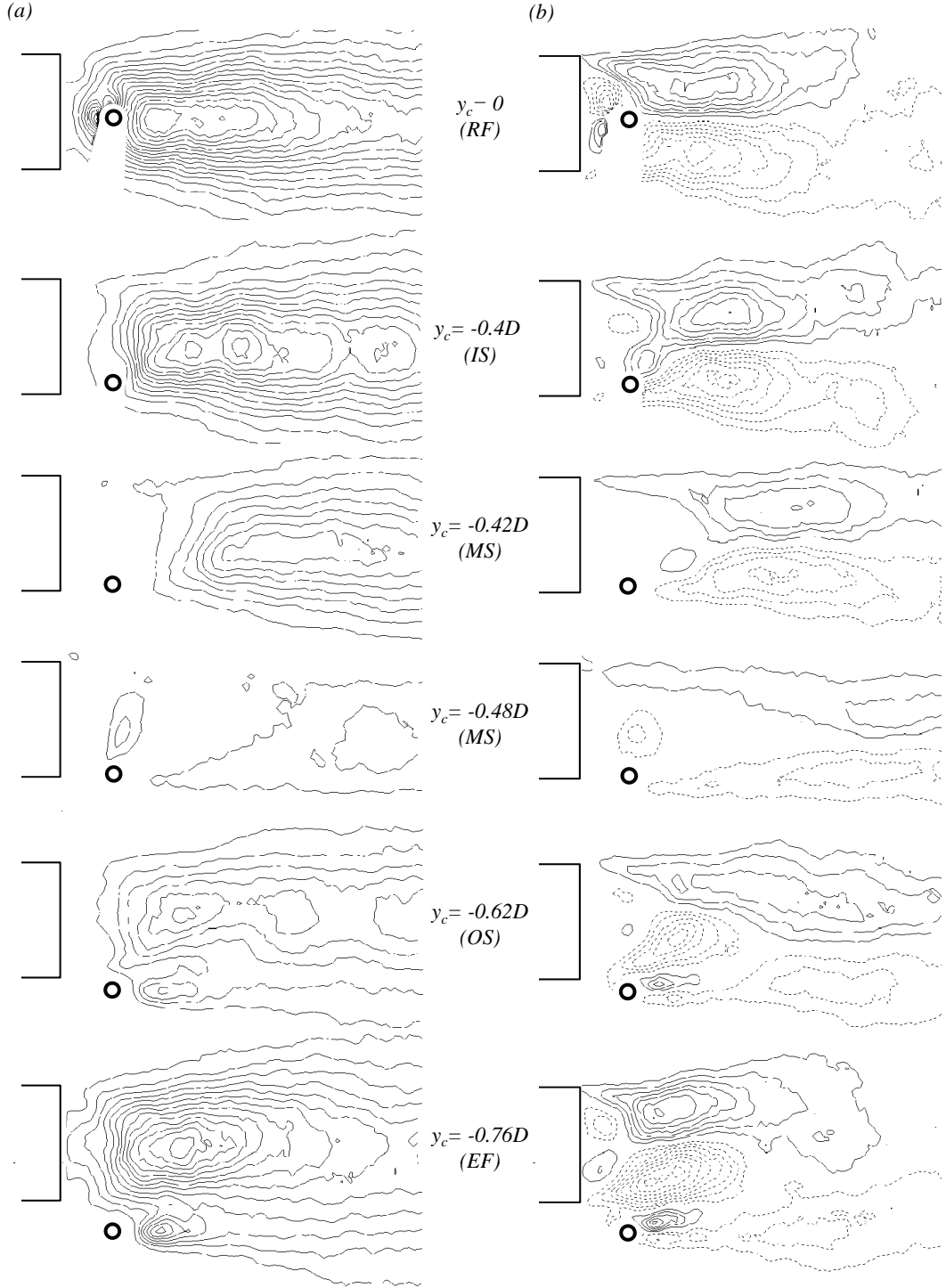


Figure 4.15: Components of the Reynolds stresses for characteristic positions of the 3mm control cylinder: v'^2 , in range of $0(m/s)^2$ to $15(m/s)^2$ (a), and $\overline{u'v'}$, in range of $\pm 5(m/s)^2$ (b). The isolines are in the interval of $1(m/s)^2$ (continuous lines for positive and dashed for negative values). Notation *RF*, *IS*, *MS*, *OS* and *EF* refers to configurations defined in section 4.2.2.

4. WAKE WITH A CIRCULAR CONTROL CYLINDER

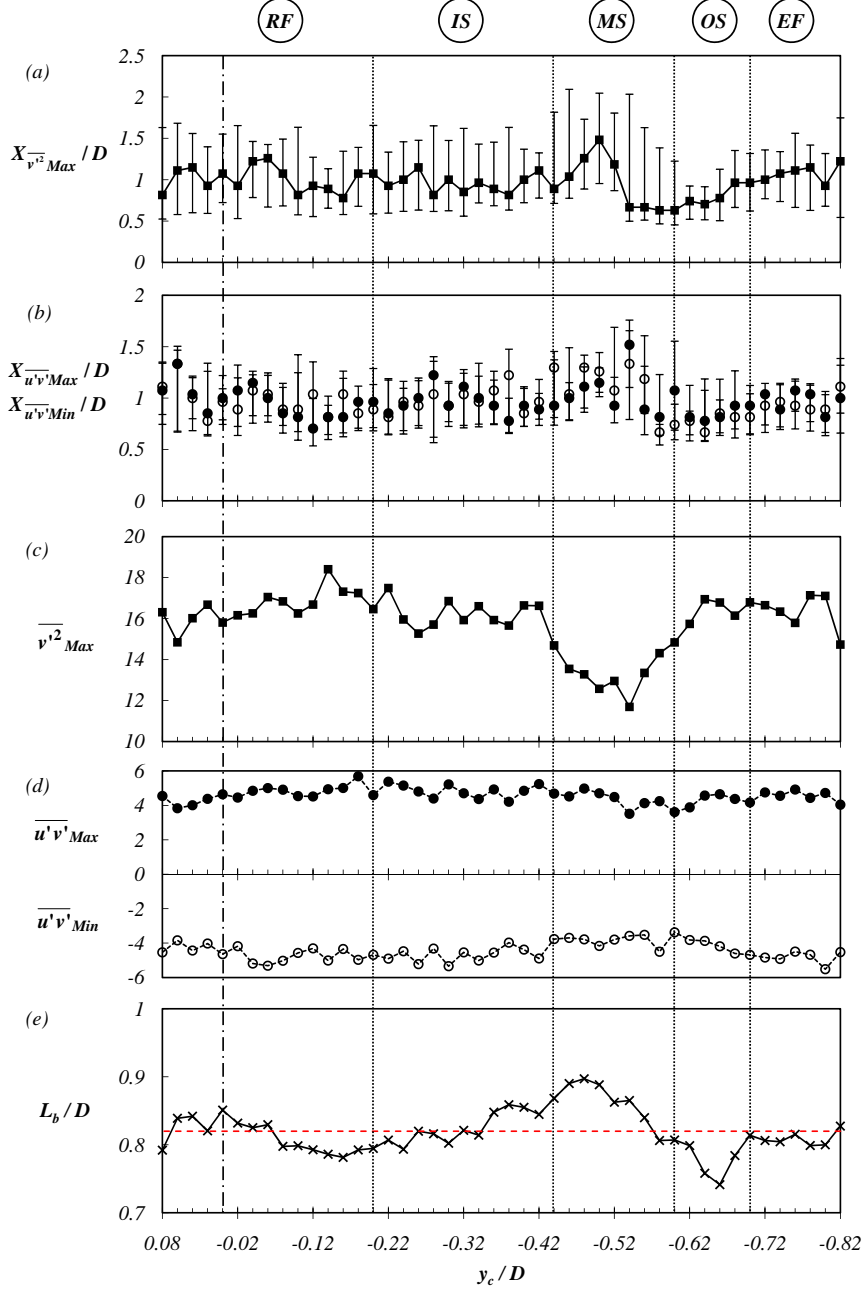


Figure 4.16: Amplitudes and streamwise locations of the extrema of Reynolds stress components $\overline{v'^2}(x,y)$ and $\overline{u'v'}(x,y)$ for positions of the 1mm control cylinder ($x_c/D = 0.4$, $-0.82 < y_c/D < 0.08$): (a) position of the maximum of $\overline{v'^2}$, (b) position of the maximum (filled circles) and the minimum (empty circles) of $\overline{u'v'}$, (c) amplitude of the maximum of $\overline{v'^2}$, (d) amplitudes of the maximum (filled circles) and the minimum (empty circles) of $\overline{u'v'}$ and (e) size of the recirculation bubble L_b/D . Notation *RF*, *IS*, *MS*, *OS* and *EF* refers to configurations defined in section 4.2.2. Error bars denote the streamwise length of the first iso-line around the maximum (see figure 4.14).

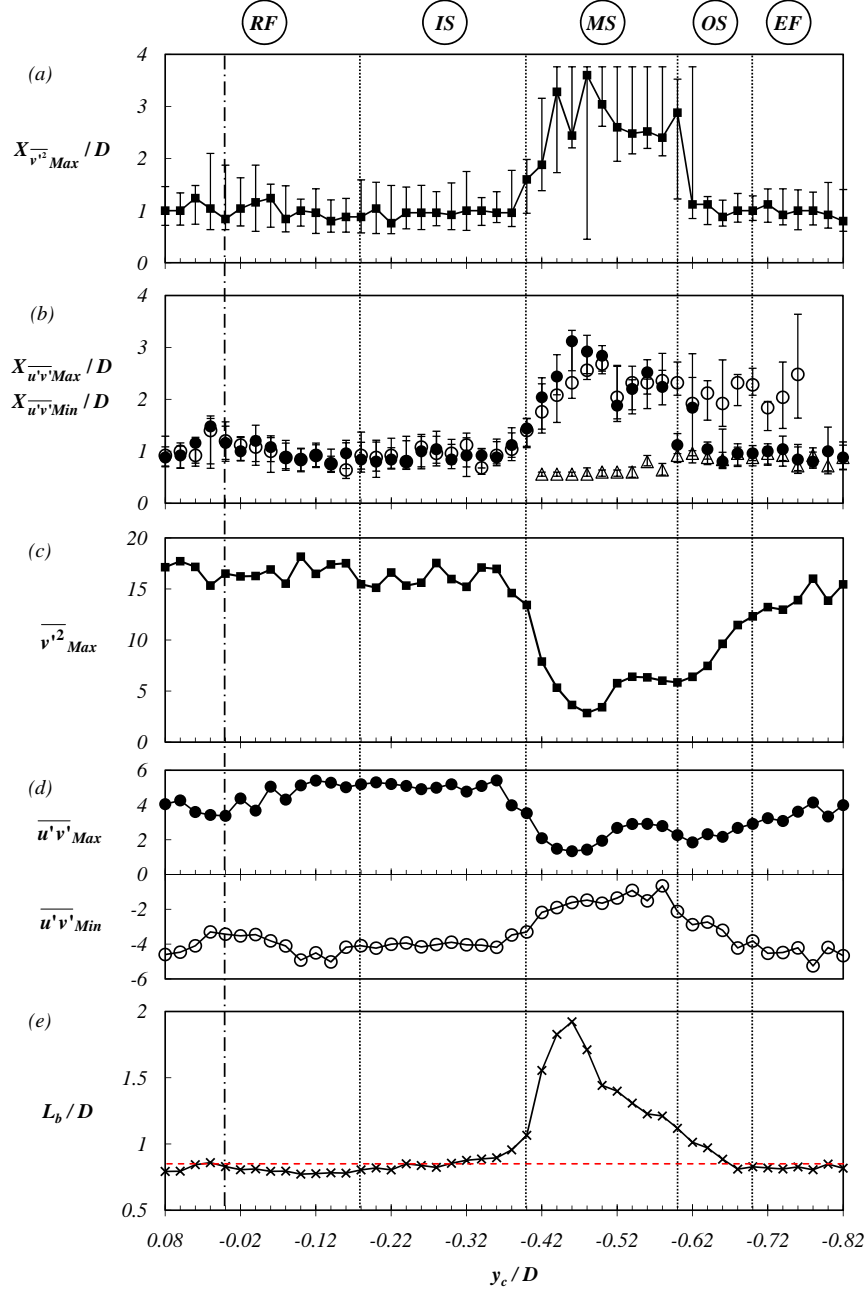


Figure 4.17: Amplitudes and streamwise locations of the extrema of Reynolds stress components $\overline{v'^2}(x, y)$ and $\overline{u'v'}(x, y)$ for positions of the $3mm$ control cylinder ($x_c/D = 0.4$, $-0.82 < y_c/D < 0.08$): (a) position of the maximum of $\overline{v'^2}$, (b) position of the maximum (filled circles) and the minimum (empty circles) of $\overline{u'v'}$, (c) amplitude of the maximum of $\overline{v'^2}$, (d) amplitudes of the maximum (filled circles) and the minimum (empty circles) of $\overline{u'v'}$, the second minimum (triangles) appears in figure 4.15(b) for $y_c/D = -0.48$. Size (e) of the recirculation bubble L_b/D . Notation RF , IS , MS , OS and EF refers to configurations defined in section 4.2.2. Error bars denote the streamwise length of the first isoline around the maximum (see figure 4.15).

4. WAKE WITH A CIRCULAR CONTROL CYLINDER

and a third extremum in $\overline{v'u'}(x, y)$ (denoted as triangles in figure 4.17b) with a nearly constant streamwise location is observed. The presence of this extremum is due to the shear splitting (major ingredient of the *MS* configuration) and directly related to the part entering the recirculation region. This is clearly seen in figure 4.15(a-b) for position $y_c/D = -0.48$ as the isolated extremum of $\overline{v'^2}(x, y)$ and negative $\overline{v'u'}(x, y)$ located above the control cylinder. However, the vortex shedding is associated with the two extrema symmetrically located with respect to the horizontal axis, thus having the same abscissa. In *OS* configuration a significant transition is observed around $y_c/D = -0.6$ when the shear entering the recirculating region starts to couple with the upper shear to interfere with the vortex shedding. This is displayed in figure 4.17(b) when the upper shear extremum (denoted by filled circles) starts to shift its streamwise location x/D back, towards the position of the extremum produced by the jet (denoted by triangles), until they are symmetrically located with respect to the horizontal axis. For *MS* and *OS* configurations, the relevant extrema associated to vortex shedding are significantly displaced downstream by almost a factor of 3. This displacement is clearly correlated to an increase of the bubble length L_b (figure 4.17e) and also associated to a strong damping of all of the extrema of the Reynolds stresses as shown in figure 4.17(c-d).

4.3 Turbulent wake modifications with a control cylinder at $y_c/D = 0$

This set of experiments was originally intended to discover the reasons for the frequency increase when the control cylinder is placed at the *Ox* axis, in a limited range of positions, near $x_c/D = 0.4$, as can be seen on the frequency sensitivity maps for $d = 3mm$ in figure 4.2. The object of interest was the position $x_c/D = 0.48, y_c/D = 0$ which appears to be at the middle of this frequency enhancement region. Therefore, we have performed a study of how the wake is affected when the control cylinder is displaced along the horizontal axis of symmetry. For this instance, we have actually used the $d = 4mm$ circular control cylinder, and all PIV acquisitions have been made with the high-speed setup. In an effort to discern in detail the dynamics in the recirculation bubble itself, the bigger cylinder was used in the hope that it would accentuate the mechanisms that cause the frequency to change. The obtained velocity fields were examined as instantaneous, but also as phase-averaged, in order to focus on the dynamics at the frequency of the global mode, without the hindrance of turbulent noise. Together with the results from PIV, we will use results from mapping experiments with the $4mm$ control cylinder, which are presented in chapter 6.

4.3.1 Mean wake and Reynolds stress measurements

Similarly as for the control cylinder on a vertical line, we have performed PIV measurements of the wake for several positions on the *Ox* line. They are shown in figure 4.18(a) as streamwise

velocity \bar{u} , (b) as mean component of vorticity in xOy plane $\bar{\omega}_z$ and in figure 4.19(a) as the Reynolds stresses $\overline{v'^2}$ and (b) $\overline{u'v'}$.

From the \bar{u} fields (figure 4.18a) it is clearly seen that the recirculation bubble is following the control cylinder, as it is displaced downstream. The bubble increases its length until the control cylinder goes past $x_c/D = 1.04$, after which its length starts to reduce. In the Reynolds stress display (figure 4.19a-b) we can observe that there are no fluctuations characteristic of the vortex formation region upstream of the control cylinder, up to $x_c/D = 1.04$; all of the fluctuations are downstream which confirms that the bubble encompasses the control cylinder. For the position of $x_c/D = 1.2$ we can observe a bubble decrease and that the fluctuations are present both upstream and downstream of the control cylinder, revealing a primary vortex shedding from the main cylinder, and a secondary formation region from the control cylinder.

We can conclude that the shear layers tend to delay roll-up, and interact between each other downstream of the control cylinder, when the control cylinder is in a specific range of positions at the centerline of the wake. This range of positions is a region of roughly $0.4D$ in size, around of the streamwise location where the natural bubble is closed (see figure 4.3b).

4. WAKE WITH A CIRCULAR CONTROL CYLINDER

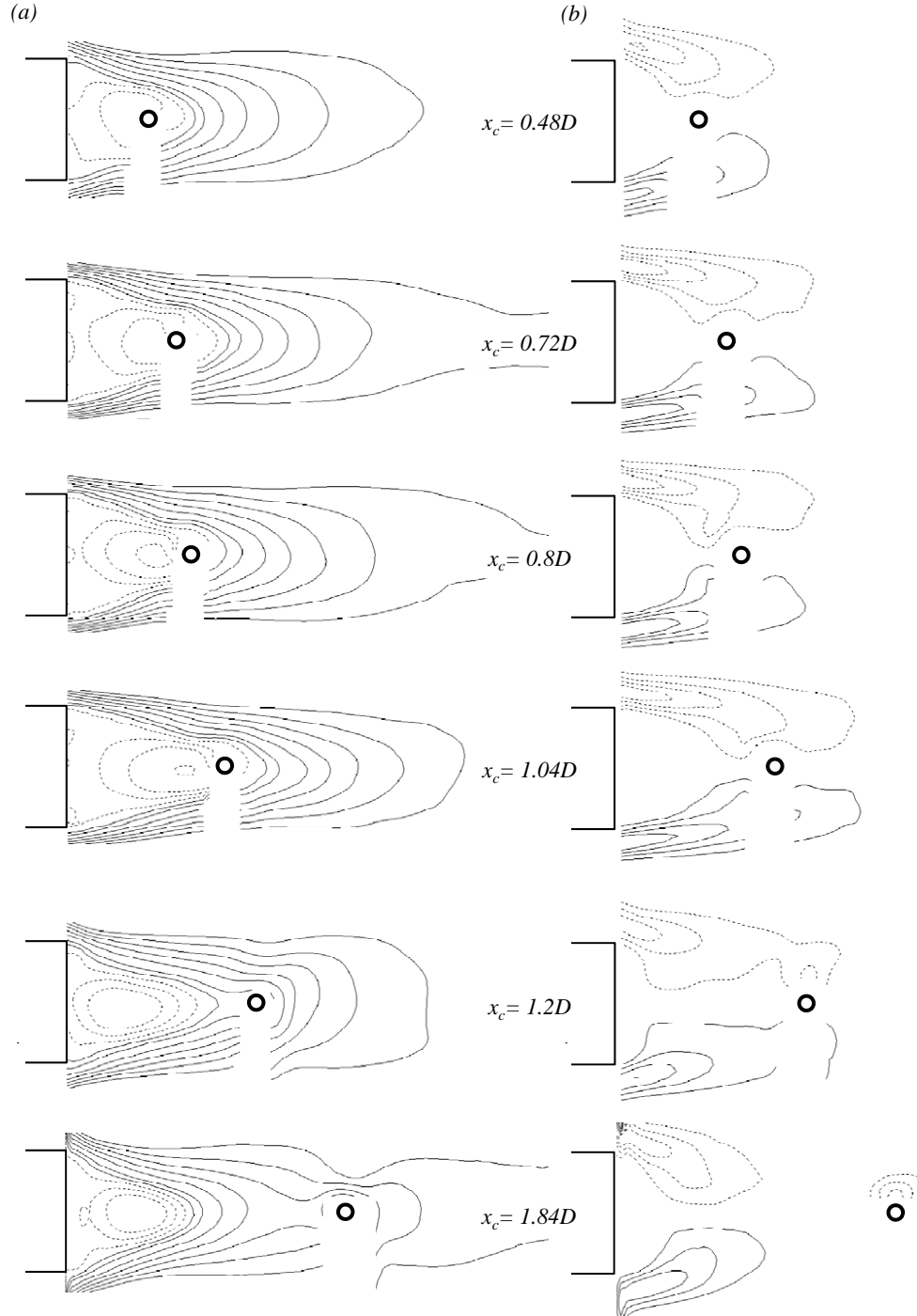


Figure 4.18: Flow for positions of the 4mm control cylinder on the horizontal axis Ox , presented as mean streamwise velocity, \bar{u} (a) with continuous lines for positive and dashed lines for negative values, from the list $[-3, -2, -1, -0.5, 0, 0.5, 1, 2 \dots 8] \text{ m/s}$; and mean vorticity $\bar{\omega}_z$ (b), where lines are at $\pm 500, \pm 1000$ and $\pm 1500 \text{ s}^{-1}$ (continuous for positive, and dashed for negative vorticity).

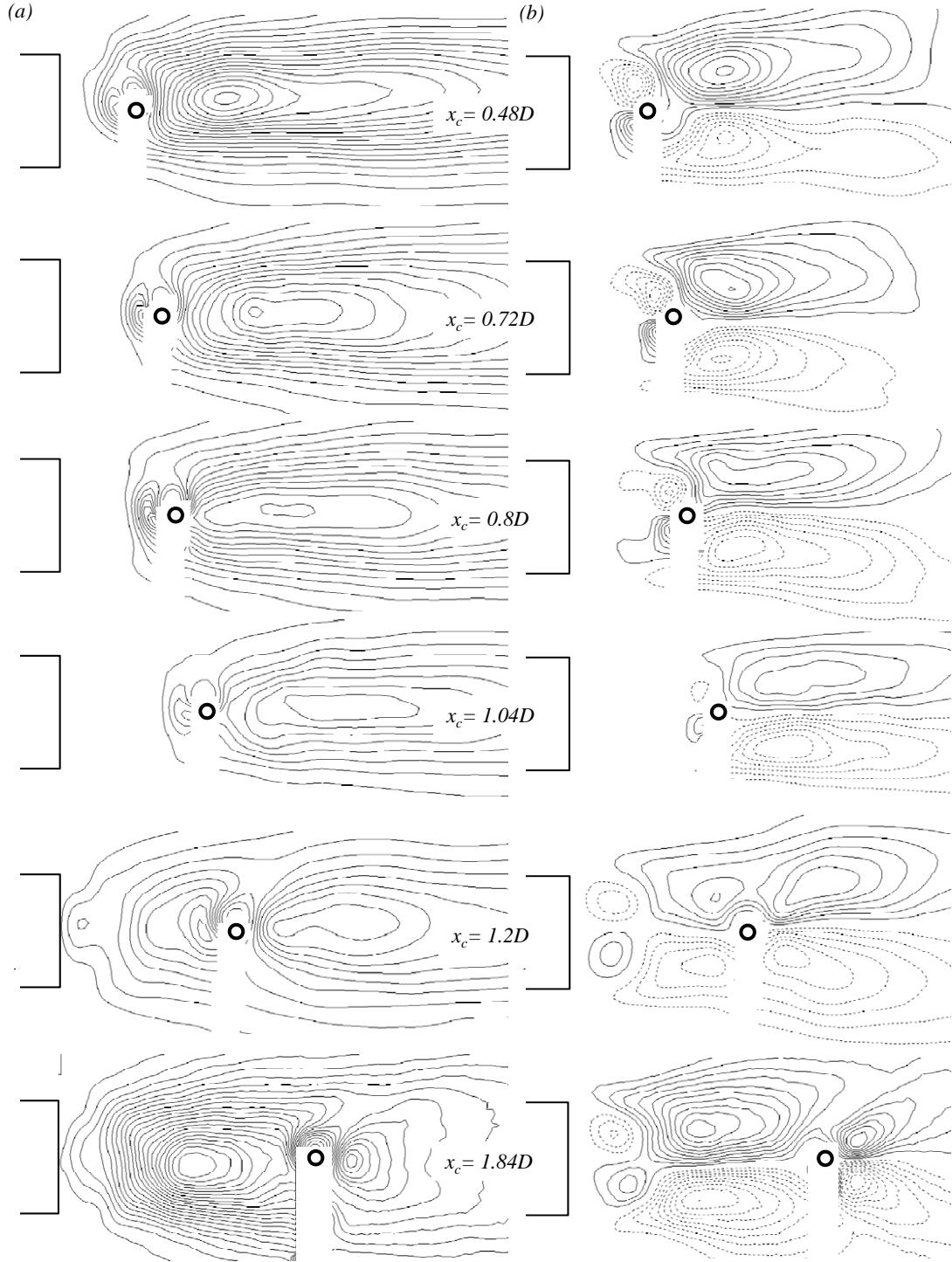


Figure 4.19: Components of the Reynolds stresses for characteristic positions of the 4mm control cylinder on the horizontal axis Ox : $\overline{v'^2}$, in range of $0(m/s)^2$ to $15(m/s)^2$ (a), and $\overline{u'v'}$, in range of $\pm 5(m/s)^2$ (b). The isolines are in the interval of $1(m/s)^2$ (continuous lines for positive and dashed for negative values).

4.4 The mechanisms of wake modification

Based on the presented results in previous sections, we will now discuss and propose possible mechanisms that are responsible for the global mode frequency selection, global mode amplitude and spatial structure, mean wake modifications and base pressure changes.

4.4.1 Global frequency selection

Direct vorticity interaction

The nature of change of the vorticity distribution in the shear layers can be observed in figure 4.20. Here we present three characteristic positions of the $d = 3mm$ circular cylinder: positions (a) and (b) are configurations *IS* and *OS* respectively, at $x_c/D = 0.4$, while position (c) belongs to a configuration type *IS*, but is taken further downstream at $x_c/D = 0.64$. Each position shows a mean $\bar{\omega}_z$ field, with two vertical profiles of $|\bar{\omega}_z|$ extracted at the streamwise points indicated by the dashed lines. The blue dashed line $A - A$ represents a vorticity profile upstream of the control cylinder, when the shear layers have just detached from the trailing edge of the main cylinder, and is taken at the same x for all three cases. The red dashed line $B - B$ is a profile taken just downstream of the control cylinder. Vorticity profiles in figure 4.20(a) clearly shows that the shears upstream are symmetric and vorticity distributions are identical, while downstream profiles reveal how the controlled shear is thinner, thus with more vorticity than the upper shear. Profiles in figure 4.20(b) show a reduction of vorticity in the controlled shear, expected for an *OS* case. The whole wake is deformed due to the flow displacement caused by the control cylinder, but we can still observe this difference between the two shears. In figure 4.20(c), we go back to a constructive effect on vorticity on for the controlled shear. The difference between the two shears is here even more pronounced, since the lower shear is "supported" by the control cylinder, and the upper shear is left completely without any direct influence, yet it adapts to the extended length of lower shear simply due to the Biot and Savart law. The selected frequency for cases $IS_{0.4}$ and $IS_{0.64}$ is $St_{(0.4)} = 0.237$ and $St_{(0.64)} = 0.256$ which makes around 8% of difference between the two. This difference is of the same order of magnitude as the difference in levels of maximum vorticity in the controlled shear for both cases, as illustrated by a higher maximum for the $B - B$ profile of the $IS_{0.64}$ case.

The high-speed PIV acquisitions have enabled us to see in more detail, what happens in these cases by using snapshots of instantaneous vorticity fields and time signal of vorticity at specific key points in the shear layers. Similarly as above, we observe one point upstream of the control cylinder and one point downstream. However, in this case, we will compare $\omega_z(t, x, y)$ for the upper and lower shear, and for the three cases of control cylinder position. The three positions are the same as in the previous analysis, and are shown in figure 4.21. The colors of the time signal correspond to the measurement point x location, blue for upstream and red for measurements downstream of the control cylinder. Both measurements for the upper shear are shown together in the top window, and measurements from the bottom shear in the bottom

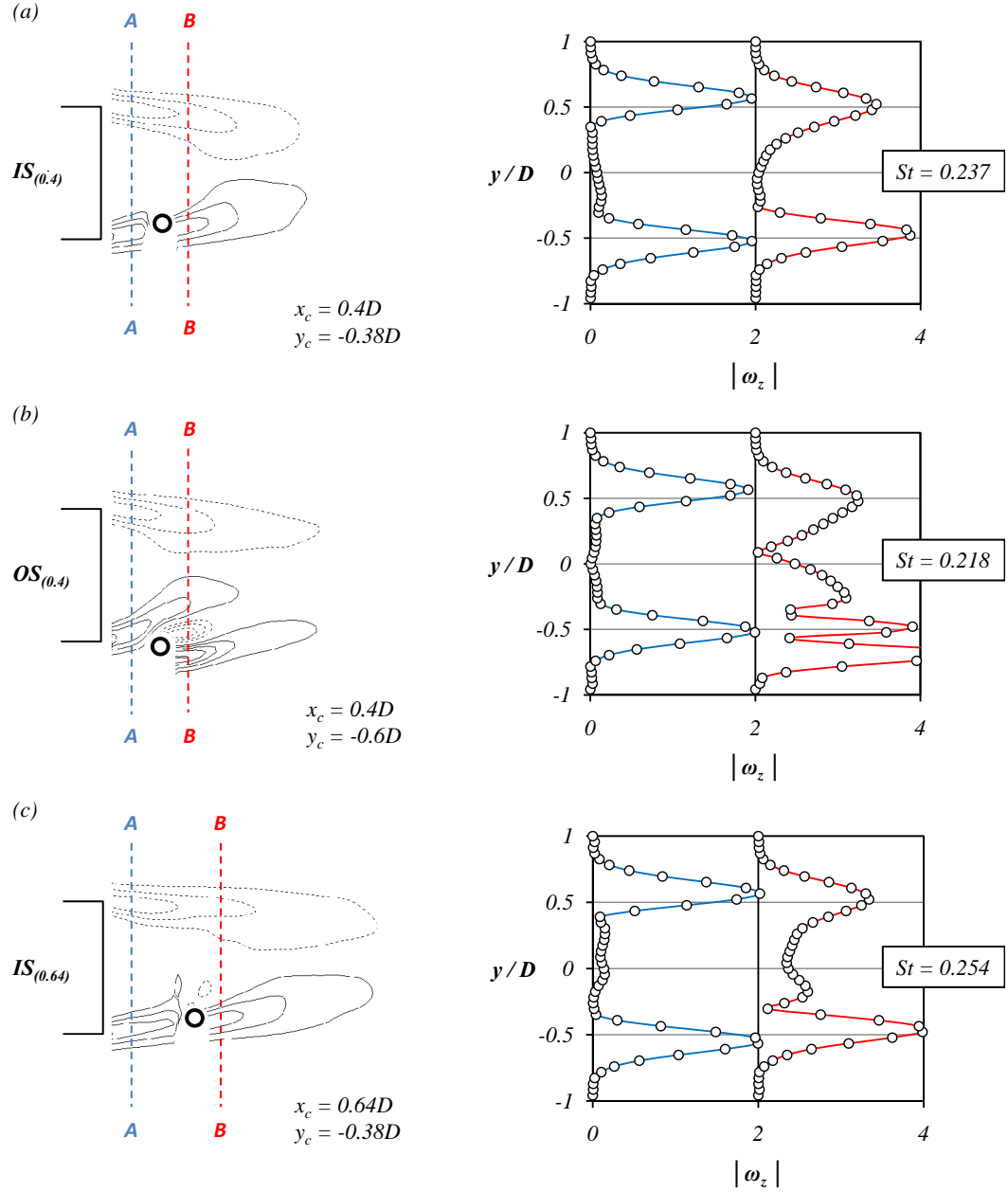


Figure 4.20: Profiles of mean vorticity $\bar{\omega}_z$ upstream (A-A) and downstream (B-B) of the control cylinder, for three positions (x_c, y_c) : (a) $0.4D, -0.38D$, (b) $0.4D, -0.6D$ and (c) $0.64D, -0.38D$.

4. WAKE WITH A CIRCULAR CONTROL CYLINDER

| Position | | $IS_{0.4}$ | | $OS_{0.4}$ | | $IS_{0.64}$ | |
|--------------------|-----------------------|------------|----------|------------|----------|-------------|----------|
| <i>Shear layer</i> | | <i>A</i> | <i>B</i> | <i>A</i> | <i>B</i> | <i>A</i> | <i>B</i> |
| <i>Upper</i> (1) | $\overline{\omega_z}$ | -1.946 | -1.404 | -1.908 | -1.223 | -1.903 | -1.167 |
| | σ_{ω_z} | 0.186 | 0.289 | 0.204 | 0.419 | 0.220 | 0.352 |
| <i>Lower</i> (2) | $\overline{\omega_z}$ | 1.951 | 1.869 | 1.989 | 0.931 | 1.488 | 1.795 |
| | σ_{ω_z} | 0.239 | 0.289 | 0.237 | 0.754 | 0.230 | 0.248 |

Table 4.1: Values of mean $\overline{\omega_z}$ and fluctuating vorticity σ_{ω_z} in the upper and lower shear layer, measured at positions upstream (*A*) and downstream of the control cylinder (*B*).

window of each position in figure 4.21(a), (b) and (c). This is perhaps the best way to show the effects of the shear layer/control cylinder interaction, and how the shear is stabilized and its vorticity increased for the *IS* positions, and how its fluctuations are markedly increased in the case of *OS* configuration. In the $OS_{0.4}$ case, we can see that the first half of the B_2 signal is more steady than the second half. This is because the second half of the velocity signal captures the oscillations of the vortex street from the control cylinder. In any case the part of the signal which shows only the oscillation of vorticity in the primary shear, clearly indicates the destabilization of this shear. The $IS_{0.64}$ case shows an increase in vorticity between points A_2 and B_2 , while vorticity between same two measurement points in the case of $IS_{0.4}$ is only conserved due to the control cylinder. Of course, both cases show shear stabilization as it is clearly visible that the fluctuations of vorticity are reduced in the controlled shear. Exact values of mean and standard deviation of each vorticity time signal can be found in table 4.1 for comparison.

Vorticity feedback mechanism

When the control cylinder is in *RF* configuration, the Strouhal maps of $3mm$ in figure 4.2 and $3mm$ and $4mm$ control cylinders in figure 6.3(a), show a frequency maximum around $x_c/D = 0.5$. What is the origin of this local maximum?

Figure 4.22 shows three frames of phase-averaged vorticity when the control cylinder is placed at $x_c/D = 0.56$. These three vorticity fields help us see what is causing the frequency increase. The first phase of this process is shown in figure 4.22(a) and shows that the control cylinder is directly in the path of an incoming roll-up vortex. In terms of the mean flow (see figure 4.11) it is in a region of reversed flow, and its downstream face "sees" a negative velocity coming from the shear roll-up around the control cylinder. In this particular case, the "blue" shear (negative vorticity) has just started its roll-up. We can still see a detached blue vortex from the previous cycle being advected downstream, while the red shear is in the full swing of his own cycle. So, the blue shear is rolling-up and is starting to impose some velocity on the surface of the control cylinder in the upstream direction. This velocity produces vorticity on the surface of the control cylinder, which is spread upstream, and is marked with blue and red dashed circles.

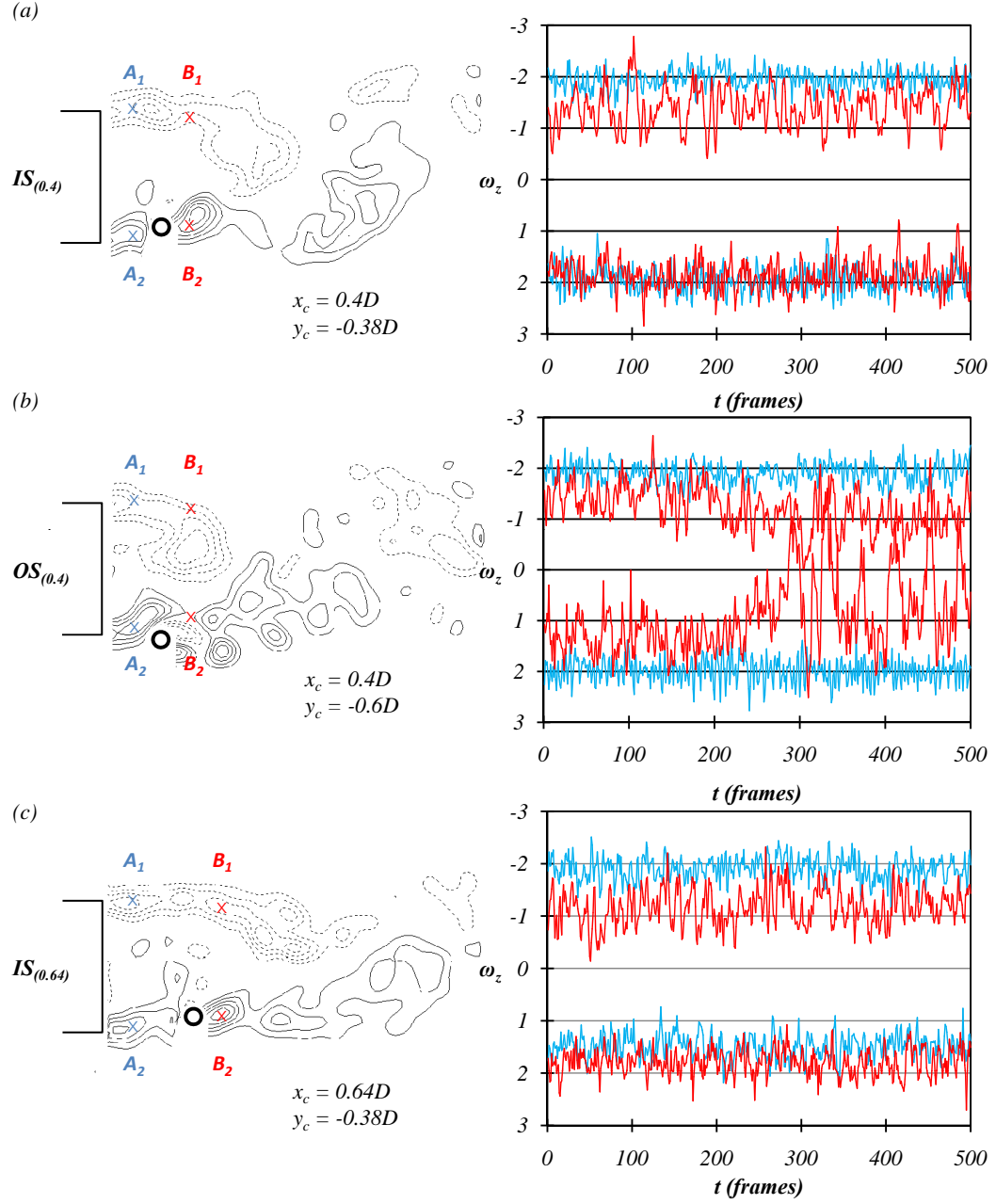


Figure 4.21: Snapshots (left) and time resolved (right) instantaneous vorticity ω_z , measured at four points in the wake, for three positions of the control cylinder (x_c, y_c) : (a) $0.4D, -0.38D$, (b) $0.4D, -0.6D$ and (c) $0.64D, -0.38D$. The measurement points upstream of the control cylinder are marked as A and their time signals shown in blue, while the measurement points downstream are marked as B and shown in red. Upper shear is referred to with index 1 and lower with index 2.

4. WAKE WITH A CIRCULAR CONTROL CYLINDER

In phase two, shown in figure 4.22(b), the vorticity from the control cylinder is being entrained into the blue shear. As we said, the blue shear is rolling up and this motion is capable of entraining the opposite shear, as explained by the law of Biot and Savart. The vorticity on the control cylinder is certainly much closer than the other shear and is naturally easy for the blue shear, or rather the forming blue vortex, to entrain. Another feature is that the velocities that are creating the vorticity are not in Ox direction (as mean velocity might imply), rather the vector of velocity and consequently the displacement of produced vorticity changes its direction, depending on the moment in the process of the primary shear roll-up.

At the peak of the cycle, both red and blue vorticity from the control cylinder are entrained in the blue roll-up, as shown in figure 4.22(c). The shear which is rolling up is weakened by the opposite vorticity (indicated by red arrows) and the shedding occurs faster and easier. Therefore, the effect on frequency comes not by direct interaction between the shear layers and the control cylinder, but by interaction of the control cylinder and the roll-up vortex. Vorticity, created this way, is advected upstream and affects the shear layers before their roll-up, effectively creating a "feedback" mechanism.

The feedback effect has not been observed in PIV measurements for the $1mm$ control cylinder. However, the Strouhal maps (see figure 4.1) show that there is a small maximum on the Ox axis, around $x_c/D = 0.4$. Therefore, we cannot make any conclusions about whether the $1mm$ control cylinder is big enough to make a feedback effect, but certainly the frequency increase in this characteristic region indicates that there is a weak feedback mechanism at play here.

Interpretation of frequency change

The global frequency is related to the vorticity distribution in the shear layers detached from the main cylinder which is influenced by the vorticity created from the control cylinder. Two mechanisms were observed, one due to a vorticity feedback in the RF configuration and the other due to a direct interaction corresponding to the IS , MS and OS configuration. In order to elucidate on these relationships, the vertical profiles of $\bar{\omega}_z(y)$ just downstream from the control cylinder, at $x/D = 0.44$ is extracted for all the positions of the control cylinder y_c . The obtained sequence $\bar{\omega}_z(y, x = 0.44D, y_c)$ is plotted respectively in figure 4.23(a) for the $1mm$ cylinder and figure 4.24(a) for the $3mm$ cylinder. The global frequency changes $\tilde{f}(y_c)$ is plotted in figure 4.23(b) for the $1mm$ control cylinder and figure 4.24(b) for the $3mm$ control cylinder. From the analysis of the extrema of the Reynolds stresses structure in section 4.4.2, it is sometimes possible to deduce which interacting shear layers are responsible for the vortex shedding (i.e. the global mode). They are marked by blue and red colored lines in the figure 4.23(a) and figure 4.24(a). The lines are computed as the vorticity barycenter of the corresponding vorticity distribution.

These figures emphasize the role of the vorticity distribution in the shears (Gerrard, 1966) and their separating distance D^* (Roshko, 1954b) in the selection of the global mode frequency. By inserting the control cylinder for a flow configuration IS , we observe that the vorticity in

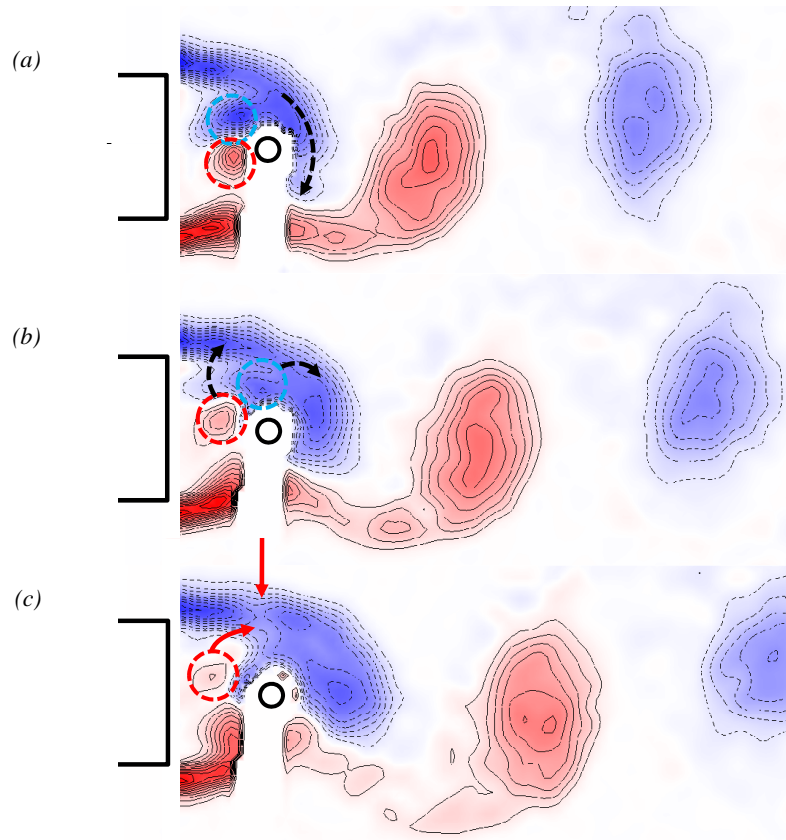


Figure 4.22: Three snapshots of one cycle of vortex shedding, showing the vorticity feedback effect of the control cylinder in the middle of the wake. The color map shows instantaneous vorticity ω_z of a phase-averaged flow.

4. WAKE WITH A CIRCULAR CONTROL CYLINDER

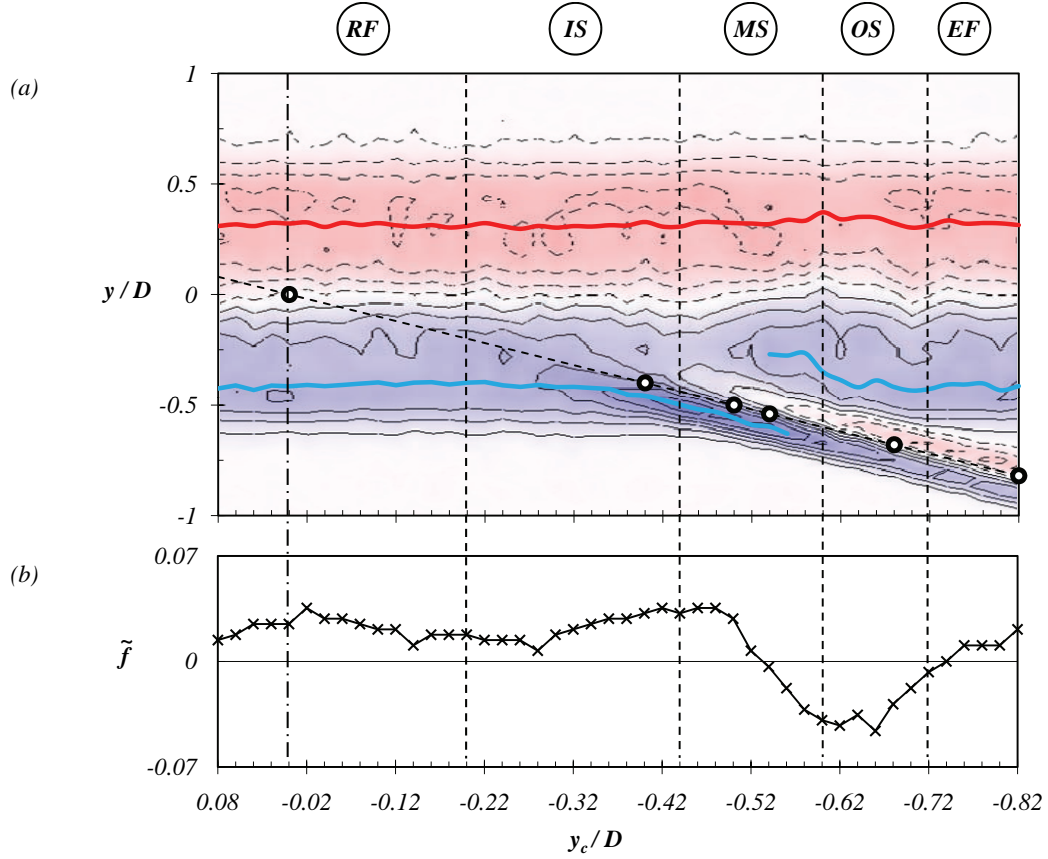


Figure 4.23: (a) Mean vorticity sequence $\bar{\omega}_z(y, x = 0.44D, y_c)$, for the 1mm control cylinder, showing the vertical vorticity distribution across the wake downstream of the control cylinder ($x_c/D = 0.4, y_c/D$). The contours of vorticity are the same as in figure 4.12(b). The dashed line denotes the path of the control cylinder across the wake, and circles represent the positions of the control cylinder presented in figure 4.12 and figure 4.14. Diagram (b) shows frequency \tilde{f} of the global mode. Notation *RF*, *IS*, *MS*, *OS* and *EF* refers to configurations defined in section 4.2.2.

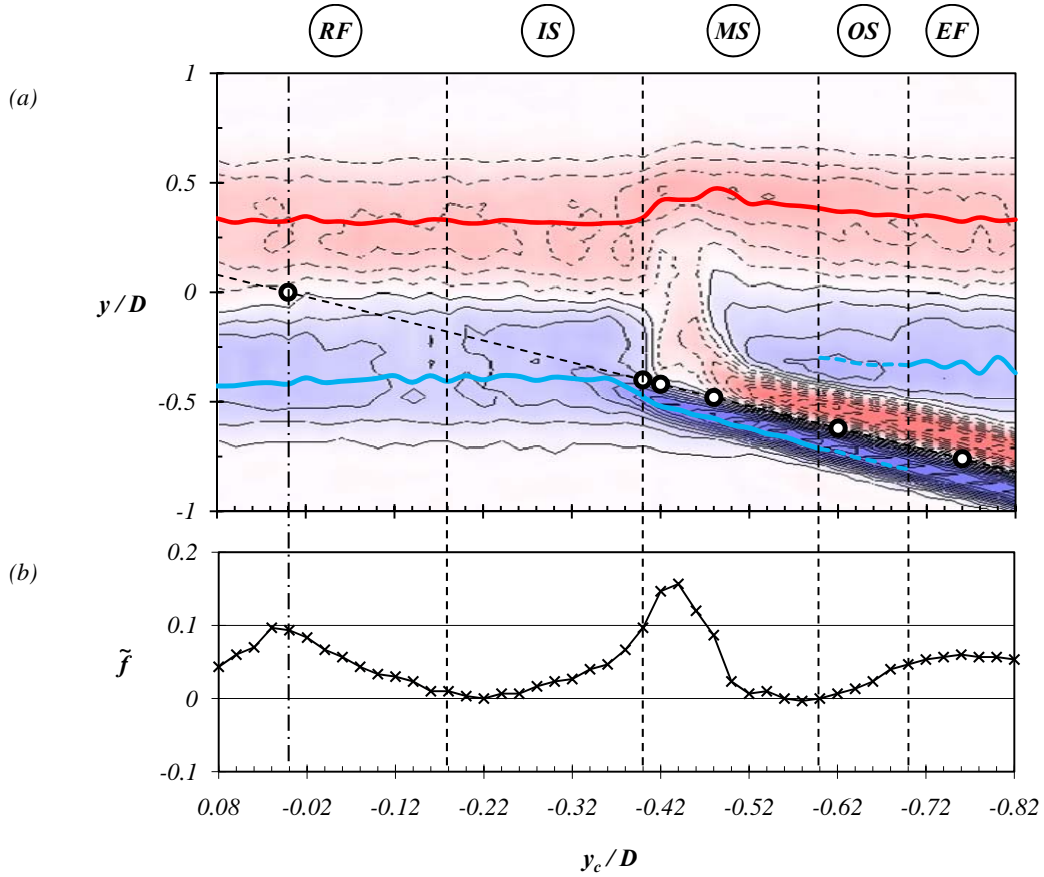


Figure 4.24: (a) Mean vorticity sequence $\bar{\omega}_z(y, x = 0.44D, y_c)$, for the 3mm control cylinder, showing the vertical vorticity distribution across the wake downstream of the control cylinder ($x_c/D = 0.4, y_c/D$). The contours of vorticity are the same as in figure 4.13(b). The dashed line denotes the path of the control cylinder across the wake, and circles represent the positions of the control cylinder presented in figure 4.13 and figure 4.15. Diagram (b) shows frequency \tilde{f} of the global mode. Notation RF , IS , MS , OS and EF refers to configurations defined in section 4.2.2.

4. WAKE WITH A CIRCULAR CONTROL CYLINDER

the affected shear is more concentrated and consequently, the shear is becoming thinner. This occurs as the cylinder progresses toward the *MS* pattern, for both control cylinder sizes. It is worth noticing that the separating distance of the shears (marked by the colored lines) remains unchanged. The thinning of the controlled shear means that the time needed for interaction of two shears to complete a vortex shedding is shorter (Gerrard, 1966), which is consistent with the corresponding frequency increase (figure 4.23-4.24) in the *IS* configurations. At some point the control cylinder starts to move the controlled shear linearly away from the center of the wake. As a result, the increase of the separating distance will counter effect the vorticity concentration. The balance between these two effects will lead to saturation and then to a decrease of the selected frequency as observed in flow configuration *MS*. In the case of the *3mm* control cylinder the separating distance is magnified by the presence of the jet (see section 4.2.2) that pushes away the uncontrolled shear (see figure 4.24a). In the *OS* configuration for the *1mm* control cylinder, the frequency is still very low because the vorticity in the controlled shear is weakened by the vorticity of opposite sign produced by the control cylinder. The mechanism of vorticity distribution is then again dominant as in *IS* configuration but in an inverse manner; vorticity is reduced and the shear becomes thicker. For configuration *EF*, the influence of the *1mm* control cylinder becomes negligible and frequency gradually increases, to obtain its natural value. In the case of the *3mm* cylinder, the frequency reaches a minimum when the separating distance is the largest at $y_c/D = -0.58$. However, the global vorticity dynamics in the *OS* configuration is confounded by the fact that there are four different layers of vorticity which are interacting. Because of this complex interaction, the *OS* region serves as a transition region between the frequency minimum in *MS* and the increased frequency in the *EF* configuration. It is then impossible to identify which shears are interacting. This is why the barycenter lines in the *OS* region are overlapping and are denoted by dashed lines. The size of the *3mm* control cylinder is sufficient to maintain a strong modification of the wake in *EF* configuration, which results in separating distance smaller than in the natural case, while vorticity remains unchanged. Hence, the frequency is higher than natural in the *EF* pattern.

4.4.2 Global mode structure and drag reduction

The spatial structure of the global mode should be extracted from the coherent part of the Reynolds stress that is synchronized at the global frequency. For cylinders, and in the near wake, the main contribution of the fluctuations to energy in the spectral domain is localized around the synchronized frequency of the global mode (see for example figure 3.7). Hence, our measurements of Reynolds stresses, displayed in figure 4.14 and figure 4.15 are also relevant to the structure of the global mode.

The main effect of the control cylinder is to displace downstream the extrema of the Reynolds shear stresses that are associated to the vortex shedding. This effect is accompanied by amplitude damping. It seems then natural to conclude that as for the Reynold stresses, the global mode structure is displaced downstream together with the strong damping. This has already

been observed in context of forced wake (Thiria *et al.*, 2006; Thiria & Wesfreid, 2007) near the threshold of instability at low Re . Similarly as in that study, we also find the maximum amplitude of the global mode to be roughly inversely proportional to its downstream position (figure 4.25). This behavior was also observed for natural wake (Couairon & Chomaz, 1999; Goujon-Durand *et al.*, 1994; Zielinska & Wesfreid, 1995) near the threshold of the instability around $Re = 50$. It is interesting to find the same feature at much higher Reynolds number.

The sensitivity of the global mode position to the control cylinder position may be interpreted with the Gerrard's model valid at large Reynolds number for the size of the formation region (Gerrard, 1966). Briefly, the formation region is bounded by the detached shears from the trailing edges and the eddies roll-up. From the physical Gerrard's model (see figure 1.7b), the size of the formation region results from an equilibrium of the entrainment of the detached shear layers (flux b) and replenishment of fluid into the recirculation region (flux c), while the circulation entrained by the vortex (flux a) is constant. Any changes in these fluxes due to the presence of the control cylinder will lead to a new equilibrium with a different size of the formation region. If the controlled shear gets more turbulent, then its entrainment will be increased which will reduce the formation region size. This occurs when the control cylinder sufficiently approaches the primary shear from outside the recirculation region. In this case, the control cylinder is in a high velocity region and has his own unsteady wake which enhances the turbulence in the primary shear. This situation is consistent with the $1mm$ control cylinder in the OS configuration, in which the vorticity in the controlled shear is partially canceled (figure 4.12b), the global mode structure shifted upstream (figure 4.14a-b) and the mean recirculation region length decreased. On the contrary, if the control cylinder concentrates the vorticity in the controlled shear, entrainment will be decreased and consequently the formation length increased. This effect is common for the IS configuration of the flow, for both $1mm$ and $3mm$ control cylinders (figure 4.12b and figure 4.13b) for which the global mode structure is shifted downstream (figure 4.14a-b and figure 4.15a-b) and the mean recirculation region length increased. A third mechanism that is responsible for the largest formation size increase, involves a direct injection of momentum in the formation region. This is clearly observable for the $3mm$ control cylinder in configuration MS (figure 4.13a), in which the global mode structure is the furthest from the main cylinder (figure 4.15a-b), and the mean recirculation region length the largest.

From our interpretation, the sensitivity of the global mode streamwise location is a direct consequence of the modification of the size of the formation region as described above due to the modification of the turbulent properties of the controlled shear.

The question that remains is about the relationship between the global mode position and global mode amplitude. Our idea is based on the role that the pressure gradients may play in the intensity of the eddies roll-up. In the previous sections of this chapter, we have shown that the base pressure is increased each time the global mode is pushed further downstream for both $1mm$ and $3mm$ control cylinders. If we assume that the formation region size is the key

4. WAKE WITH A CIRCULAR CONTROL CYLINDER

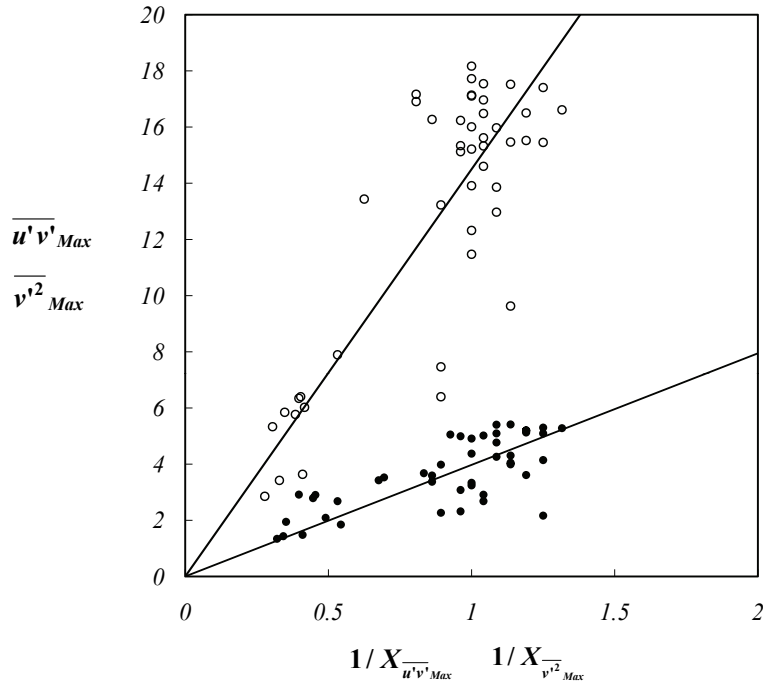


Figure 4.25: Amplitude of $\overline{v'^2}_{Max}$ (empty circles) and $\overline{u'v'}_{Max}$ (filled circles) versus the inverse of their respective locations for the $d = 3mm$ control cylinder at $x_c/D = 0.4$ and $0.08 > y_c/D > -0.82$. Straight lines are linear best fits.

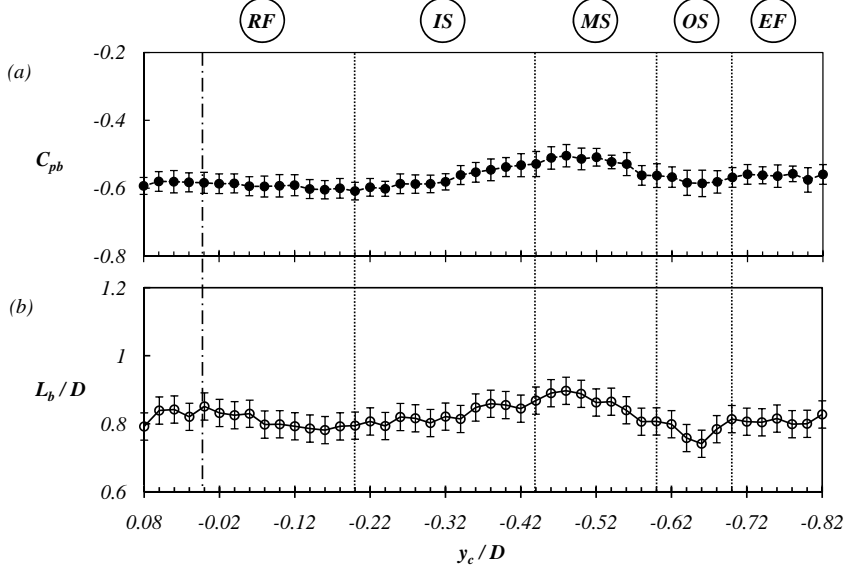


Figure 4.26: Base pressure coefficient C_{pb} (a) and recirculating bubble length L_b (b), for positions of the $1mm$ control cylinder ($x_c = 0.4D$, $-0.82D < y_c < 0.08D$). Notation RF , IS , MS , OS and EF refers to configurations defined in section 4.2.2. Error bars in (a) denote $C_{pb(rms)}$; in (b) error bars denote the uncertainty of L_b/D (see section 2.3.2).

parameter, its increase in length can create a base pressure increase (and then weaker pressure gradients), simply because a longer formation region will lead to less curvatures of the detached streamlines after the trailing edges. This is consistent with the strong correlation between the bubble length and the base pressure coefficient (see figure 4.26-4.27) and would explain the drag reduction mechanism. As a consequence, an increase of the formation region length leads the eddies to roll-up in a region of weaker pressure gradient which might explain the damping of the global mode each time it is displaced downstream.

As shown in figure 4.18(a) the $4mm$ control cylinder is also changing the recirculation bubble size when displaced along the horizontal axis of the wake. The recirculation bubble size closely follows the position of the control cylinder, because it stays attached to it, up until $x/D = 1.1$. Figure 4.28 shows that the base pressure is well correlated with the bubble length for this case also. For positions of the control cylinder $x/D > 1.1$ the bubble size starts to decline gradually. However, this "gradual reduction" is only an average of two very different bubble lengths. An increase in $C_{pb(rms)}$ in figure 4.28 for positions $x/D > 1.1$ betrays a presence of a bi-stable flow regime, which will be investigated in chapter 5. The argument that less curvature of the detached streamlines leads to higher base pressure is a feature of cavity models, based on steady potential flow theory with a closure model of the separated streamline (Wu, 1972). Whatever the closure model used, it is found that for a given bluff body the relationship between base pressure and bubble length exhibits a power law $L_b/D \propto (-C_{pb})^n$, with $n < 0$ depending on the

4. WAKE WITH A CIRCULAR CONTROL CYLINDER

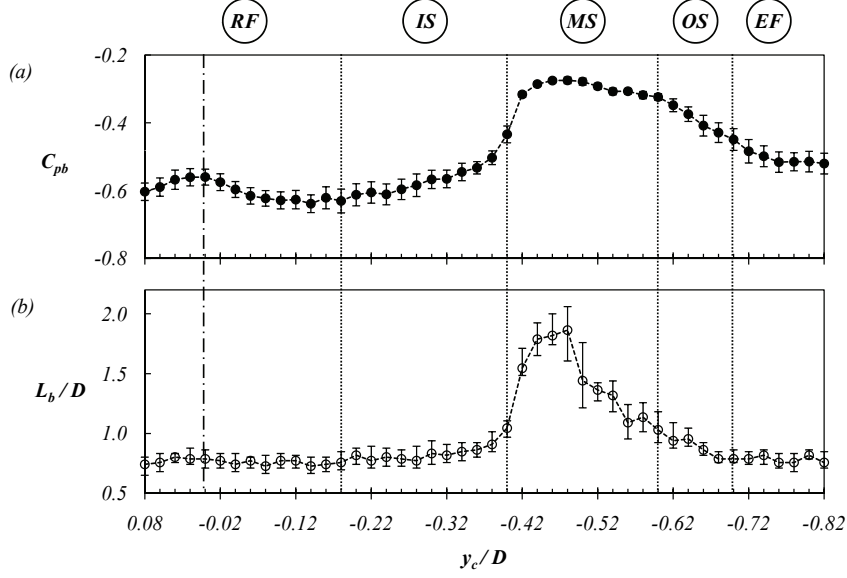


Figure 4.27: Base pressure coefficient C_{pb} (a) and recirculating bubble length L_b (b), for positions of the 3mm control cylinder ($x_c/D = 0.4$, $-0.82 < y_c/D < 0.08$). Notation *RF*, *IS*, *MS*, *OS* and *EF* refers to configurations defined in section 4.2.2. Error bars in (a) denote $C_{pb(rms)}$; in (b) error bars denote the uncertainty of L_b/D (see section 2.3.2).

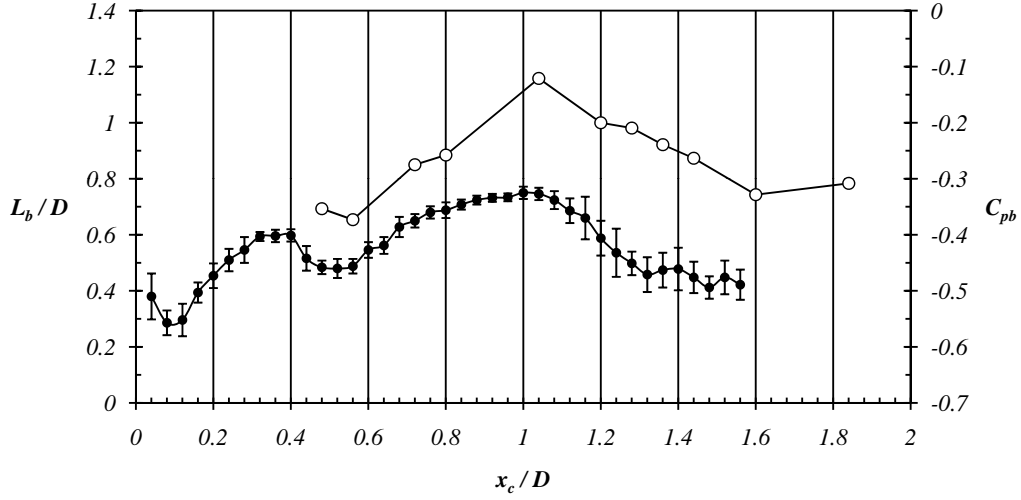


Figure 4.28: Base pressure C_{pb} (black points) and mean recirculation bubble length L_b/D (white points), for a $d = 4mm$ circular cylinder displaced along the horizontal axis of the wake $0 < x_c/D < 2$. Error bars denote the $C_{pb(rms)}$.

model (Franc & Michel, 2005). This relationship for the $3mm$ is deduced from the figure 4.27 and depicted in figure 4.29 with red circles. Two tendencies are found following that the control cylinder is inside the recirculation bubble ($y_c/D > -0.48$) or outside ($y_c/D < -0.48$). A similar tendency is also valid for the $1mm$ control cylinder which is shown in figure 4.29 with blue circles. This relationship is further confirmed with an experiment involving the artificial inflation of the recirculation bubble by base bleed. A jet of air from the base of the main cylinder is injecting momentum into the recirculation bubble, and consequently, the bubble length increases as well as the corresponding base pressure. The result is depicted by a yellow triangle in figure 4.29, and we can conclude that this relationship follows the same trend as when the control cylinder is inside the bubble. Details of this experiment can be found in appendix A. The bubble curvature is dependent on the length of the bubble as well as on its height, which is further discussed with regard to an experiment involving the trailing edge flap, the details of which can be seen in appendix B.

4. WAKE WITH A CIRCULAR CONTROL CYLINDER

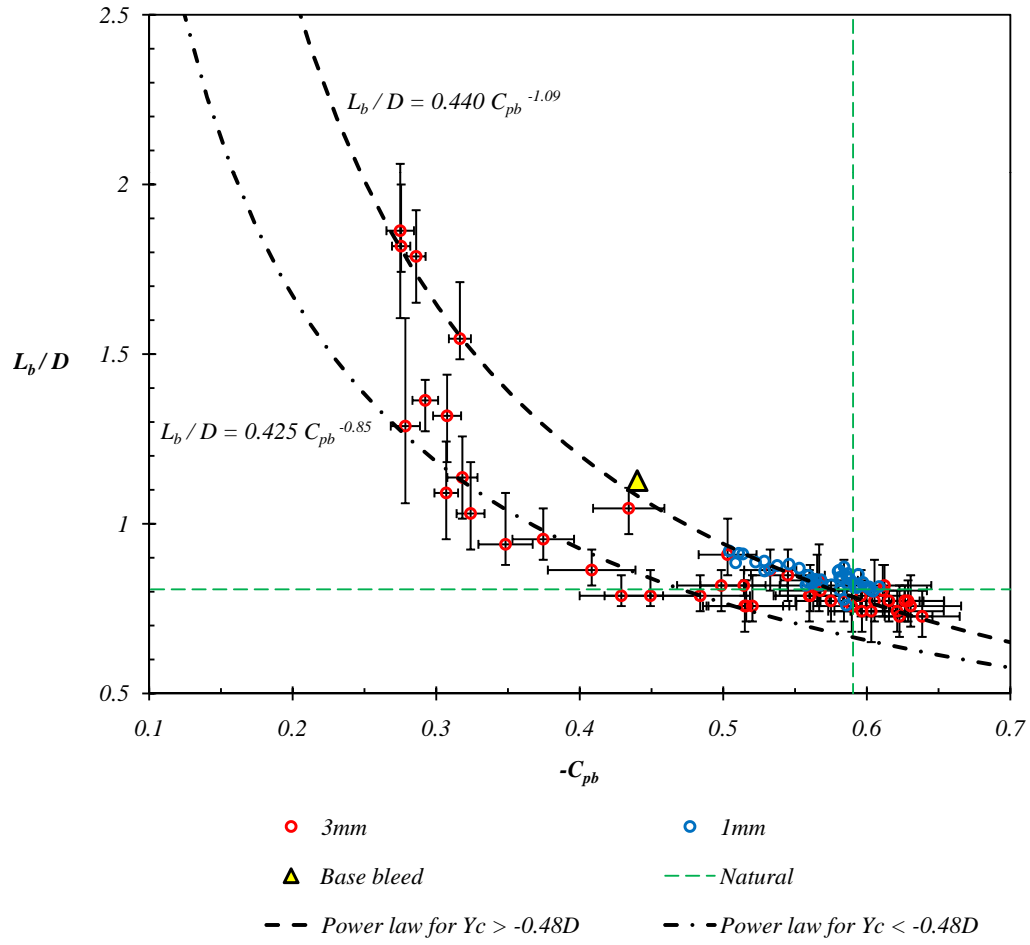


Figure 4.29: Base pressure coefficient C_{pb} as a function of the bubble recirculation length L_b for positions of the 1mm and 3mm control cylinder at $x_c/D = 0.4$, the natural case and for base bleed experiment.

4.4.3 Summary of the observed flow configurations

Figure 4.30 summarizes the variety of effects of the control cylinders on the global dynamics of the detached shear layers:

- In the reverse flow configuration the vorticity produced on the control cylinder travels upstream and affects the shear layer that is rolling-up; the vorticity of the same sign as in the shear is entrained into the roll-up vortex, while the vorticity of the opposite sign is canceling out with the incoming shear, making it weaker. The consequence is an easier vortex shedding and a higher global frequency. This effect is very weak for the $1mm$ control cylinder.
- In the inner shear configuration, the control cylinder feeds the controlled shear with same vorticity sign, making it thinner. Reduced entrainment demands, mean that the formation region will increase its size to regain a new equilibrium.
- In the middle shear configuration the controlled shear splits, the part of it that is deviated inside the formation region is canceled by the shear of opposite sign created by the $1mm$ control cylinder while it forms a jet in the case of the $3mm$ control cylinder. As the result the jet inflates the formation region.
- For the $1mm$ control cylinder, in the outer shear configuration, the shear of the control cylinder cancels partially the vorticity in the controlled shear, making it thicker and more turbulent. Increased entrainment demands, mean that the formation region will decrease its size to regain a new equilibrium. For the $3mm$ there is no vorticity cancellation, which leads to a complex interaction between the controlled shear and the two shears of the control cylinder.
- The external flow configuration shows no impact of the $1mm$ control cylinder, and the formation region is close to natural value, however, $3mm$ control cylinder is large enough to create a blockage effect that squeezes the formation region vertically.

4. WAKE WITH A CIRCULAR CONTROL CYLINDER

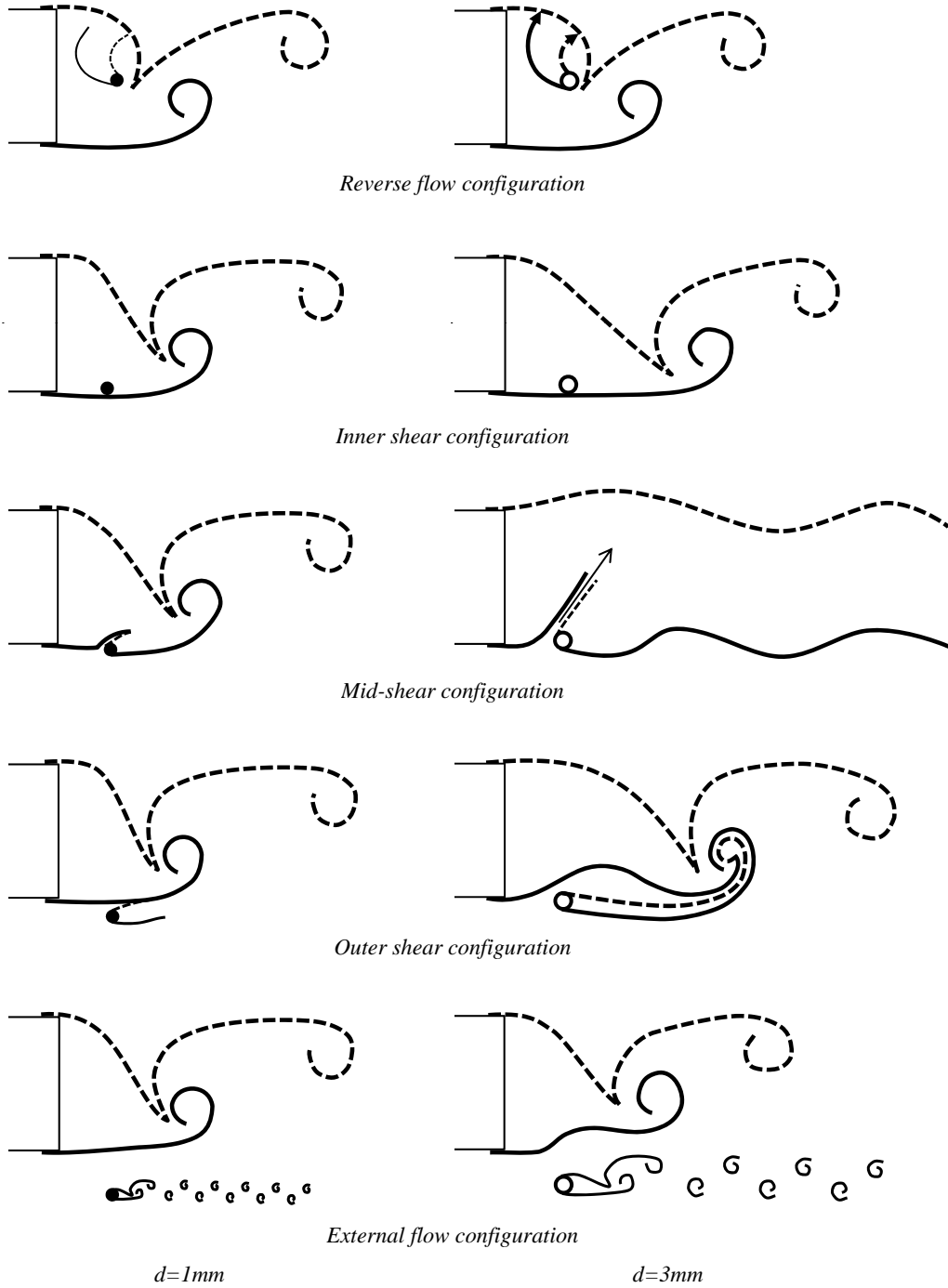


Figure 4.30: Schematic representation of characteristic wake flow patterns, observed and classified in this study.

Chapter 5

Bi-stable flow regime and 3D effects

5.1 Fluctuations of base pressure and lift

Pressure measurements have been used in previous chapters to observe and analyze the effects of the control cylinder on mean base pressure and mean drag. Because of all filtering effects of our measurement system, we cannot see the actual rate at which the pressure fluctuates. However, we can extract the *rms* of base pressure and lift measurements and see how it changes depending on the control cylinder's position.

The *1mm* map in figure 5.1(a) show only a trace of effect, which is not surprising since we have shown in the earlier chapters that there isn't much mean flow modification by that diameter of the control cylinder. If we look at the case of the *3mm* control cylinder, the mean flow modification is one of the main causes of change in the base pressure fluctuations, as can be deduced from the corresponding *3mm* map in figure 5.1(b). Both maps indicate a value of $C_{pb(rms)} \approx 0.03$ as the measurable natural fluctuation of the base pressure. In the *3mm* map, it is clear that the envelope of fluctuations is reduced in regions which correspond very well with regions of increased base pressure from figure 4.3(b). As we have shown in sections 4.2.3 and 4.1.2, whenever we increase the base pressure, it means that the vortex shedding is displaced downstream and away from the main cylinder. This displacement reduces the amplitude of the instability, and also the amplitude of fluctuations seen by the main cylinder, since the instability is pushed downstream. In any case, the pressure at the base of the main cylinder becomes more steady. However, there are regions of the *rms* map in figure 5.1(b) that show three to four times increase of the pressure fluctuations. These two regions are located around the downstream edges of the regions of reduced fluctuations, ie. on the edges of the regions where the length of the mean recirculation bubble is increased.

The lift fluctuations are less pronounced than base pressure fluctuations, which can be

5. BI-STABLE FLOW REGIME AND 3D EFFECTS

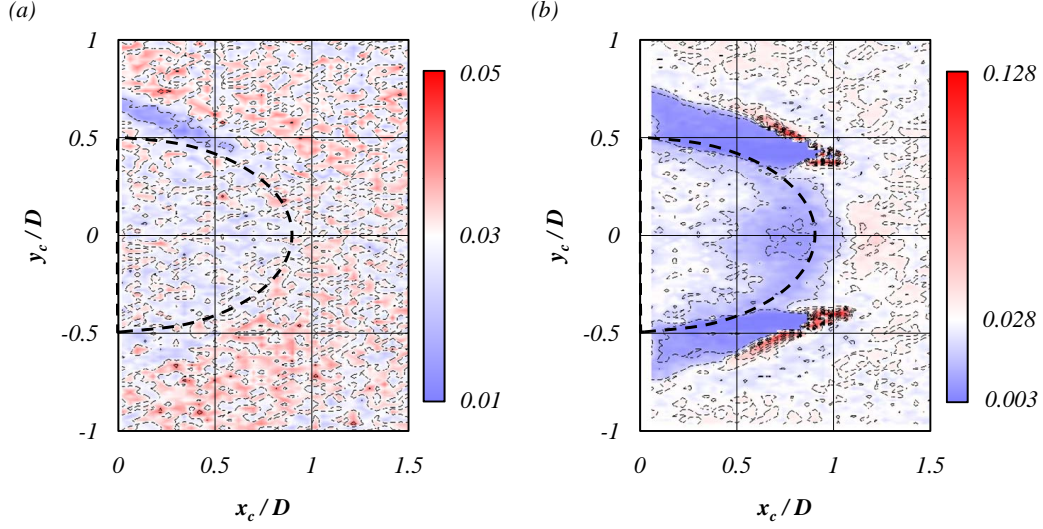


Figure 5.1: Sensitivity maps of base pressure $rms\ C_{pb(rms)}$ for (a) $d = 1mm$ and (b) $d = 3mm$ circular control cylinders. Isolines are in intervals of 0.01. Blue color designates a decrease and red an increase in base pressure fluctuations compared to that of the natural base pressure fluctuations, which is given in white. Dashed line depicts the shape of the recirculation bubble for the natural flow.

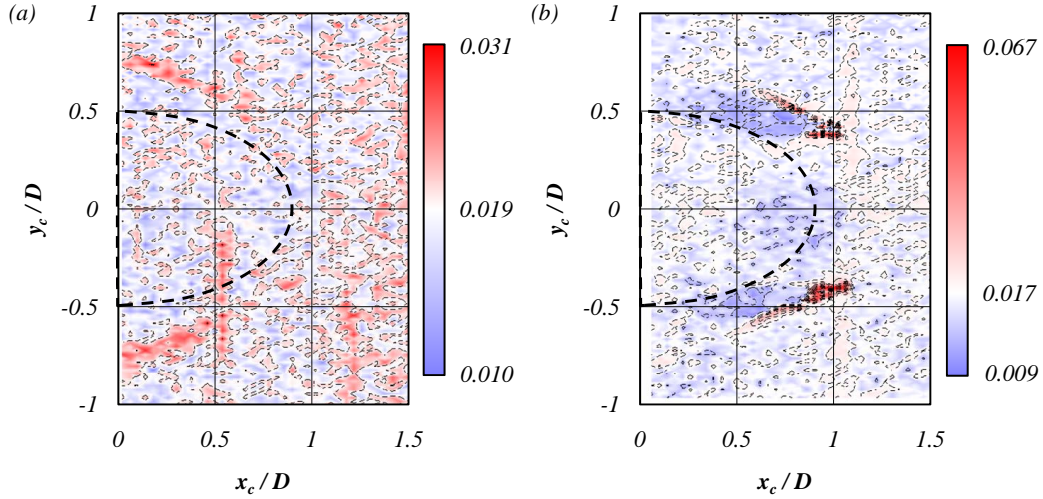


Figure 5.2: Sensitivity maps of lift coefficient $rms\ C_{l(rms)}$ for (a) $d = 1mm$ and (b) $d = 3mm$ circular control cylinders. Isolines are in intervals of 0.005. Blue color designates a decrease and red an increase in lift fluctuations compared to that of the natural lift fluctuations, which is given in white. Dashed line depicts the shape of the recirculation bubble for the natural flow.

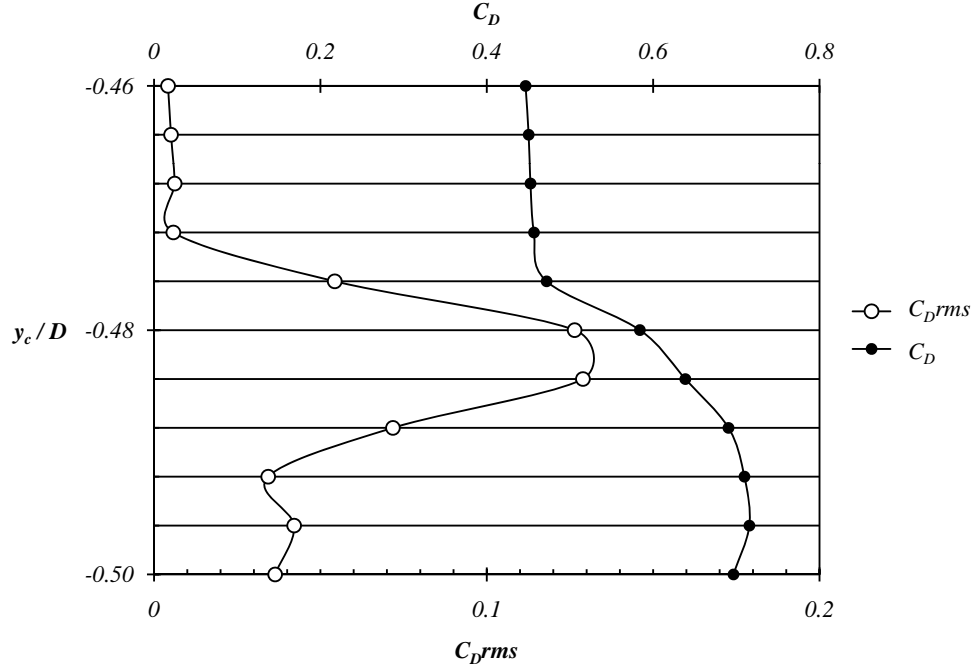


Figure 5.3: Mean drag coefficient (black circles) and drag *rms* (white circles) for ten positions of the $d = 3mm$ circular cylinder on a vertical line at $x_c/D = 0.74$ and $-0.46 < y_c/D < -0.5$.

confirmed from the maps in figure 5.2(a) for $d = 1mm$ and (b) for $d = 3mm$ circular control cylinders. The smaller cylinder has barely any distinguishable impact on lift fluctuations, while the larger shows a sensitivity structure similar to base pressure, but of globally lesser amplitudes. Suffice it to say that the lift fluctuations originate from the oscillation of the shear layers due to vortex shedding; when the global mode is damped, so are these oscillations and thus, the lift fluctuations are reduced. We do see an increase in lift fluctuations in exactly the same regions as for the base pressure, hence we assume that the origin of those is the same, and in further text we will discuss and explain this in terms of base pressure and drag only.

5.2 Bi-stable flow regime

In order to explore the phenomenon of high *rms* fluctuations of pressure, we have performed measurements for several positions of the control cylinder at a constant $x_c/D = 0.74$, which falls into the domain of high *rms* in the previously shown maps. Figure 5.3 shows the drag coefficient and drag coefficient *rms*, when the $3mm$ control cylinder is displaced from $y_c/D = -0.46$ to $y_c/D = -0.5$, in steps of $0.04D$. As said in chapter 4: drag is considered as an affine function of base pressure, therefore if we had shown the base pressure instead, it would change in the

5. BI-STABLE FLOW REGIME AND 3D EFFECTS

same manner. Here, drag is shown simply because those values were actually recorded during this particular experiment. That being said, we can observe that the fluctuations change very rapidly as the control cylinder changes position, from low fluctuation in the upper segment of the vertical range, through very high values, and finally the fluctuation settles to a value around natural in the bottom positions of the control cylinder. We can say that the high *rms* values for drag are in a region from $y_c/D = -0.476$ to $y_c/D = -0.488$. This means that, in absolute units, this region is only 0.3mm wide. In spite of this, the robustness, in terms of existence and size, of this high *rms* region is confirmed in several different experiments. Its exact vertical position, however, differs each time we attempt a measurement, but not by more than its size. When a follow up experiment was performed by recording long time series of pressure at $x_c/D = 0.742$, the maximum of *rms* was found this time to be at $y_c/D = -0.5$.

The diagram in figure 5.4 shows $C_p(s)$ distribution around the main cylinder for three characteristic positions of the control cylinder within this vertical line. The characteristic positions are chosen with regard to the *rms* value, and are at $(0.74, -0.48)$ for low *rms*, $(0.74, -0.5)$ for maximum of *rms* and $(0.74, -0.52)$ for the natural *rms* in the bottom part of the vertical line. The $C_{p(rms)}(s)$ for each pressure port is given in the error bars. The values of *rms* for the error bars have been scaled $\times 10$ in order to be visible and comparable between the three cases.

The first property we can observe is that, indeed, only the mean pressure and *rms* at the base of the main cylinder ($0.4 < s/L < 0.6$) are varying with different control cylinder positions. If we reference these positions to the map of the $C_{pb(rms)}$ for $d = 3\text{mm}$ shown in figure 5.1(b), we can confirm that the first position in figure 5.4(a) belongs to a region of reduced *rms*, as the error bars show a very small *rms*. Very large error bars for base pressure points in figure 5.4(b) tell us that the control cylinder is in the region of very high *rms*. Finally, figure 5.4(c) gives intermediate values of *rms* which is consistent with the natural state of the flow.

Now, in order to see what is happening in the flow, we have performed PIV measurements of the wake for the position of the control cylinder where we have obtained the maximum value of pressure fluctuations. This PIV recording is done with the standard setup and the acquisition parameters are referenced in chapter 2.

The PIV acquisitions in figure 5.5 two instantaneous velocity fields, for the same position of the control cylinder at $(0.78, -0.48)$. Figure 5.5(a) shows frame 435/500, where we can observe a huge region of low velocity, extending downstream for a length of more than $3D$. Figure 5.5(b) is showing frame 450/500 in which we can clearly see the Kármán Vortex Street, which is the governing global mode of the wake of the main cylinder. We can observe two pairs of vortices being advected downstream, from their origin in the roll-up zone, which appears to occur around $1D$ downstream of the trailing edge of the main cylinder. If we were to make mean velocity fields by choosing only instantaneous images from these two flow configurations, we would indeed obtain two mean velocity fields, which would considerably differ in the length of the mean recirculation bubble. In order to make mean flows of the two distinct states, we

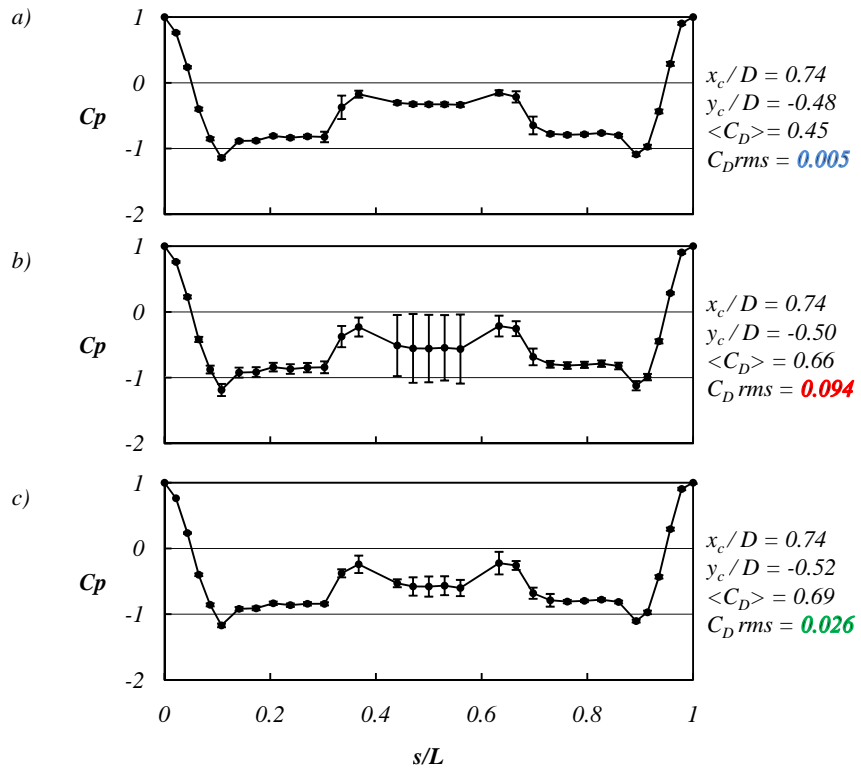


Figure 5.4: Pressure distributions ($\overline{C_p}(s)$) on the main cylinder for three characteristic positions around the regions of high base pressure fluctuations. Error bars denote $C_{pb(rms)}(s)$ scaled up by a factor of 10.

5. BI-STABLE FLOW REGIME AND 3D EFFECTS

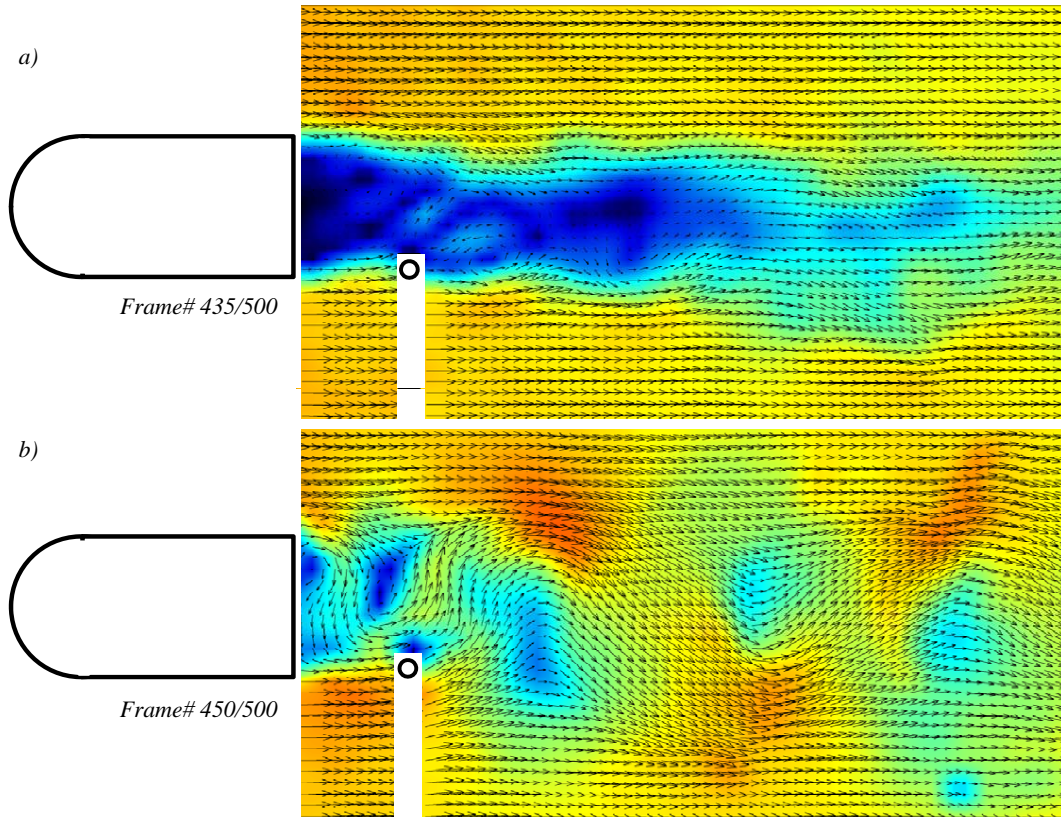


Figure 5.5: Instantaneous PIV velocity snapshots for $d = 3mm$ circular cylinder at $x_c/D = 0.78$, $y_c/D = -0.48$ showing two distinct configurations between which the flow oscillates in bi-stable mode.

have to be able to detect which state we see at each moment. For that purpose we extract the streamwise velocity $u(t)$, from the PIV image set, at $(1.7D, 0)$ in the wake. This point has been chosen as being in the region of low velocity when the recirculation bubble is big, and in the region of high velocity when the recirculation bubble is small. We will refer to these states as "high", for high speed, ie. small bubble, and "low", for low speed, ie. large bubble. Figure 5.6 shows the extracted velocity signal in green and a simple moving average of the signal over $\tau = 0.6s$ in red color. We have performed a simple moving average in order to facilitate the detection of flow state by setting the threshold of $u = 2m/s$. It is quite apparent from the raw velocity signal that the flow alternates between two states, with $\bar{u}_{low} \approx 1m/s$ and $\bar{u}_{high} \approx 4m/s$ as mean velocities at the referenced measurement point. Also, from figure 5.6, we can say that inside these 45 seconds of recorded flow the bubble changes its state six times; estimated roughly it can spend from 2 to 11 seconds in one of the states.

The 500 PIV images from this acquisition are divided into two groups based on the threshold criteria, and a mean streamwise velocity \bar{u} field is constructed from both groups of images. The two mean flows obtained are shown in figure 5.7(a) for the "high" state and in figure 5.7(b) for the "low" state. The lengths of the mean bubble L_b/D measured from these two mean flows are $L_{b(high)}/D = 2.9607$, for the "high" state and $L_{b(low)}/D = 1.62765$, for the "low" state. The base pressure *rms* for this position was recorded as $C_{pb(rms)} = 0.1264$. Also, we can recognize the typical *MS* flow configuration for the $d = 3mm$ circular cylinder, with the jet of fluid entering the recirculation bubble (see section 4.2).

The effect responsible for this bi-stable flow regime is the intermittent reattachment of the primary shear layer on the control cylinder. For positions with high *rms* of pressure, the shear layer is hesitating between being attached far downstream to the control cylinder, and rolling up immediately behind the main cylinder. This significant variation of the location of the formation region and the global instability is causing the recorded variations in the base pressure.

Out of the 500 fields in this set, we find 155 belonging to the "low" state and 345 to the "high" state. However, due to the small acquisition rate and duration of the PIV system, we cannot produce any well converged information on the time spent in each state. Therefore, we have performed additional measurements with a hot wire probe, placed at $x/D = 2$, $y/D = 0$, in order to measure more accurately how much time does the flow spend in each of the possible configurations. Ten positions of the control cylinder were explored with hot wire measurements, in range of $-0.48 > y_c/D > -0.52$, at a fixed $x_c/D = 0.742$. For each position hot wire probe measured the velocity signal during 4 hours, with the acquisition rate of $2000Hz$. The author would like to use this opportunity to specially thank Romain Monchaux for his work on the statistical treatment of the velocity signals in these experiments.

Figure 5.8 shows the velocity time series captured by the hot wire probe when the control cylinder is in position of high *rms*. We can see how the modulus of velocity in the xOy plane is varying between the two flow states. There is no determinable frequency of the shift between

5. BI-STABLE FLOW REGIME AND 3D EFFECTS

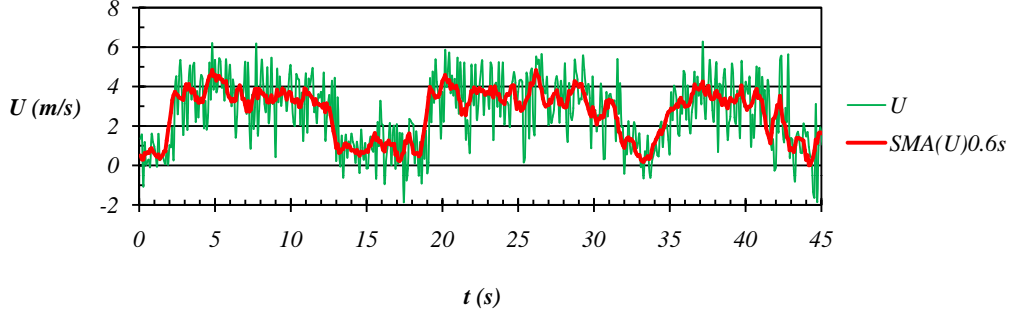


Figure 5.6: Time signal of streamwise velocity $u(t)$, obtained from PIV measurements, at $x/D = 1.7$, $y/D = 0$ (shown in green). The thick red line is a simple moving average $SMA(U(t))_{\tau=0.6s}$ of this signal performed over 0.6s.

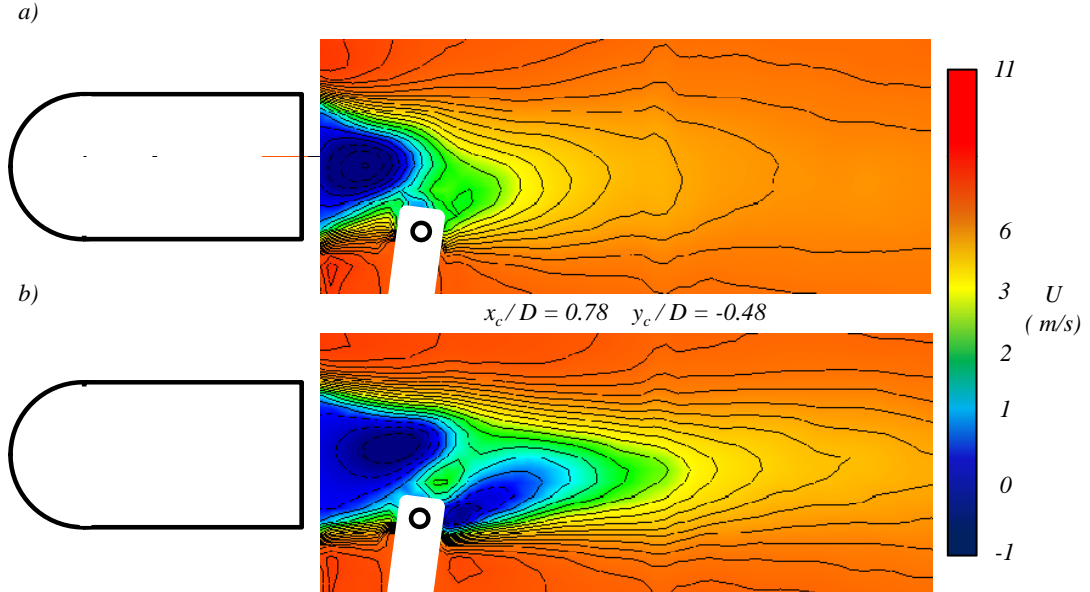


Figure 5.7: Mean streamwise velocity \bar{u} fields for the two states of the wake in the bi-stable mode: (a) "high" state of small bubble, and (b) "low" state of large bubble.

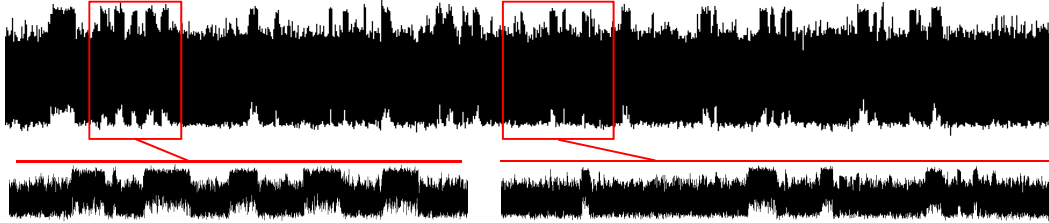


Figure 5.8: Time series of 2 minutes of the modulus of velocity in xOy , from the hot wire probe acquisition with the two flow regimes visible. The two zoomed-in details of the signal illustrate how there is no observable pattern; ie. the bi-stability is a stochastic process.

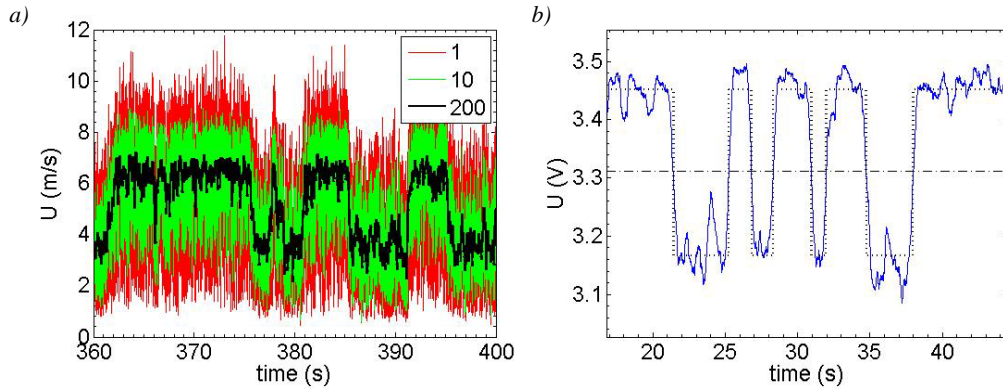


Figure 5.9: Time series of the modulus of velocity in xOy , from the hot wire probe acquisition of 2 minutes, with two flow regimes visible. The two zoomed-in details of the signal illustrate how there is no observable pattern; ie. the bi-stability is a stochastic process.

5. BI-STABLE FLOW REGIME AND 3D EFFECTS

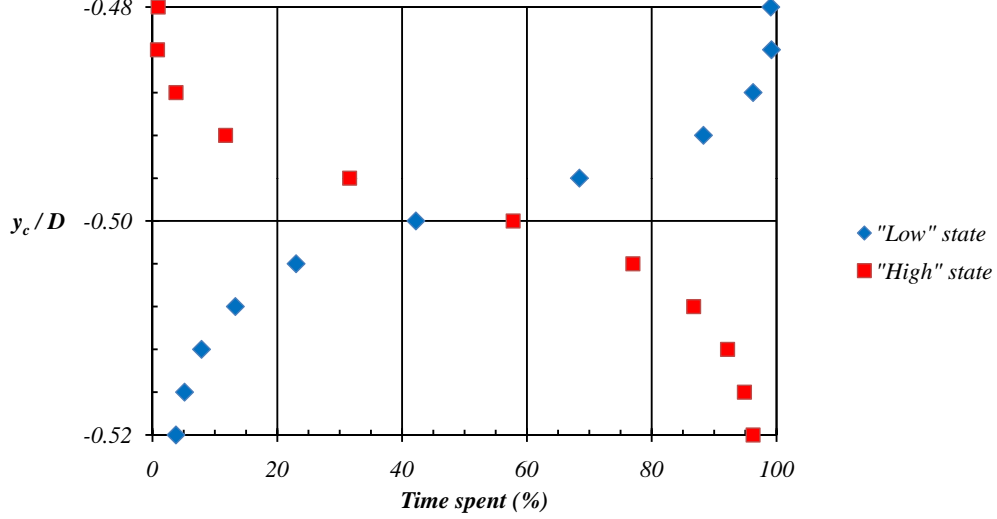


Figure 5.10: Time spent in "low" (red) and "high" (blue) states, based on the hot wire probe signal of 4 hours duration for each position of the control cylinder in range of $-0.48 > y_c/D > -0.52$.

states, and also no constant time duration of either of the two states. We can conclude that the process is stochastic and that the selection of a state is randomly by the turbulent nature of the wake. A property we can measure is how much time does the flow spend in each configuration.

A moving average was performed on the velocity time series as shown in figure 5.9(a). We have selected the moving average on 200 points as the basis for state detection, as it is obviously much smoother. Next, a rough threshold is defined at $5m/s$ and the signal is split between the parts below and above this threshold. Averages of both parts are computed and a mean between the two averages is taken as a definitive threshold between the two states. It is found that the threshold is changing by no more than 10% between the different positions of the control cylinder. The data is then binarized around the established threshold (figure 5.9b), and the length of each sequence is calculated, and summed for each of the two corresponding states. The statistics are plotted in figure 5.10, as percentage of time in each state as a function of the position of the control cylinder. We can conclude that the flow spends almost an equal amount of time in each state at the position of the maximum recorded rms . As the control cylinder is moved towards the wake horizontal axis, the time spent in "low" state (ie. when the bubble is large) increases, which means that it gets easier for the shear layer to re-attach to the control cylinder. When the control cylinder moves downwards, away from the middle of the wake, the flow spends more and more time in "high" state, meaning that the flow is mostly detached.

From the base pressure rms sensitivity map of the $3mm$ circular cylinder in figure 5.1(b), we can notice another small region of increased rms values, which is found on the horizontal axis of the wake, at $(1.1D, 0)$ to $(1.4D, 0)$ downstream of the main cylinder. One of these high

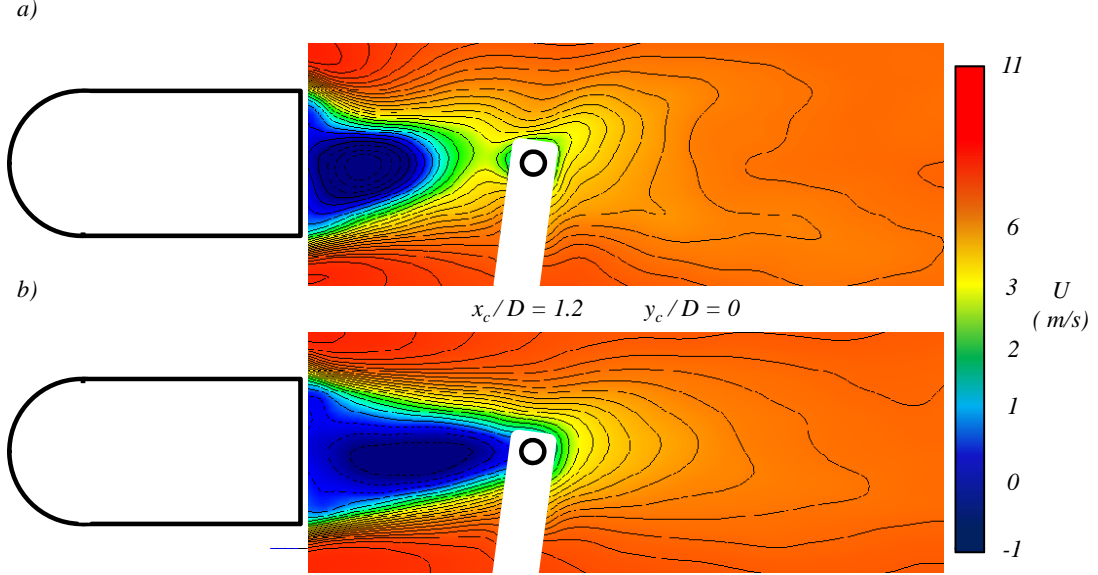


Figure 5.11: Mean streamwise velocity \bar{u} fields for the two states of the wake in the bi-stable mode: (a) "high" state of small bubble, and (b) "low" state of large bubble.

rms positions, at $(1.2D, 0)$ has been mentioned in chapter 4.3. We have shown mean flows for this position in figure 4.18 and figure 4.19, which were built from flows in both states with a resulting value of the bubble size which was somewhere between the values for each state. The separate mean flows for each state are shown in figure 5.11, and we can measure a mean bubble lengths of $L_{b(low)}/D = 1.28$, for the "low" state and $L_{b(high)}/D = 0.73$, for the "high" state.

In conclusion, we can say that the modification of the wake by the control cylinder can lead to damping of the fluctuating aerodynamic forces on the main cylinder, except in a few localized regions, where the control cylinder provokes huge increase in fluctuations. These fluctuations are caused by intermittent re-attachment of the flow to the control cylinder. Since these regions are sufficiently far downstream, the differences in recirculation bubble between the two different states are very large, and so, the pressure at the base fluctuates between two very different values, which is observable in the base pressure *rms*. At the focal point of these high *rms* regions, the flow spends almost equal amounts of time in each of the two possible states, however, there is no pattern observable for choosing one state or the other, and we can conclude that the process is stochastic.

5.3 Hysteresis of shear layer re-attachment

A phenomenon of hysteresis of the shear layer re-attachment was noticed in several of the mapping experiments of $1mm$ circular cylinder. Figure 5.12 shows raw frequency data obtained from one such experiment. The color map is in a usual range of values for a frequency map, but here it is in Hz , not given as a Strouhal number, with white being the natural frequency for this experiment. The axes depict indexed position of the control cylinder. We can see that the step in horizontal sense in two times larger than the step in the vertical direction, which is usual in most of our mapping experiments. The black dashed lines depict the movement of the control cylinder, with the arrows pointing out the direction for each sequence.

We can notice an increase in frequency when the control cylinder reaches position $x_c = 3$, $y_c = 30$, while for other positions around it frequency is decreased. This transient appears again at $x_c = 5$, $y_c = 28$, and similarly for a few more positions which can be easily seen on the map. This occurs each time the control cylinder is moved downwards across the sensitive area, but not when it is moved upwards. This brings us to a conclusion that we are witnessing a hysteretic behavior of the re-attachment of the shear layer to the control cylinder. This behavior is not visible in the lower part of the map (not shown here).

The specific conditions of the upper shear in this experiment in conjunction with the size of the control cylinder which, being $1mm$, is just enough to cause attachment, have caused the shear layer intermittently attaching depending on the direction from where the control cylinder is approaching it. When it approaches from above and outside of the recirculation region, we observe a usual frequency reduction as in the position OS for the $1mm$ control cylinder, then the cylinder passes through the MS configuration and the natural frequency, finally entering IS , with re-attachment and frequency increase. However, if the control cylinder is moved further down, the effects of IS abruptly stop, since the shear is no longer attached. An example of this entire sequence are positions at $x_c = 5$, from $y_c = 45$ to $y_c = 25$. On the contrary, if the control cylinder approaches the shear layer from below, the IS effect is missing; the shear doesn't attach to the control cylinder and there is no vorticity production which would increase the frequency. The cylinder moves directly into MS and then into OS configuration of frequency decrease. See positions $x_c = 4$, from $y_c = 25$ to $y_c = 35$ as a good example.

5.4 Spatial correlations of hot-wires local measurements

Similarly to the frequency sensitivity maps presented in the previous sections, we will show how the correlation coefficient computed from Eq. 2.1 changes when the control cylinder is inserted into the wake. Figure 5.13 shows the three horizontal and one vertical correlation coefficient for the $1mm$ control cylinder. Figure 5.14 shows the same for the $3mm$ control cylinder. As a consequence of the experimental symmetry, the sensitivity maps of $r_{[0-1]}$ and $r_{[1-2]}$, both computed on a distance of $2D$, display the same structure and intensity. This is evidenced in the scatter plot of figure 5.15, by the linear relationship of slope 1 between $r_{[0-1]}$ and $r_{[1-2]}$.

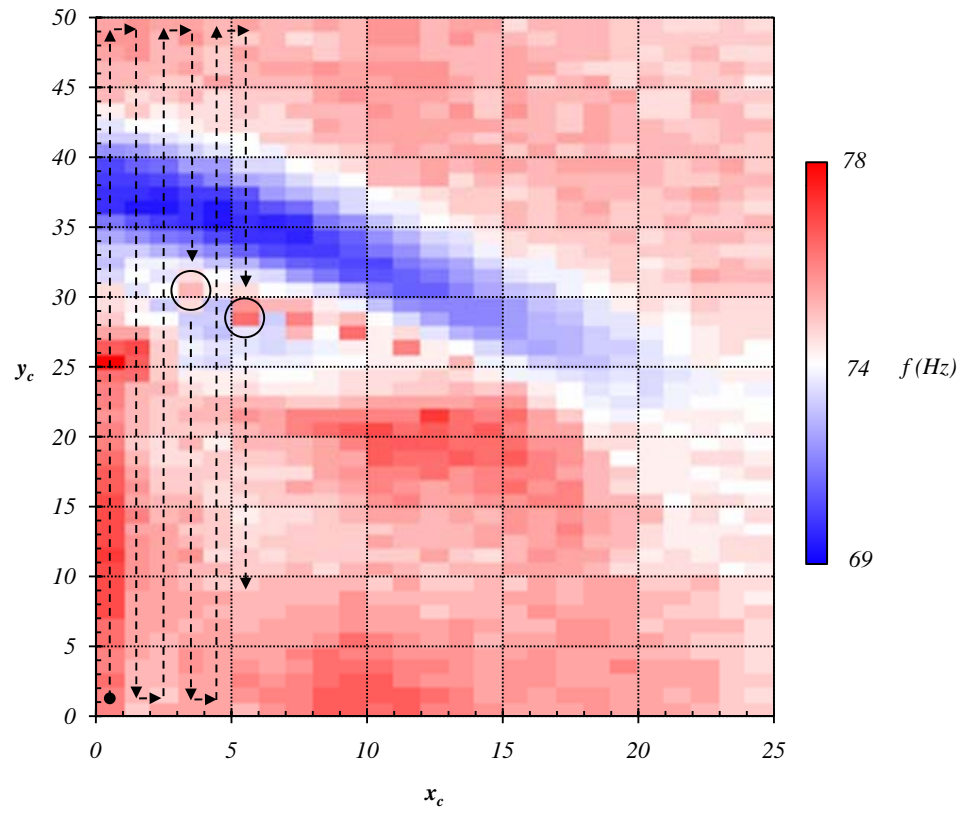


Figure 5.12: Sensitivity map of the Strouhal number for 1mm circular control cylinder, showing hysteresis of the detached shear layer re-attachment, as intermittent St changes. Dashed lines represent the movement of the control cylinder during the mapping experiment.

5. BI-STABLE FLOW REGIME AND 3D EFFECTS

The sensitivity map of $r_{[0-2]}$, which is computed on a distance of $4D$, is identical to the others in structure, but its intensity is reduced by a factor of 2 because of their linear relationships of slope 1/2 (see figure 5.15). These observations are identical for both control cylinders.

The spanwise correlation can then be described from only one correlation coefficient that will be chosen as $r_{[0-1]}$, and is shown in figure 5.13, for the $1mm$ control cylinder. In this case, correlation coefficient changes are in the range of $0 < r < +0.39$, and we can conclude that the presence of the control cylinder can significantly improve the correlation as well as it can reduce it (see chapter 3 for natural values). The correlation is improved when the control cylinder is inside the recirculation bubble, or on its boundary. When the control cylinder is outside, either above or below the wake, the correlation is reduced.

The effects of the $3mm$ control cylinder on the correlation coefficient $r_{[0-1]}$ can be seen in figure 5.14. The changes are in the range of $-0.034 < r < +0.626$. As for the $1mm$ control cylinder, the correlation is always increased when the control cylinder is inside the bubble. The main difference is observed at boundary of the mean recirculation bubble, where there are two regions of strong reduction of correlation. The reduction sometimes reaches negative values in the upper region. These regions are spatially very similar to regions of increased base pressure coefficient, and a comparison between them for the $1mm$ and two different experiments of the $3mm$ control cylinder are shown in figure 5.16.

For both sizes of the control cylinder, the sensitivity maps of r show some sort of symmetry with respect to Ox axis. We remind the reader that due to position of the velocity measurements (see section 2.2), that is not on the horizontal axis of the experiment, there is no symmetry that imposes identical measurements for two symmetric positions $\pm y_c$ of the control cylinder. Then the pseudo-symmetry in figures 5.13 and 5.14 indicates, that even if the measurement of the correlation is local, it remains influenced by the global properties of the wake.

5.5 Effects on the 3D properties of the wake

The three dimensional properties of the wake have been investigated with spanwise spatial correlation. The spatial correlation is increased for all the positions of the control cylinder inside the recirculating region comprising RF and IS configurations. It is decreased when the control cylinder is in the OS and EF configurations. In the case of the MS configuration, it depends on the size of the control cylinder, the correlation is increased for the $1mm$ control and decreased for the $3mm$ control. At large Reynolds number, $Re > 5000$, the 3D structure of the wake of a cylinder is dominated by random-positioned vortex dislocations (Norberg, 2001) causing a strong decrease in the lift fluctuations and contribute to the width of the peak at the Strouhal frequency (Prasad & Williamson, 1997). It is known that these effects are correlated to the laminar to turbulent transition in the shear layers (Bloor, 1964; Norberg, 2001). For the $3mm$ control, the clear modulation in the RF and also in IS configurations along the span indicates periodic dislocations appearances in the wake. This organization can be ascribed

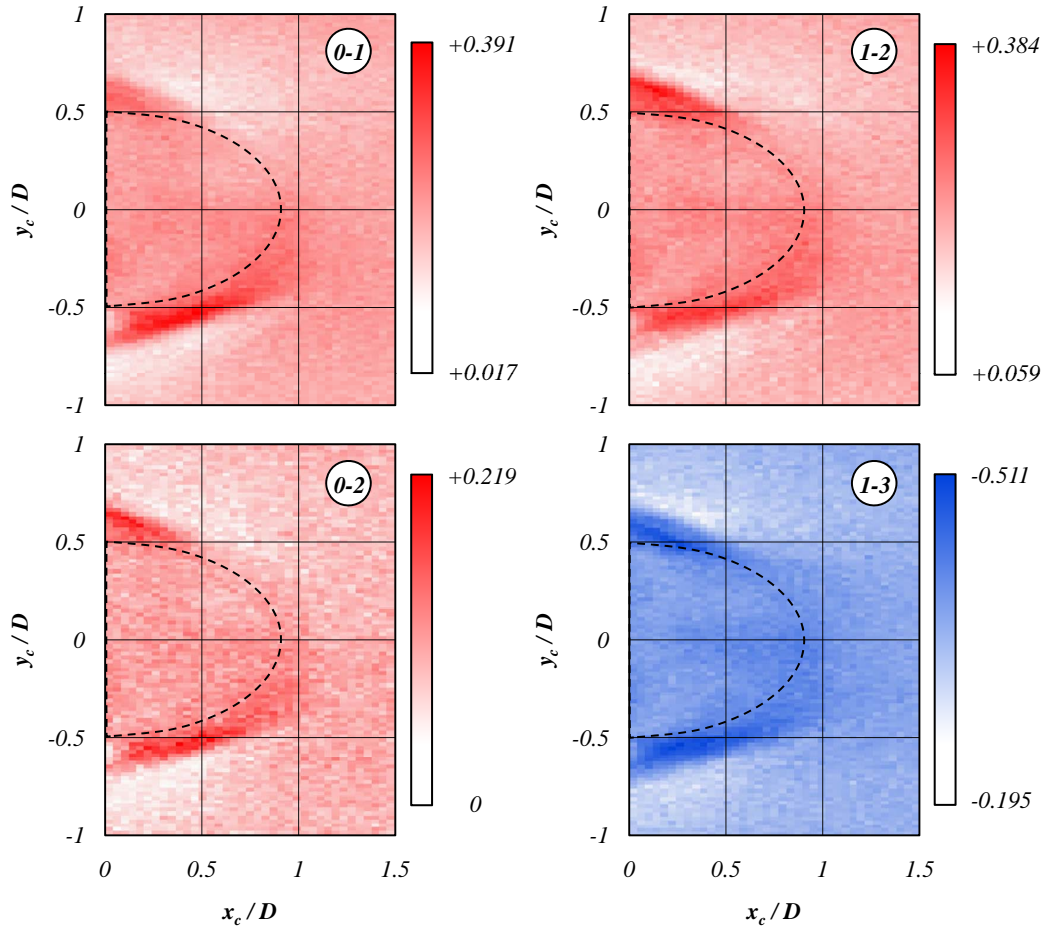


Figure 5.13: Sensitivity maps of the spatial correlation coefficient $r(x_c, y_c)$ for $d = 1mm$ control cylinder. In the top right corner of each map is indicated which hot wire probes are used to build the corresponding correlation coefficient. Dashed line depicts the shape and size of the mean recirculation bubble for the natural flow.

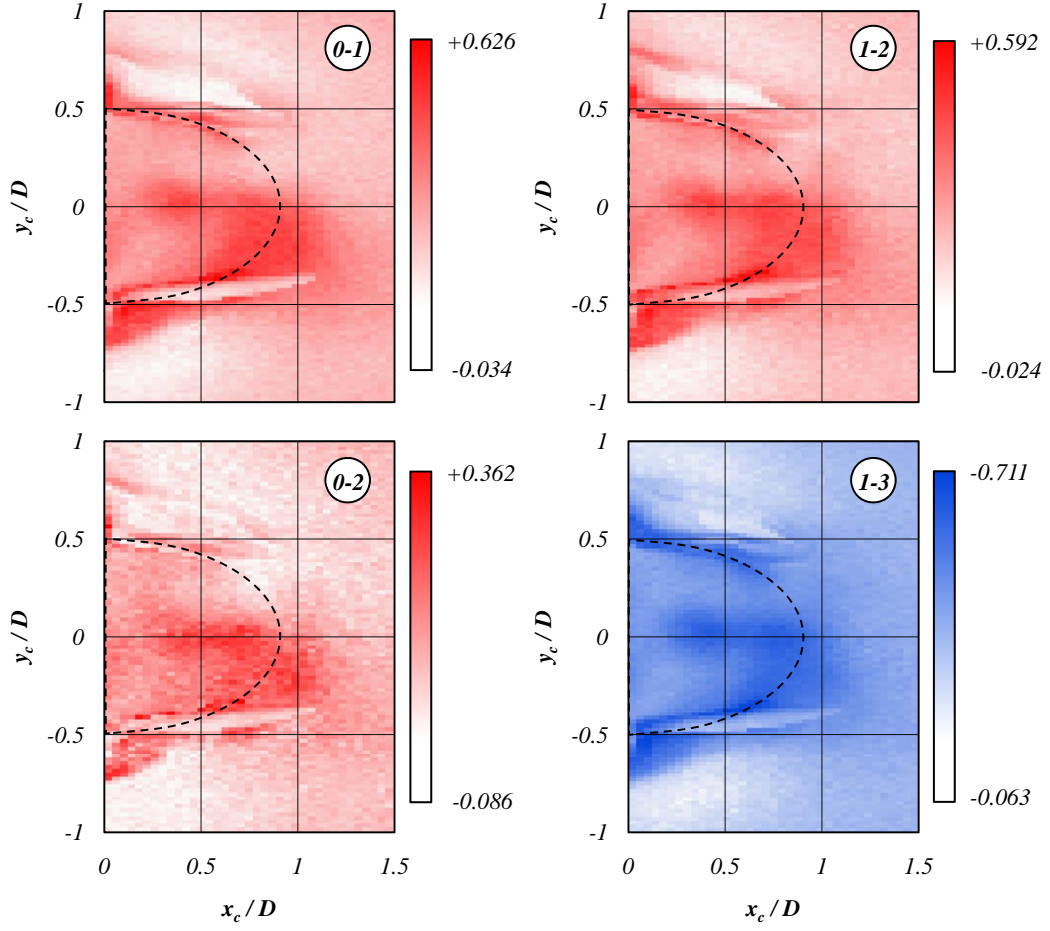


Figure 5.14: Sensitivity maps of the spatial correlation coefficient $r(x_c, y_c)$ for $d = 3mm$ control cylinder. In the top right corner of each map is indicated which hot wire probes are used to build the corresponding correlation coefficient. Dashed line depicts the shape and size of the mean recirculation bubble for the natural flow.

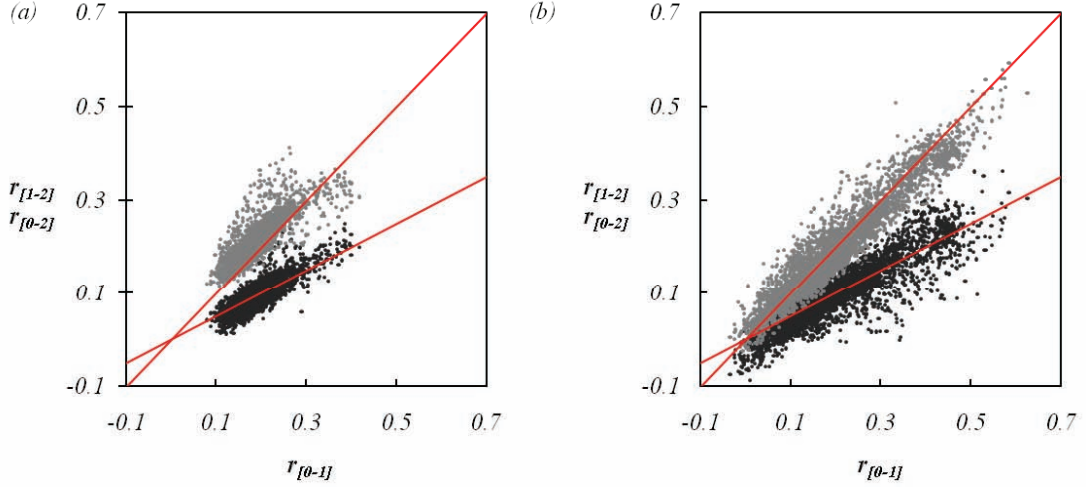


Figure 5.15: Scatter plot of correlation coefficients $r_{[0-1]}$ vs. $r_{[1-2]}$ (light points), and $r_{[0-1]}$ vs. $r_{[0-2]}$ (dark points), for (a) 1mm and (b) 3mm control cylinder. Lines correspond to linear relationship slope of 1 and 1/2.

to an improvement of the feedback effect involved in the global mode synchronization and may contribute to the spanwise correlation increase. In addition, for *IS* configuration, the vorticity concentration in the controlled shear can be viewed as a relaminarization of the shear whose consequence will be to improve the spanwise correlation. Similarly, for the *OS* and *EF* configurations, the controlled shear is weaker and forced by the Kármán vortex street of the control cylinder, which can be viewed as a turbulence enhancement in the shear and thus, a reduction of the spanwise correlation.

In the interest of characterization of 3D effects, we have performed smoke visualization of the flow in xOy plane, for some positions that correspond to configurations *RF*, *IS* and *OS*. Figure 5.17(a) shows the flow configuration *RF*, with a corresponding velocity spectrum in (b). The spectrum has two clear peaks around the shedding frequency. The visualization of the wake reveals parallel vortex tubes (c) and oblique shedding (d) with the appearance of dislocations, thus creating a difference in the frequency of shedding between the two far edges of the main cylinder. In the work of Maekawa & Abe (2002) we can see examples of periodic dislocations and the corresponding multiple energy peaks in the spectral analysis of the velocity. The difference in shedding frequency between the two edges of the main cylinder span correspond to the difference in frequency between the two peaks in the spectrum shown above. Figure 5.18 gives the same information but for a typical *IS* flow configuration shown in (a); the shear layer is attached and the bubble has grown, and the spectrum (b) shows a single wide peak. The images in (c) and (d) both show a large bubble, while the left side

5. BI-STABLE FLOW REGIME AND 3D EFFECTS

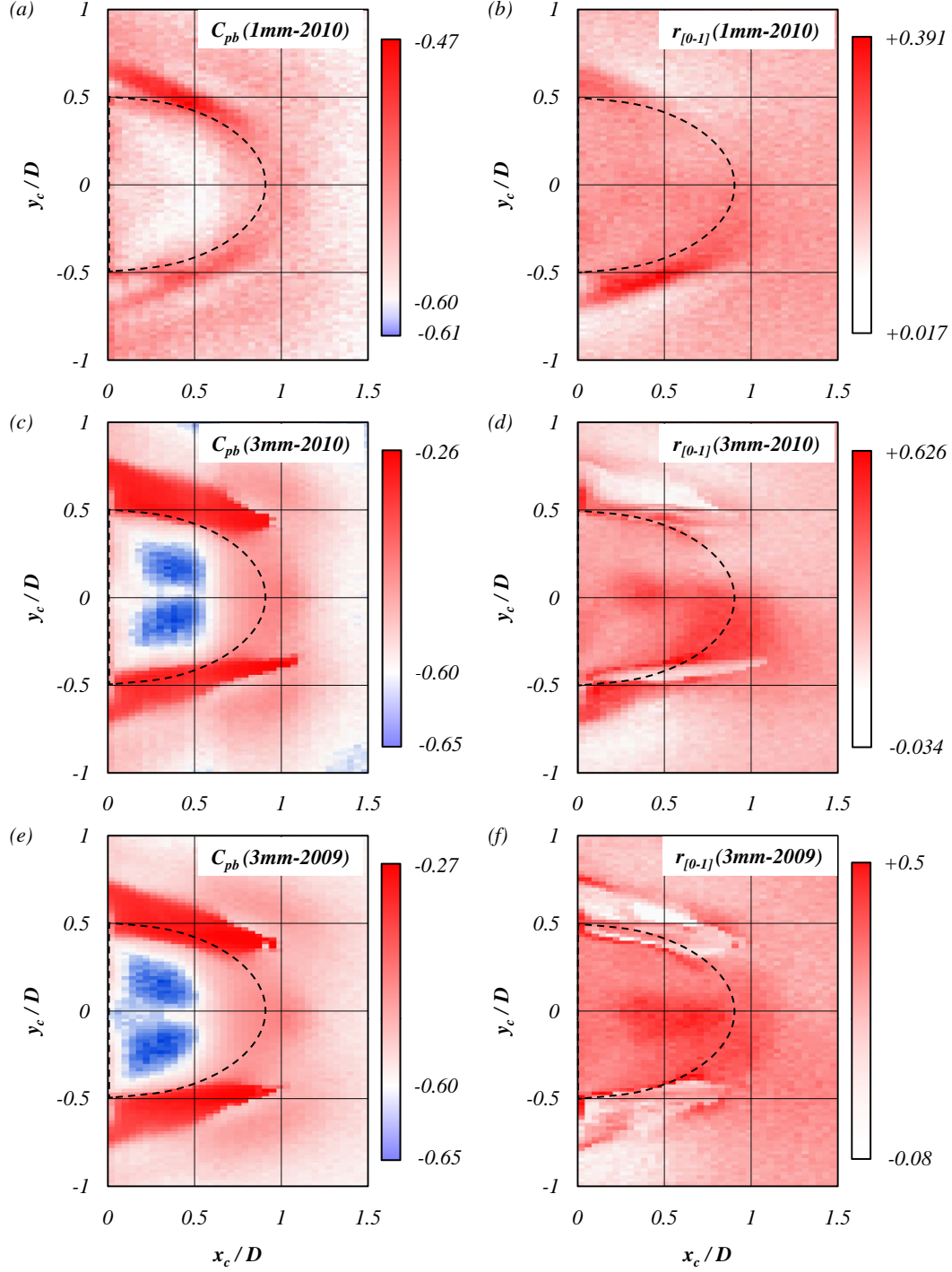


Figure 5.16: Comparison of sensitivity maps of base pressure (left column) and spanwise correlation coefficient (right column). The results are obtained for 1mm (a,b) and two experiments of the 3mm circular control cylinder (c,d,e,f).

of the wake shows oblique shedding and a central dislocation. Due to shear layer and control cylinder interaction and the bubble growth, this wake is much more chaotic than the one shown in figure 5.17. Figure 5.19(a) shows a position between the *MS* and *OS* configurations. We can observe in figure 5.19(b) a very noisy spectrum with no distinguishable energy peak. The visualization in figure 5.19(c) reveals a very large bubble and very irregular vortex tubes behind it. In figure 5.19(d) we can see that a smaller bubble also appears in this flow, with vortex shedding behind still very irregular.

We can also observe some consequences of 3D effects with high-speed PIV in the xOz plane in figure 5.20 for the *IS*, and in figure 5.21 for the *OS* configuration. We have extracted the vertical velocity $v(t)$ at $x/D = 2$ and $y/D = 0$ from the 500 frames of instantaneous PIV velocity fields. Figure 5.20(a) shows a modulated amplitude of the vertical velocity, and the corresponding frames in (b) show the bubble slightly longer around frame number 250. This could be due to a dislocation which appears around $t = 250$ and the vortex shedding mechanism "misses" one cycle, but adapts by momentarily delaying the roll-up. We can observe that the shear layer is always attached to the control cylinder, as is usual for the *IS* configuration, and therefore a 3D event is probably responsible for this sudden modification. Figure 5.21(a) shows a bigger impact on the amplitude of the velocity signal, and the corresponding frames in (b) reveal a bubble, which is longer from $t = 0$ to $t = 200$, and then is followed by a shorter bubble throughout the second half of the measurement. This is very similar to two states shown earlier in figure 5.19. Again, a probable scenario is a 3D effect which can locally (in spanwise sense) modify the bubble size.

However, it needs to be emphasized here that both the visualization experiments and the high-speed PIV give little in the way of statistical information as they are measured over very short time scales. The 500 frames of high-speed PIV shown above show only $1/6$ of a second of flow, given the acquisition rate of $3000Hz$. Therefore, these are only observations and illustrations of the events we have been able to witness in the wake. Still, they are very helpful in obtaining a better picture of the complexity of 3D structures and their influence in our study of a turbulent wake behind a 2D cylinder. Experiments with end-plates added to the main cylinder have also been performed, in an attempt to reduce the 3D instabilities in the wake. Details of these experiments are given in appendix C.

5. BI-STABLE FLOW REGIME AND 3D EFFECTS

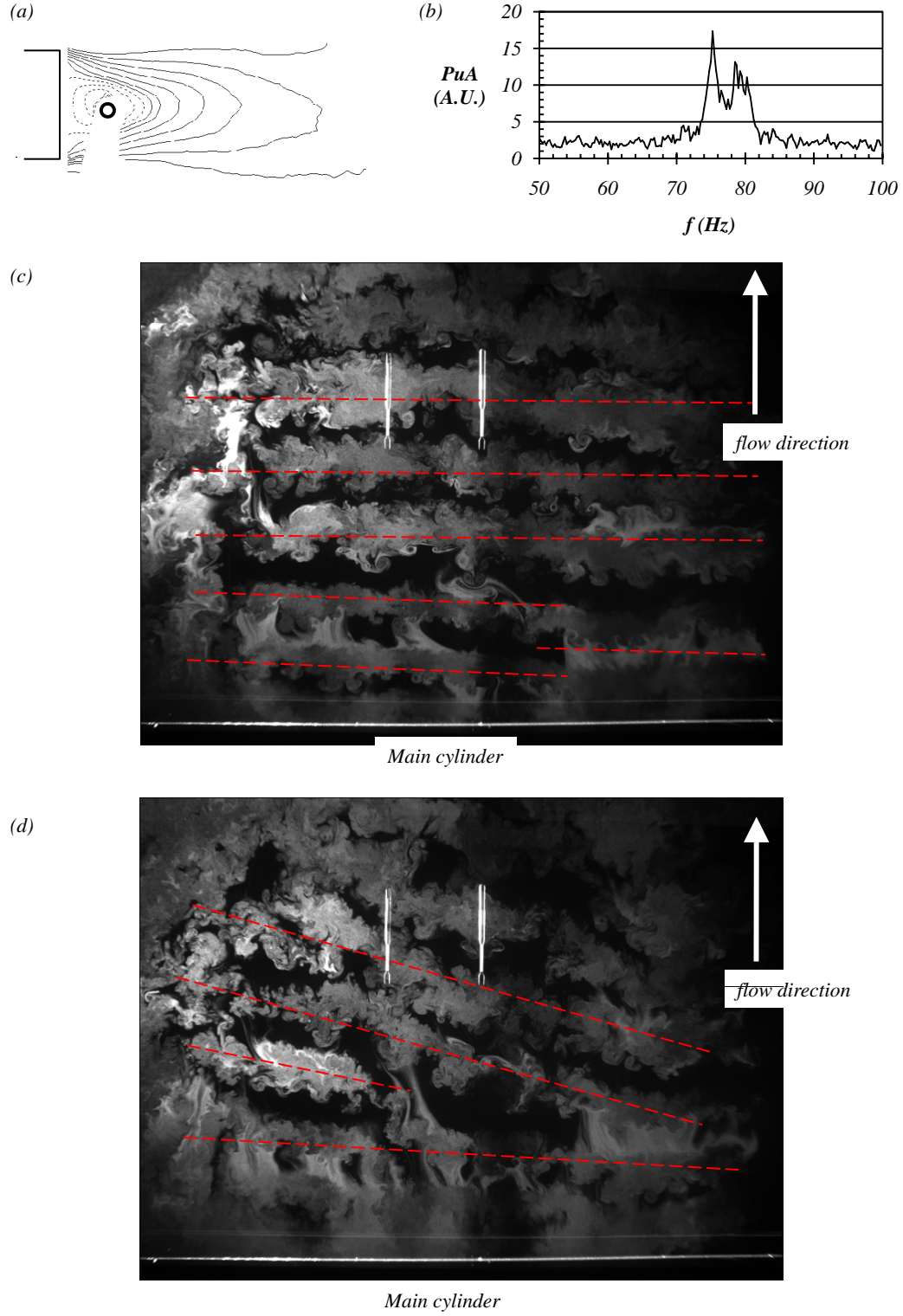


Figure 5.17: Flow patterns in the xOy plane of the wake, for the position of the control cylinder in RF configuration: (a) mean streamwise velocity (b) velocity spectrum (c) and (d) smoke visualization images of the wake.

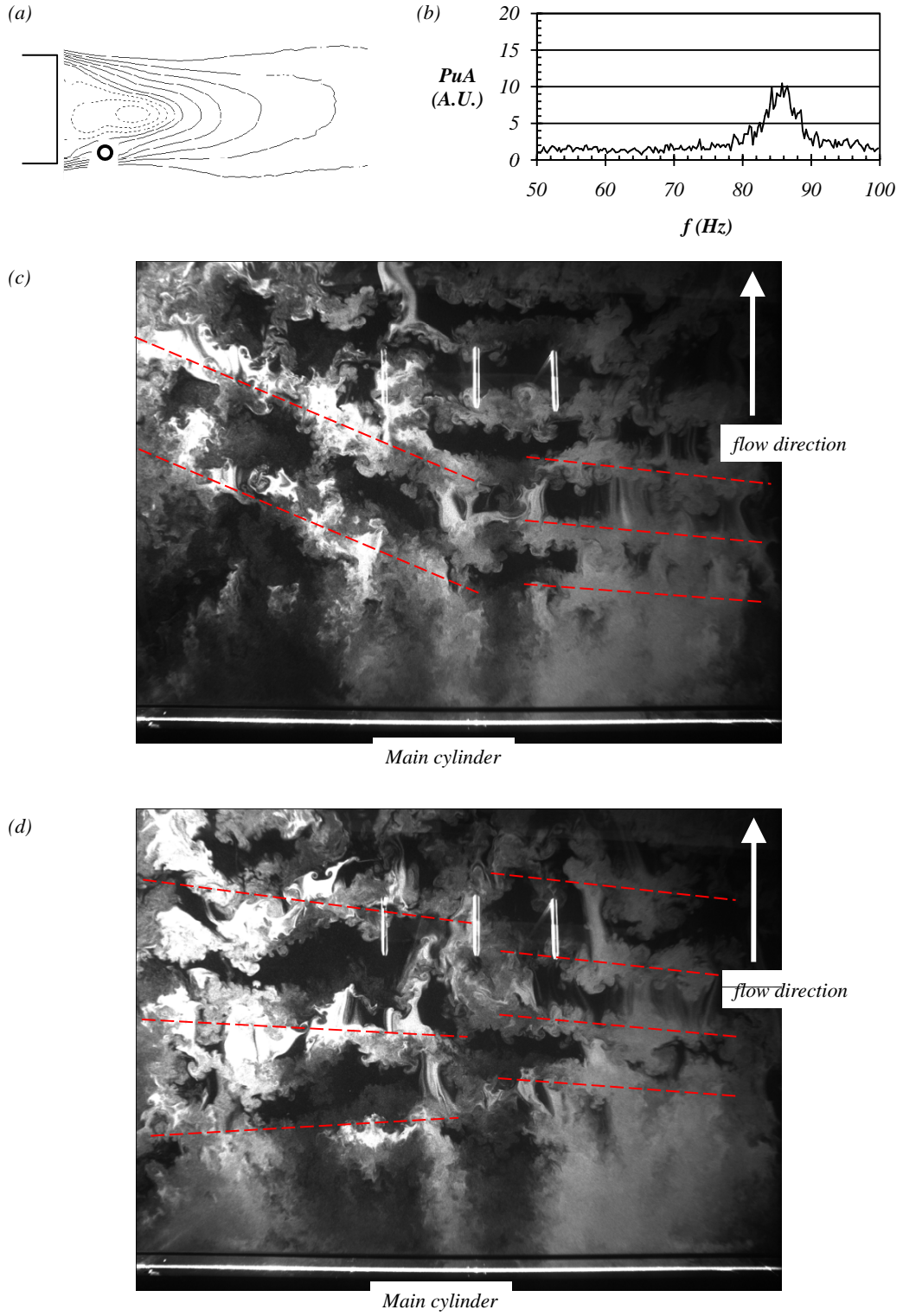


Figure 5.18: Flow patterns in the xOy plane of the wake, for the position of the control cylinder in IS configuration: (a) mean streamwise velocity (b) velocity spectrum (c) and (d) smoke visualization images of the wake.

5. BI-STABLE FLOW REGIME AND 3D EFFECTS

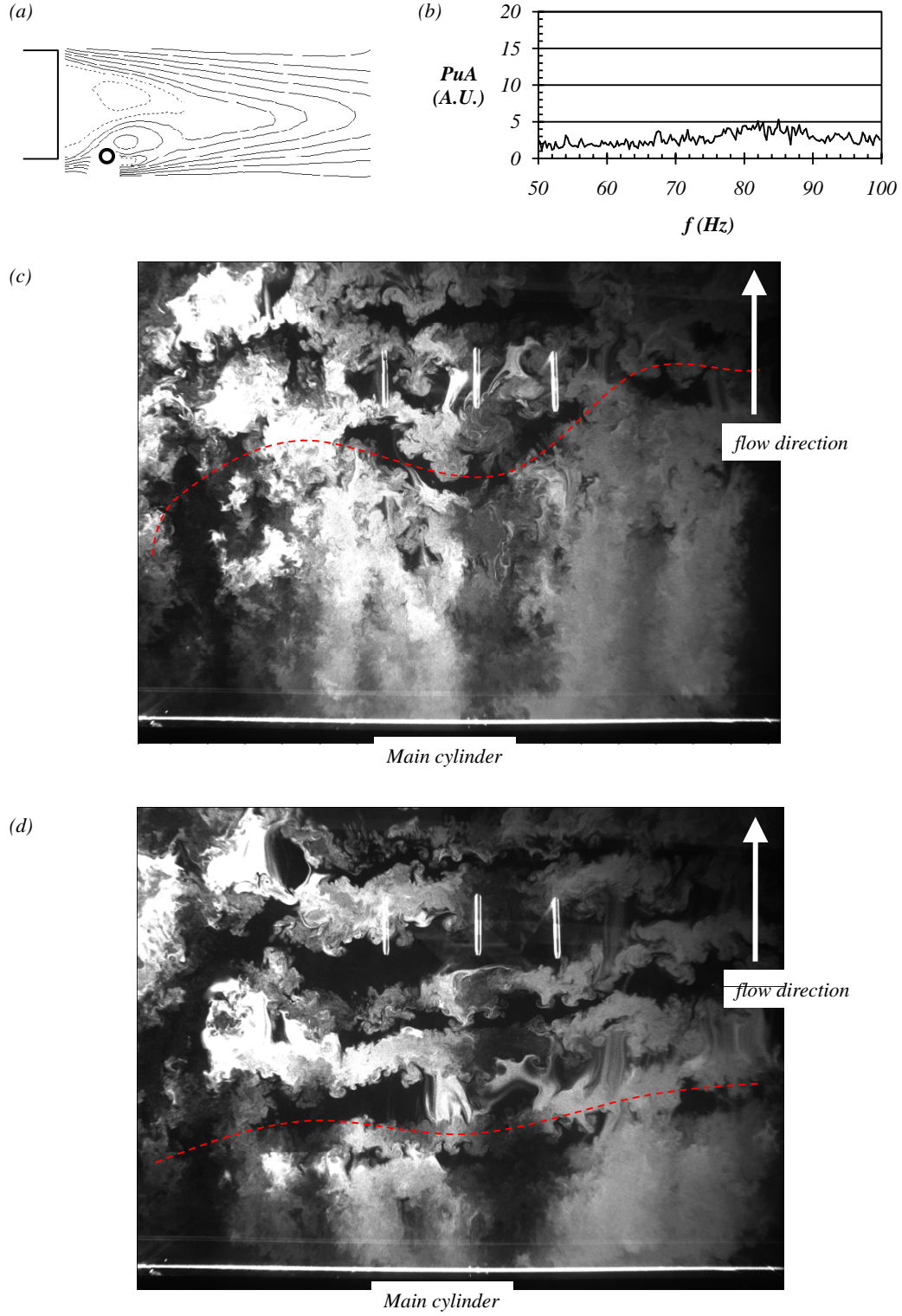


Figure 5.19: Flow patterns in the xOy plane of the wake, for the position of the control cylinder in *MS-OS* configuration: (a) mean streamwise velocity (b) velocity spectrum (c) and (d) smoke visualization images of the wake.

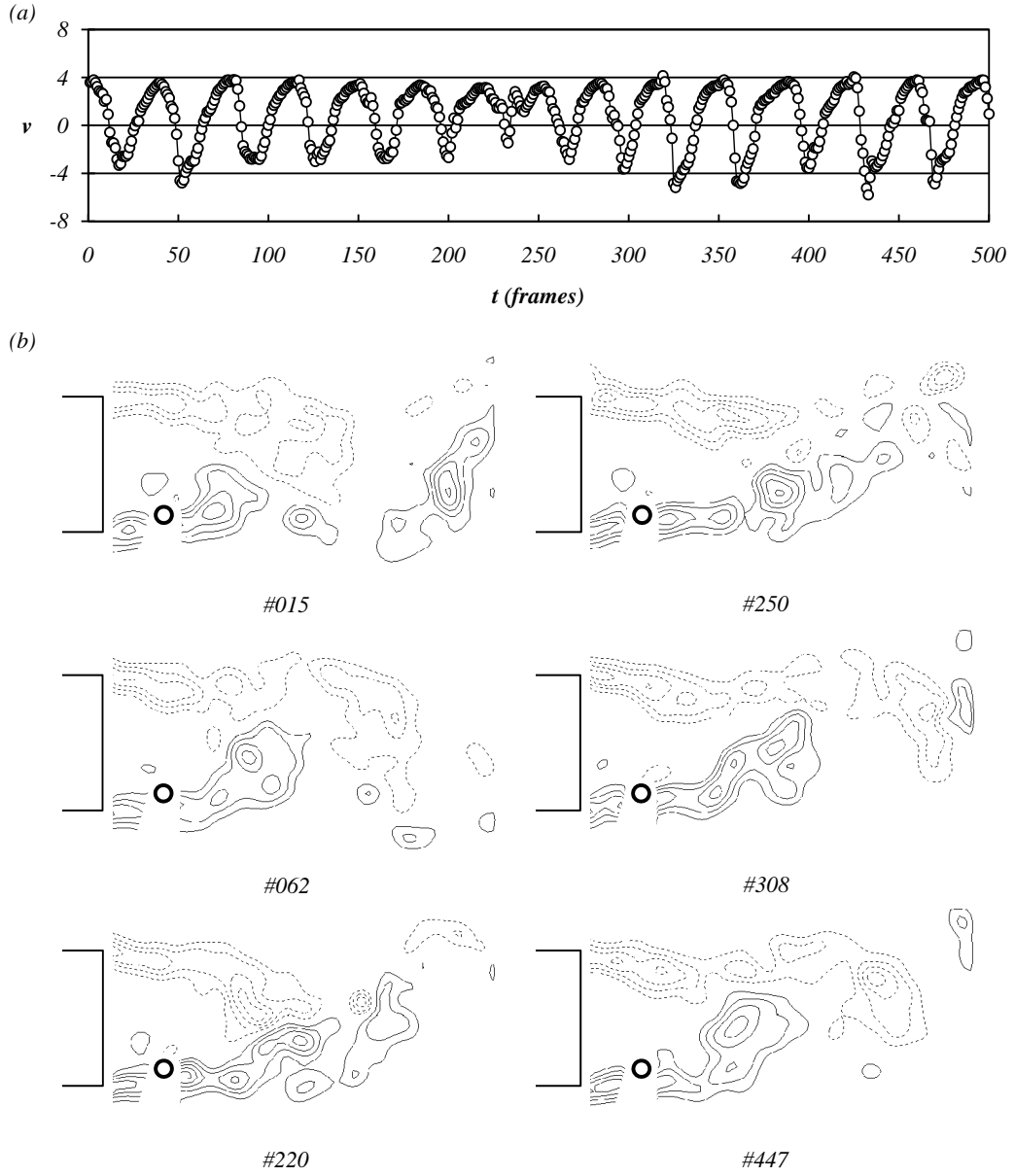


Figure 5.20: Transversal velocity $v(x, y, t)$ time signal (a) and snapshots of instantaneous vorticity ω_z at key frames (b) for 3mm control cylinder placed at (0.4,-0.38) ie. the *IS* configuration.

5. BI-STABLE FLOW REGIME AND 3D EFFECTS

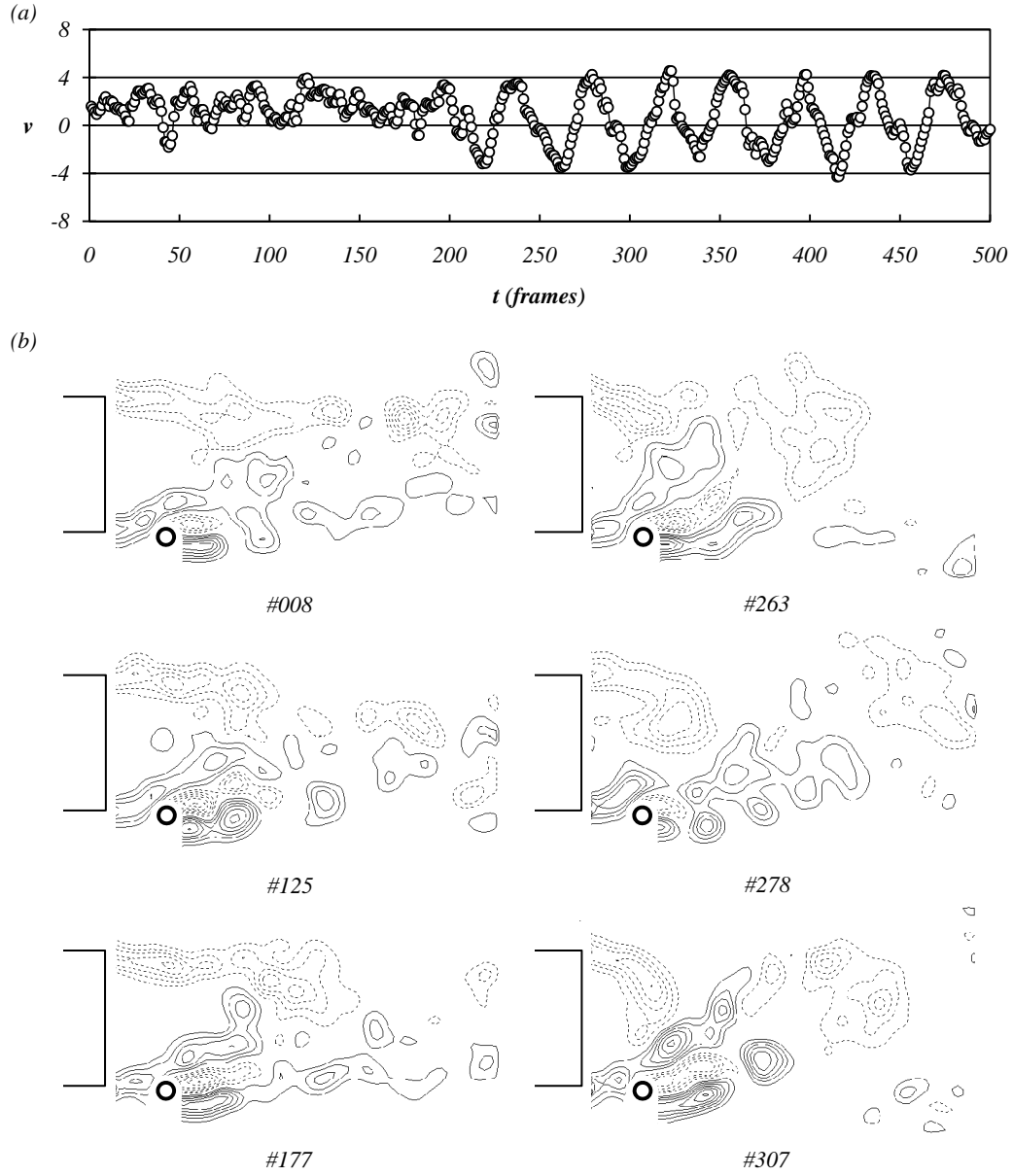


Figure 5.21: Transversal velocity $v(x, y, t)$ time signal (a) and snapshots of instantaneous vorticity ω_z at key frames (b) for 3mm control cylinder placed at (0.4,-0.6) ie. the OS configuration.

Chapter 6

Sensitivity maps

Sensitivity maps of global quantities are assembled from the measurements described in chapter 2; for each position of the control cylinder, we can extract the frequency of the global mode, base pressure coefficient and lift. We can also measure the *rms* of lift and base pressure. In the following sections we will see how the structure of the sensitive regions in the wake looks like and how does it change with regard to the Reynolds number, size and shape of the control cylinder, end plates, etc.

6.1 Anatomy of the sensitivity maps

Based on the mechanisms proposed in the previous sections of this chapter, we will now re-visit the sensitivity maps for the $3mm$ circular control cylinder and explain each significant sensitive region for the global frequency and the base pressure. The Strouhal and base pressure maps, shown in figures 6.1 and 6.2, were obtained in the mapping experiment whose details are given in section 4.1.4.

We have shown in chapter 4 how the global frequency is affected by the interactions of vorticity contained in the detached shear layers and the control cylinder, as well as the distance between the shear layers at the formation length. Based on these mechanisms, we will interpret the results matched together from the mapping experiment and the PIV measurements, shown in figure 6.1. The PIV images are given as mean vorticity $\overline{\omega_z}$, which represents well the major mechanisms mentioned above. We can recall the mechanisms of the Strouhal number change and match them to position given as $(x_c/D, y_c/D)$:

- The vorticity feedback mechanism, which is located around the horizontal centerline of the wake, and here represented by positions (0.48,0.0), (1.04,0.0) and (1.2,0.0) (outlined in yellow). Vorticity created on the control cylinder is alternatively entrained by the shears rolling-up, and vortex shedding is faster and more synchronized; the effect has a local maximum near the main cylinder, and as the control cylinder is moved downstream it is

6. SENSITIVITY MAPS

progressively weaker, until the St is returned to the natural value for bi-stable positions at (1.2,0.0) and beyond.

- The vorticity production mechanism, which is associated with the shear re-laminarization by re-attaching to the control cylinder. The characteristic positions (0.4,-0.38), (0.72,-0.38) and (0.8,-0.36) are outlined in red and are usually located in two tongue-shaped regions adjacent to the inner boundary of the recirculation bubble. In the case shown here, these regions extend far downstream, attesting to the capability of the $3mm$ control cylinder to cause the shear layer re-attachment and hence strong modifications of the mean natural flow. Position (0.2,-0.24) also show vorticity production, but a much lesser extent, since there is no attachment of the flow on the control cylinder.
- The vorticity cancellation mechanism is in the case of $1mm$ solely responsible for Strouhal number decrease. However, strong mean flow modifications which reduce the shear separating distance in $3mm$ case shown here (outlined in blue), working in conjunction with this mechanism are responsible for completely different resulting Strouhal numbers. Consequently, the Strouhal number is reduced (0.08,-0.76), natural (0.4,-0.6), and increased slightly (0.72,-0.58) and then substantially (0.72,-0.68). In a sequence like this we can say that the vorticity cancellation is slowly giving way to shear separating distance as a major effect.

In chapter 4 the base pressure is shown to be directly related to the size of the recirculation bubble. In figure 6.2 we show flow configurations typical for various regions of the base pressure sensitivity map for the $3mm$ control cylinder, in terms of mean streamwise velocity. This is a convenient way to visualize the recirculation bubble size and shape. We can discern four types of recirculation bubble increase for the $3mm$ case:

- Outlined in green are positions (0.2,-0.24) and (0.4,-0.38) which are characterized by flow re-attachment on the control cylinder. However, in the first case the base pressure is lower than the natural because the control cylinder shrouds the base of the body from the reversed flow of the bubble. Hence, the pressure at the base is reduced although the bubble is actually increased. The second position shows clearly a big bubble, which is a consequence of re-attached shear laminarization. This configuration is typical for the inner parts of the tongue-shaped regions.
- Positions shown in red outline (0.72,-0.38) and (0.8,-0.36) show typical cases of extremely elongated recirculation bubble due to a combination of flow re-attachment and the jet of displaced flow, entering the recirculation region. This is typical for the middle part of the large base pressure increase regions, and also for the downstream tips of these two big sensitivity regions.
- Due to the large size of the $3mm$ control cylinder, base pressure can be increased by vertically squeezing and horizontally extending the bubble by a blockage effect, when the

control cylinder is near the outer boundary of the bubble. Positions shown in blue outline (0.08,-0.76), (0.4,-0.6), (0.72,-0.58) and (0.72,-0.68) show such cases. These configurations are responsible for the base pressure increase in the outer parts of the two large base pressure sensitivity regions, as well as everywhere around these regions, outside of the bubble. In the case of weak mean flow modifications ($d = 1mm$), these effects are severely reduced.

- The yellow outline shows positions (0.48,0.0), (1.04,0.0) and (1.2,0.0) of the control cylinder on the horizontal axis. For this type of flow, it is characteristic that the bubble attaches to the control cylinder, when it is near the vortex formation region, or near the bubble closure. For a range of positions, the bubble will be attached, and consequently its size will grow, depending on the cylinder position. This configuration is responsible for the base pressure change at the Ox axis, ranging from natural values, to a local maximum, and then again to a lower level of base pressure increase, far downstream. We remind the reader that this lower level, as seen on the map for position (1.2,0.0) is actually only a mean value of two distinctly different bubble sizes, caused by the bi-stability and described in chapter 5.

6. SENSITIVITY MAPS

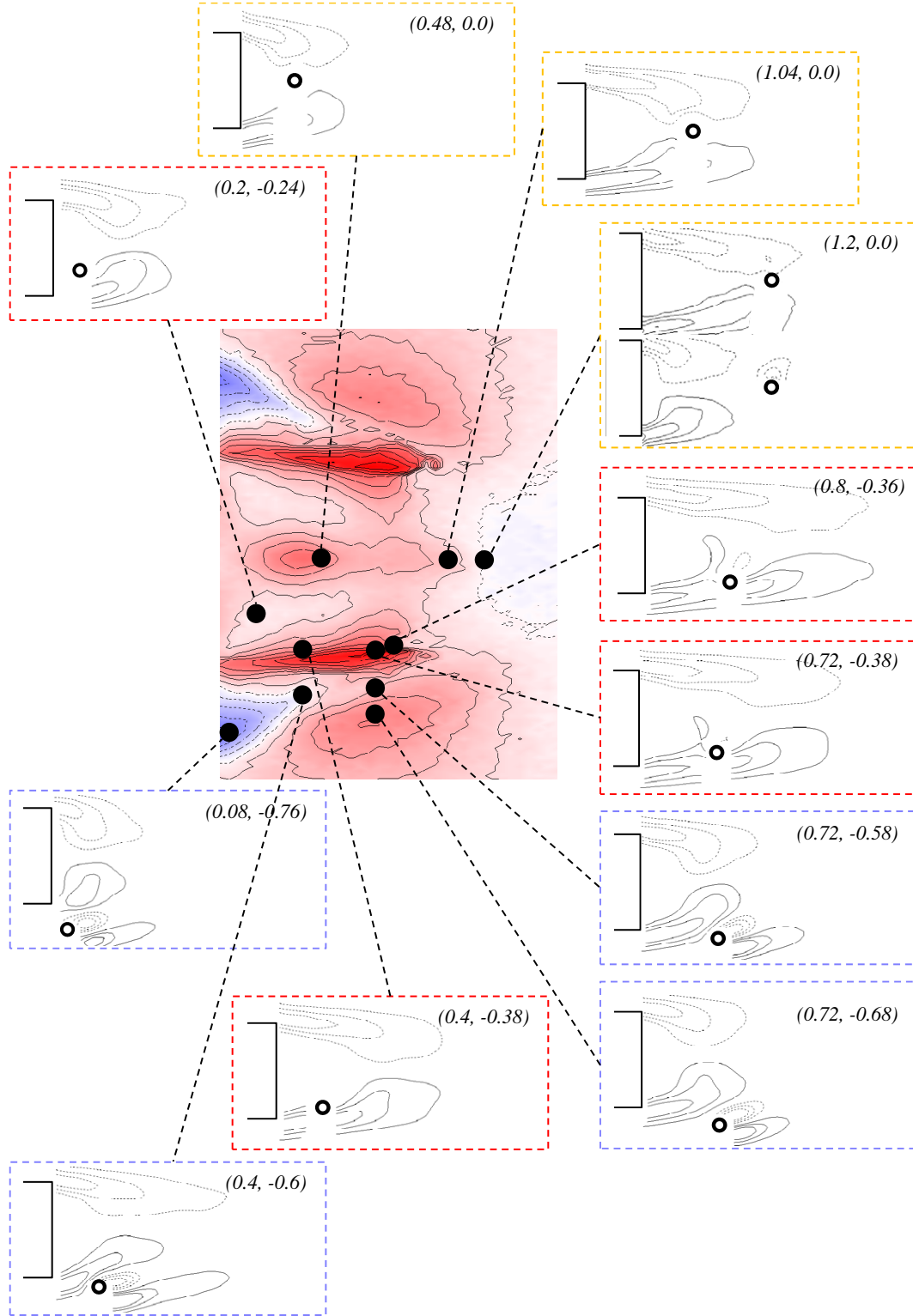


Figure 6.1: Anatomy of the Strouhal number sensitivity map. Contours of mean z-component of vorticity $\bar{\omega}_z$ are shown for each denoted position of the control cylinder.

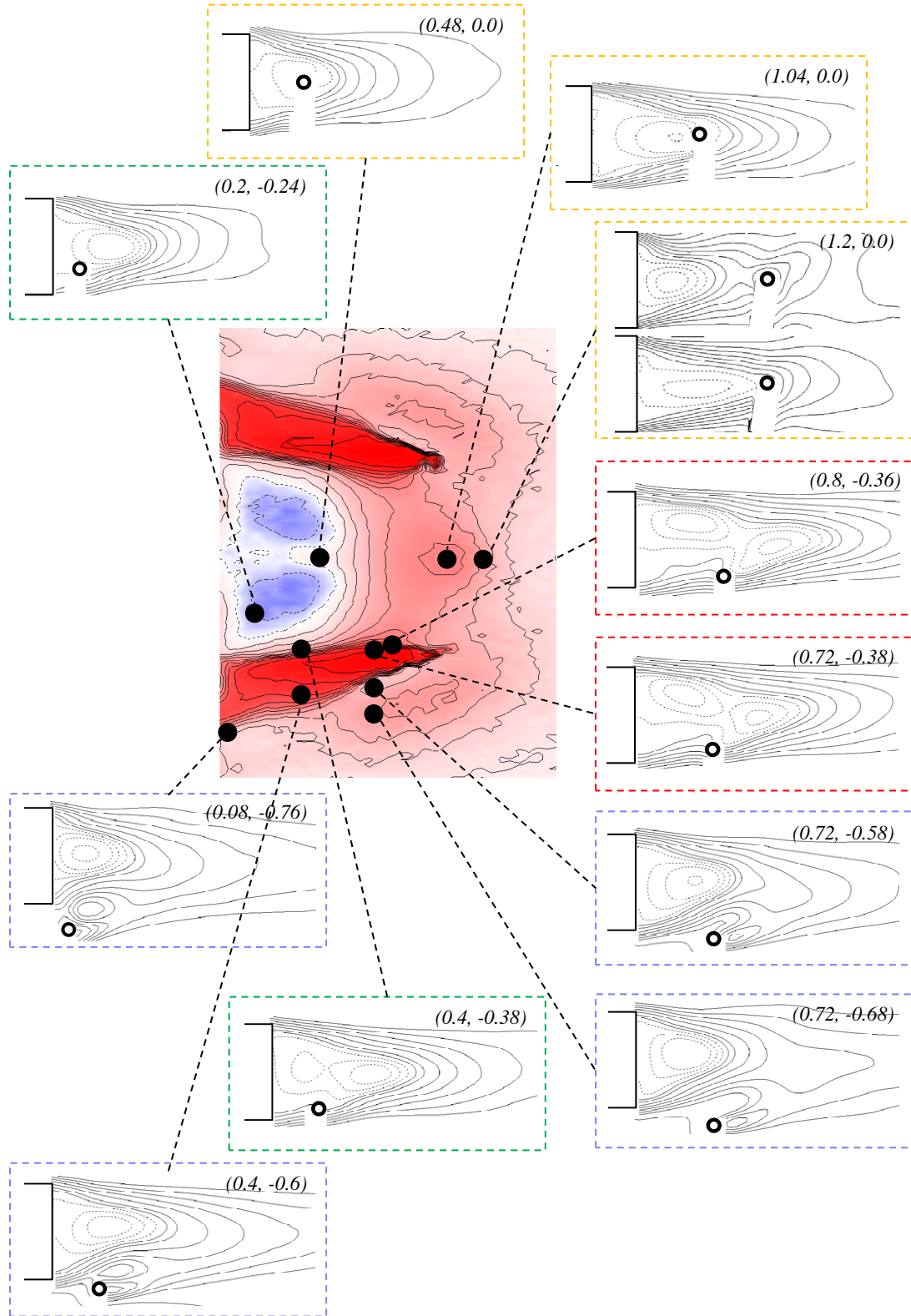


Figure 6.2: Anatomy of a base pressure sensitivity map. Contours of mean streamwise velocity \bar{u} are shown for each denoted position of the control cylinder.

6.2 Impact of the control cylinder size and the Reynolds number

The first of the two studies involves circular control cylinders of different diameters. Figure 6.3 shows the Strouhal number(a) and the base pressure (b), for control cylinder diameter varied between $d = 0.1mm$ and $d = 4mm$. The maps cover an area of $1.5D \times 1D$, below the horizontal centerline of the wake. The results show similar sensitivity structure for control cylinder diameters $d > 1mm$. At $Re = 13000$ these control cylinders are all bigger than the thickness of the shear layers at the trailing edge ($\delta_{min} = 1.25mm$, see section 3), and strong mean flow modifications are evidenced in the resulting maps. On the contrary, for diameters $d \leq 1mm$, the sensitive regions are following the shape of the natural mean bubble (shown as dashed line). This shows that we obtain asymptotic structural sensitivity map, and that control cylinders of diameter $d \leq \delta_{min}$ can be considered as a "disturbance". At the same time, the amplitudes of the effects of control cylinders are decreasing as their diameter, and for the very small cylinder of $0.1mm$ the effects on pressure are almost indistinguishable from the background noise caused by ambient temperature variations (see section 2.4). However, the maps of the $1mm$ control cylinder have a clearly visible structure and we can consider this diameter as the upper limit diameter which can be regarded as a disturbance.

The effects of the different Reynolds numbers are shown on the example of the $3mm$ circular control cylinder in figure 6.4 for the (a) Strouhal number and (b) base pressure coefficient. We have varied the Reynolds number of the experiment by changing the free stream velocity in the tunnel, and the corresponding values are indicated alongside each pair of maps in figure 6.4. We can observe an increase in the streamwise length of the sensitive regions for both St and C_{pb} , which implies flow re-attachment further downstream as the Re is increased. From the natural flow streamlines shown in figure 3.1, we can measure an increase of the natural bubble length L_{bn}/D when Re is increased, here shown by the dashed line in each map in figure 6.4. However, this increase is very small compared to the increase in sensitive regions length. The decrease of δ_{min} of the turbulent shear layers for higher Re (Rowe *et al.*, 2001) causes the control cylinder to no longer be smaller than the shear layer thickness, or to be even a larger perturbation than before, depending on its d . This can explain the increased capability of the shears to re-attach, ie. the larger mean flow modifications. What we can conclude in any case is that by decreasing δ_{min} , for higher Re , the diameter of the control cylinder needs to be decreased in order to obtain an asymptotic sensitivity map.

6.3 Impact of control cylinder shape

The flat plate control cylinder is an interesting bridge between small mean flow modifications of the $1mm$ circular cylinder, and large mean flow modifications, caused by the $3mm$ diameter. Since the dimensions of the flat control cylinder are $3mm$ by $1mm$, by rotating it around the

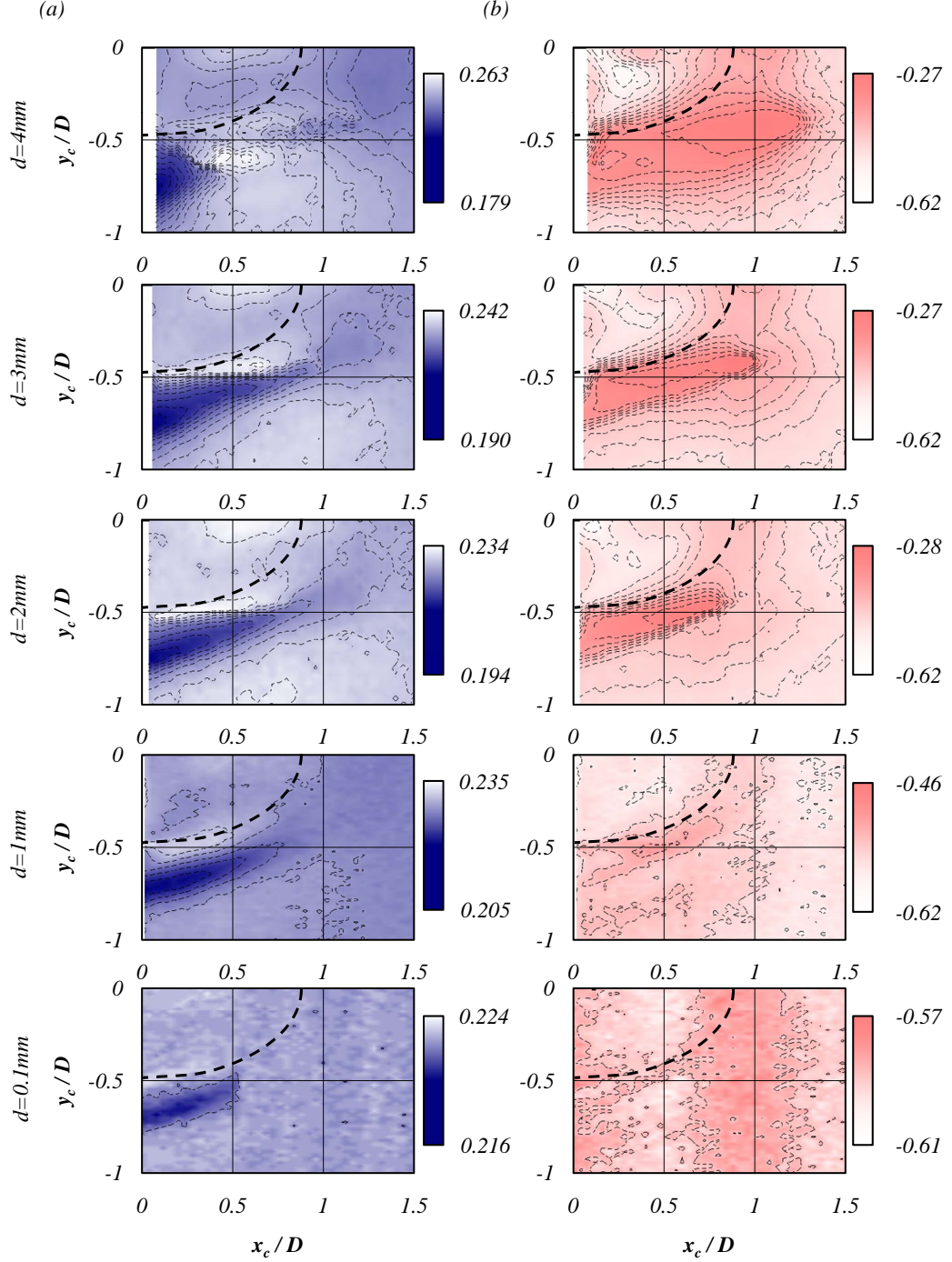


Figure 6.3: Sensitivity maps of: (a) Strouhal number and (b) Base pressure coefficient for five different diameters of the circular control cylinder. The contours are in the interval of 0.005 for the St and 0.03 for the C_{pb} .

6. SENSITIVITY MAPS

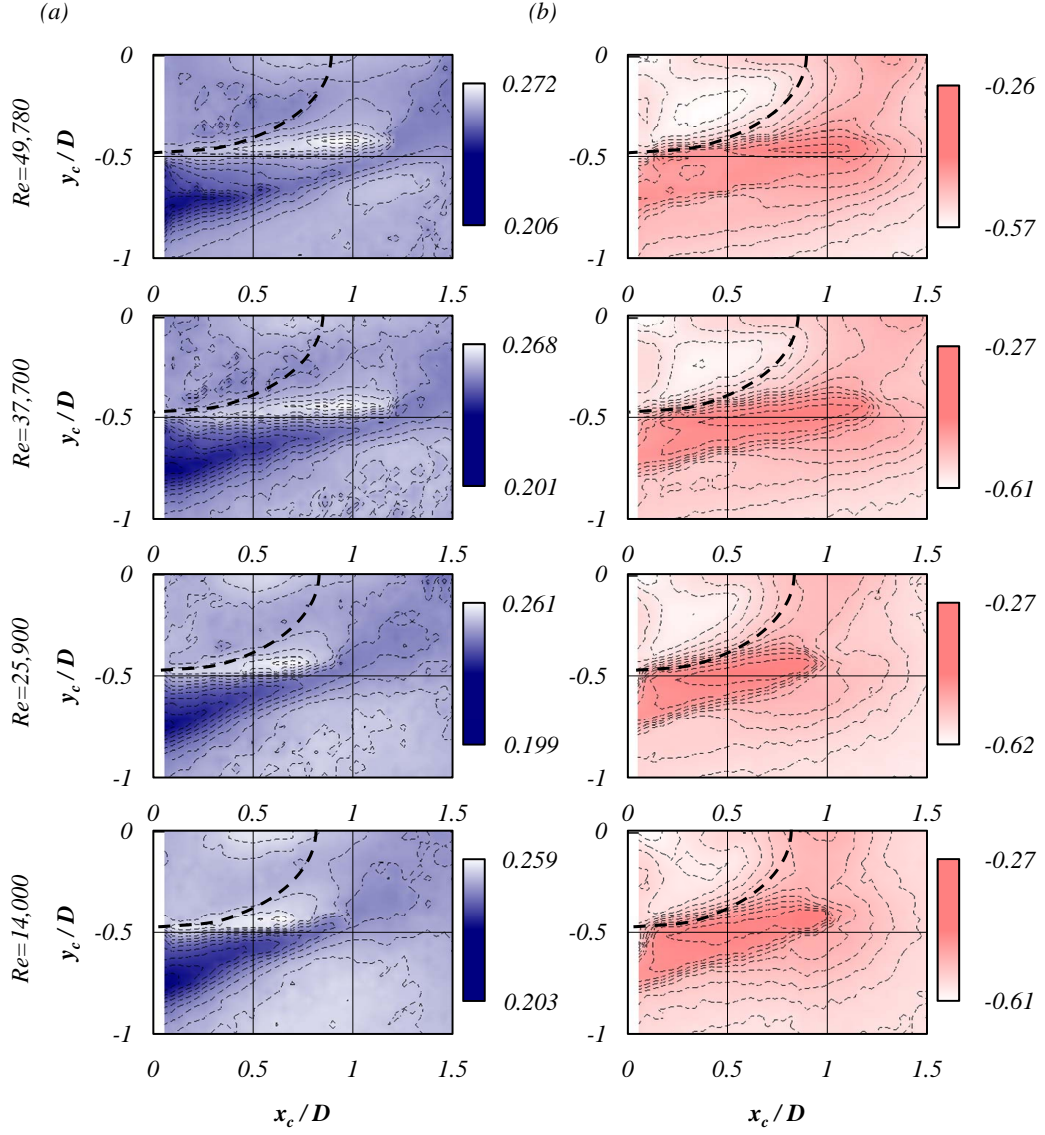


Figure 6.4: Sensitivity maps of (a) Strouhal number and (b) base pressure coefficient, for different Reynolds numbers. The contours are in the interval of 0.005 for the St and 0.03 for the C_{pb} .

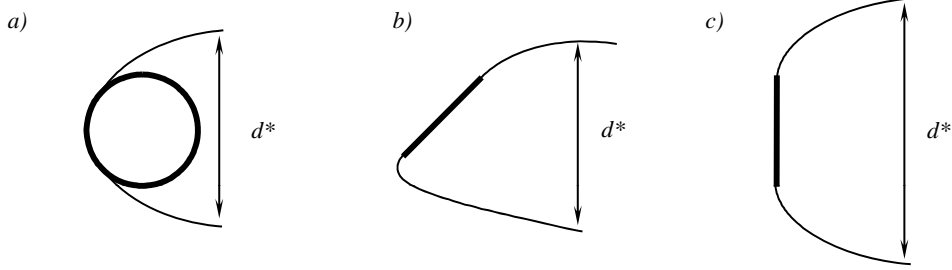


Figure 6.5: Illustration of the wake sizes for the circular (a) and flat control cylinder at different angles (b) and (c). The diameter of the circular cylinder and the length of the flat plate are the same d , and their wake heights are denoted with d^* .

middle, the incoming flow will "see" a different diameter effectively changing the "bluffness" $\frac{d^*}{d}$ of the control cylinder as illustrated in figure 6.5. Thanks to this versatility of the flat control cylinder, we can produce maps that emphasize different effects that a control cylinder can have on the wake. The following analysis is based on the mechanisms explained in section 4.4, and will refer frequently to the classification of positions of the control cylinder as defined in section 4.2.2.

The resulting sensitivity maps are shown in figure 6.6(a) for the global frequency (in terms of St), figure 6.6(b) for the mean lift, figure 6.7(a) is showing the mean base pressure and figure 6.7(b) the *rms* of base pressure. In each case the angle of the flat control cylinder is marked in the top right corner of the map, with an appropriate drawing for $\alpha = 0^\circ$, $\alpha = 45^\circ$ and $\alpha = 90^\circ$. Strouhal maps have all been re-scaled to a natural value of $St(n) = 0.221$ and base pressure maps to a $C_{pb(n)} = -0.6$. The natural values for lift and $C_{pb(rms)}$ are indicated for each particular map, and have not been re-scaled, as this was not needed due to the nature of these values. Some points in the Strouhal maps are colored black; in these areas the peak detection routine (see section 2.3.1) failed to detect an energy peak distinguishable from the noise in the spectrum.

The flat cylinder at $\alpha = 0^\circ$ produces the St sensitivity map very much like the $1mm$ circular cylinder. The effects that could be associated with the transversal dimension of the control cylinder, such as flow deviation and wake height modification are minimal. Therefore, frequency decrease caused by increased distance between shears is not observable here, and the regions of decreased frequency are shaped almost exactly as for the *OS* type interaction, for the $1mm$ circular cylinder. The St increase is much stronger in this case, and we can observe the effect exists much farther downstream than in the $1mm$ circular cylinder case. The effects on base pressure show a noticeable asymmetric effect; the difference in quality of the primary shear layers obviously favored the lower shear for re-attachment to the control cylinder. We can see that the base pressure is increased, substantially farther downstream, when the control cylinder is interacting with the bottom shear. The lift map is symmetric in structure but not

6. SENSITIVITY MAPS

in amplitude, but this is probably due to the imperfections in experiment global symmetry (see section 2.4) to which lift is very sensitive. In any case, we can state the following remarks: the flat control cylinder produces sensitivity regions similar to the $d = 1mm$ in the transversal sense, but in the streamwise sense the effects of flow re-attachment are the dominant factor. The shear layers are re-attaching to the flat face of the plate, causing the effects of vorticity production and recirculation bubble elongation as in the *IS* case of the $3mm$ cylinder, which in turn increases the global frequency and base pressure.

For the $\alpha = 45^\circ$ we can observe a true mix between the $1mm$ and $3mm$ cases. The flat control cylinder is facing the flow in a different manner depending on whether it is above or below the horizontal axis of the wake. On average, the flow will arrive nearly perpendicular to the control cylinder, when the latter is in the bottom part of the wake. When the control cylinder is in the upper part of the wake its shape follows the streamlines of mean velocity and the flow encounters its small frontal face. Both the St and C_{pb} maps suggest a strong affinity for shear re-attachment in the bottom part of the wake. So when the flow encounters the larger face, the sensitive regions are created as for the $3mm$ control cylinder. Otherwise, the effects in the upper parts of the map are mostly caused by the same mechanisms as in the case of the $\alpha = 0^\circ$, ie. the flow is slightly influenced by the length of the control cylinder, and as such is attached at time, but there is not much flow displacement and wake height modification.

For the case of the flat control cylinder at $\alpha = 90^\circ$, it is obvious that there is a lot of flow displacement around its edges. The incoming flow sees a flat plate of $3mm$ in height and depending on the position of the control cylinder, strong secondary shear layers are formed on one or both of its edges. As illustrated above, the wake of the flat cylinder at this angle is probably closer in height to a wake of a $d = 4mm$ circular control cylinder. Indeed if we compare the $\alpha = 90^\circ$ map in figure 6.6(a) with the $d = 4mm$ map in figure 6.3(a), we can observe a very similar pattern of sensitivity regions.

For this case of the flat cylinder, we can measure a largest envelope of frequency change. The frequency is strongly changed in regions which are created by flow displacement, ie. when the frequency is modified by modifying the wake height as in the case of *MS* to *OS* transition for the $3mm$ circular cylinder. At the same time frequency modifications due to vorticity production are less present, since vorticity production implies flow re-attachment, which is weaker in this case. For the same reason, the envelope of base pressure is not much increased. This envelope is rather shifted towards decrease of base pressure. However, the area of the base pressure sensitive regions is much bigger than in previous cases. This confirms that the flow modifications are mostly from flow displacement due to blockage as in a typical *OS* or *EF* case for the $3mm$ circular cylinder, when the bubble is squeezed vertically, but its length is increased. However, this length increase is not as effective as when the same control cylinder is in the *MS* position and the flow is displaced inside the wake as a jet. In our case here, the bubble doesn't grow as in the circular cylinder *MS* case, because when the flat cylinder is in a similar position, its geometry effectively blocks the jet from entering and injecting momentum into the bubble.

As far as the base pressure changes for the *RF* configuration are concerned (shown in figure 6.7a), it is clear that the control cylinder is acting as a shroud by preventing the reverse flow from imposing pressure on the base of the main cylinder. When the flat cylinder is horizontal, it can only affect one point of base pressure measurement, and that only when in it very close to the trailing edge. When it is in the vertical position, it clearly has a big impact, and the pressure ports at the base of the main cylinder register a low pressure. The fluid in the wake between the control cylinder and the trailing edge is probably quite stagnant in this case. Some examples of flow dynamics with a perpendicular plate in the wake of a bluff cylinder can be seen in Bentley & Mudd (2003), albeit for a lower *Re* number and a much larger plate.

The *rms* of base pressure is shown in figure 6.7(b). In all three cases the maps of $C_{pb(rms)}$ are quite similar to their counterpart for the 3mm circular cylinder. The main differences are in terms of the sizes of the sensitive areas, while the envelopes of fluctuations are very similar in all cases. It is apparent that the flat cylinder at $\alpha = 90^\circ$ is also capable of causing the bi-stable flow configuration. However, the re-attachment of the primary shears on the edges of a flat cylinder angled in such a manner is quite a difficult task for the flow, and so, the bi-stability is present for more different vertical positions of the control cylinder than usual, but at a more strictly localized region in the streamwise sense.

6.4 Extended sensitivity map for $d = 1mm$ circular cylinder

Although the primary focus of this work was to investigate and characterize the interaction between the free-shears in the wake and a control cylinder, we have extended the mapping of the global properties for the case of the 1mm control cylinder, in order to construct a sensitivity map all around the main cylinder. The maps of the global frequency in figure 6.8(a) and base pressure in figure 6.8(b) are obtained from three different experiments to cover the entire region. The first part, which was obtained as a part of the main investigation, is covering the wake area in the range $0 < x_c/D < 1.8$ with a resolution of the control cylinder displacement of $\Delta x_c \times \Delta y_c = 1mm \times 0.5mm$. The second part covers the region above the flat portion of the main cylinder in the range $-1.5 < x_c/D < 0$ with the same resolution as above. The third part covers the area in front of the semi-circular part of the main cylinder; in the range $-2.2 < x_c/D < -1.5$. For this area the control cylinder displacement resolution is increased to $0.5mm \times 0.5mm$ in order to precisely follow the wall curvature. The total duration of these experiments to produce this map was 87 hours.

Figure 6.8(c) shows the streamlines of the natural flow as a case of reference for the mean boundary layer/shear layer locations and geometry. When the sensitivity of the wake ($x_c > 0$) is investigated, the control cylinder changes neither the detachment points of the shear layers nor influence significantly the boundary layer development along the body. On the contrary, upstream of the detachment ($x_c < 0$), the small 1mm control cylinder can impose strong

6. SENSITIVITY MAPS

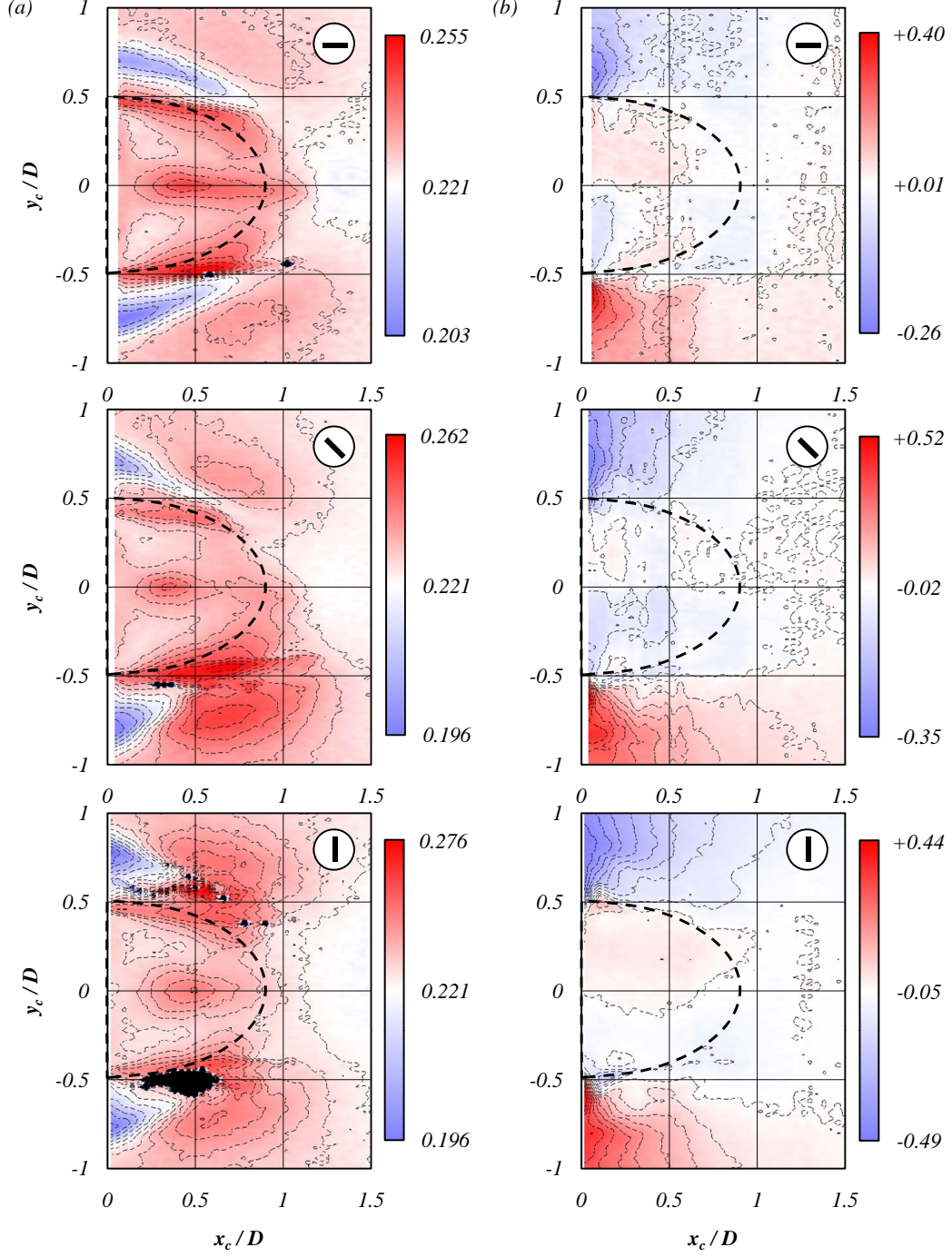


Figure 6.6: Sensitivity maps of (a) Strouhal number St and (b) mean lift coefficient C_l , for the flat control cylinder. The chevron in top right corner of each map indicates the angle (0° , 45° or 90°) of the control cylinder for the corresponding map. The contour lines are in the interval of 0.005 for St , and 0.05 for C_l .

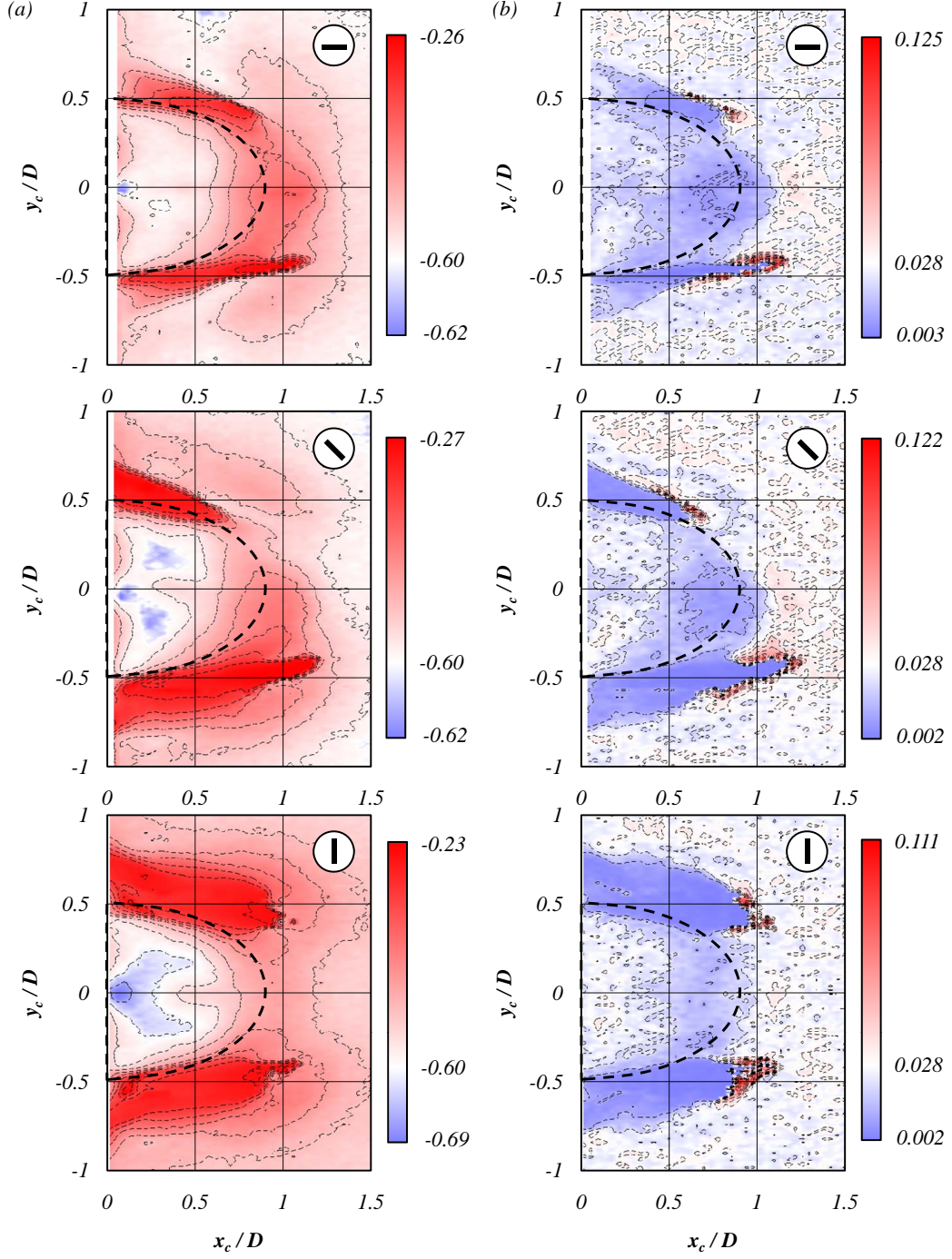


Figure 6.7: Sensitivity maps of (a) mean base pressure coefficient C_{pb} and (b) rms of base pressure $C_{pb(rms)}$, for the flat control cylinder. The chevron in top right corner of each map indicates the angle (0° , 45° or 90°) of the control cylinder for the corresponding map. The contours are in the interval of 0.05 for C_{pb} and 0.01 for $C_{pb(rms)}$.

6. SENSITIVITY MAPS

modifications to the history of the boundary layer. The region ($x_c > 0$) being thoroughly discussed in previous chapters, we will here only comment on most prominent features of the newly added parts of the sensitivity map ($x_c < 0$).

A reduction of the global frequency is clearly visible. This effect can be attributed to the vorticity cancellation mechanism (see section 4.4.1) since the control cylinder is just above the boundary layer. The effect of the sensitivity of the small separated region near the wall at $-1.5 < x_c/D < -0.5$ is observable on both the base pressure and global frequency. The large base pressure increase near the wall at $-1.5 < x_c/D < -0.5$ indicates that a thinner shear (having small entrainment velocity) initiates the wake compared to that of the natural flow (see section 4.4.2). This can be achieved because the control cylinder placed in a favorable pressure gradient near the wall at $-1.5 < x_c/D < -0.5$ will provoke turbulent transition in the boundary layer and certainly suppresses the detachment at $x_c = -1.5D$. As a result, a thinner turbulent boundary layer should be observed at $x_c = 0$. A large decrease of the base pressure (blue region in figure 6.8b) is observed in the reattachment region of the small separated region. It indicates that a thicker shear (having large entrainment velocity) initiates the wake (see section 4.4.2). This can be achieved because the control cylinder placed in or after the reattachment region creates an adverse pressure gradient that is able to either increase the shear thickness or provoke early separation. Further experimental verification of these assumptions would be needed before any definite conclusion are made, unfortunately this work would go beyond the scope of this thesis.

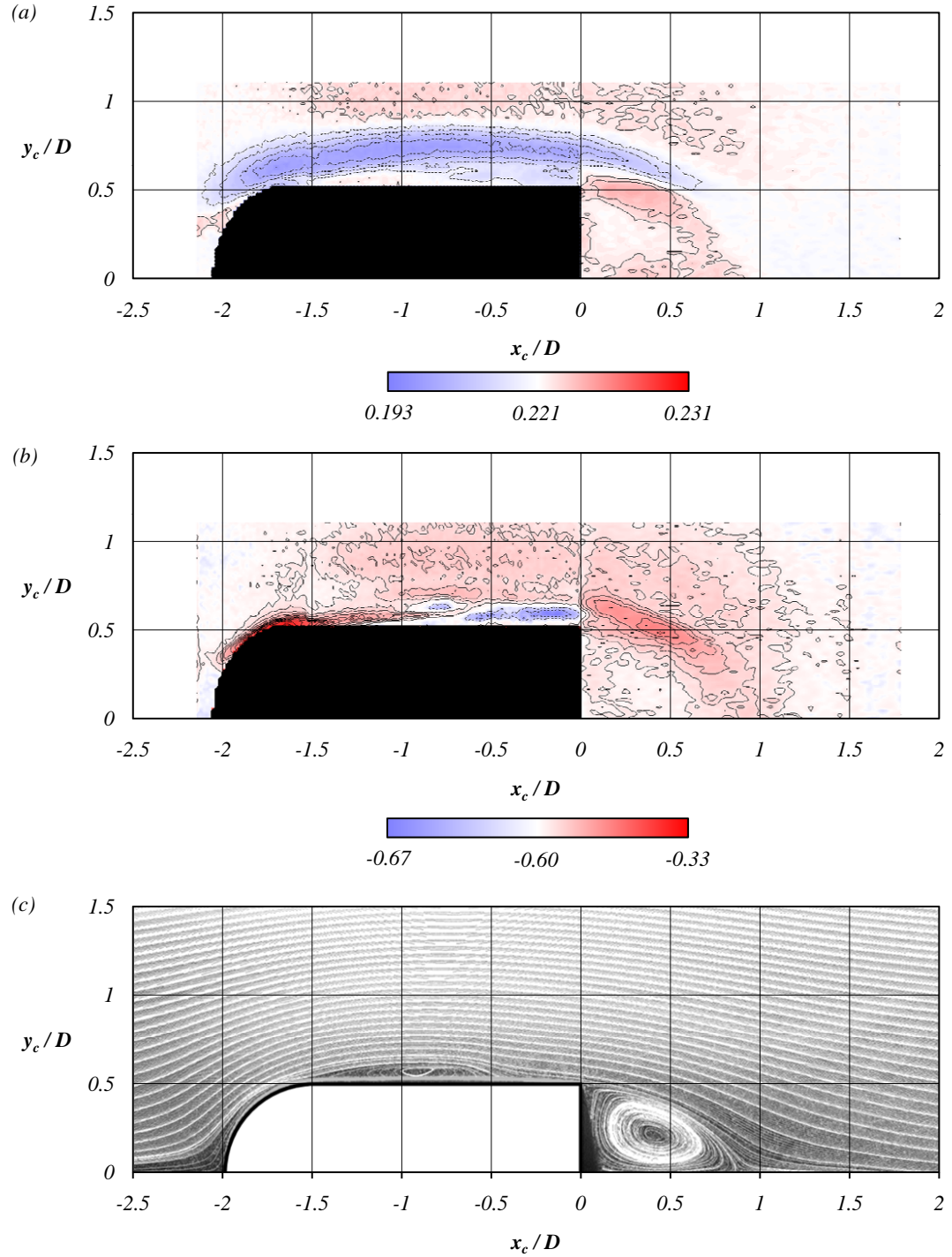


Figure 6.8: Sensitivity map around the bluff cylinder for the 1mm circular control cylinder. (a) Map of the Strouhal number with contour lines in interval of 0.005. (b) map of the base pressure coefficient C_{pb} with contour lines in interval of 0.05. (c) Streamlines of the mean natural flow.

6. SENSITIVITY MAPS

Chapter 7

Conclusion

The flow around a D-shaped bluff cylinder at high Reynolds numbers is investigated in chapter 3 as a basis for our sensitivity analysis. At $Re \approx 13000$ we find fully turbulent shear layers detaching from the trailing edge of our bluff cylinder. The wake so created is dominated by a global mode known as the Kármán vortex street.

Our main objective is to explain the changes in global properties of this wake when a small control cylinder is placed in it. The idea is to construct a sensitivity map of a turbulent wake and elucidate on the mechanisms governing the modification of global properties. The experiments involved several different sizes and shapes of control cylinders. In chapter 4 we focus on two particular diameters of a circular control cylinder, one bigger than the initial thickness of the detached shear layers and the other one smaller. The resulting Strouhal and base pressure sensitivity maps show an elaborate structure of regions in the wake, sensitive to the presence of a control cylinder. PIV wake measurements reveal mean flow and global mode structure modifications for key positions of the control cylinders in the vicinity of the detached shear layers.

From the results, we have proposed a mechanism based on the efficiency of the control cylinder to change the size of the formation region mainly through the modification of the turbulent properties of the perturbed shear layer. The physical mechanism explains the observed modifications of the spatial structure of the global mode and its amplitude as well as the global frequency selection and the drag reduction. The main changes in the global mode frequency are interpreted in terms of shear diffusion and separating distance between the shear layers participating in the global mode. The global mode spatial structure is closely related to the base pressure (ie. the drag), through the formation length, and their relationship is recovered similarly as for the cavity models (Wu, 1972). A striking difference compared to the sensitivity analysis at low Re (Giannetti & Luchini, 2007; Luchini *et al.*, 2008, 2009; Marquet *et al.*, 2008; Strykowski & Sreenivasan, 1985, 1990), for which the global frequency is always decreased, is that at large Re the global mode damping can be either accompanied by a low or high vortex

7. CONCLUSION

shedding frequency.

A strong increase of fluctuations of aerodynamic forces on the main cylinder is found for certain positions of the control cylinder. This is identified in chapter 5 as a bi-stable flow configuration for which the wake alternates between two significantly different formation region sizes.

The influence of the control cylinder on the 3D properties of the wake is presented in the same chapter. This is examined through spatial correlation of local velocity measurements in the wake, as well as flow visualization. Correlation coefficients show improved wake synchronization, whenever the control cylinder is placed inside the recirculation bubble. However, positions of the $3mm$ control cylinder which cause strong damping of the global mode also result in correlation reduction.

In chapter 6 we revisit the sensitivity maps and review the origins of the different sensitive regions through the mechanisms revealed in previous chapters. In light of this, we explain the effects on the sensitivity map structure of different shapes and sizes of the control cylinder and different Reynolds numbers. Mapping experiments performed with a $0.1mm$ circular control cylinder show the same structural sensitivity as the $1mm$ control cylinder but with amplitudes just distinguishable from the background noise. We therefore conclude that the $1mm$ control cylinder causes sufficiently small mean flow modifications and can be treated as a "disturbance", at the Reynolds number of our main experiment.

As a final effort to complete the analysis, extended mapping experiment is performed, which investigates the sensitivity of the flow all around the main bluff cylinder. In this case, the obtained global mode sensitivity results from both boundary layer and free shear layer control. This makes the extended sensitivity maps of the $1mm$ circular cylinder good candidates to be compared to future theoretical results of the structural sensitivity analysis of a turbulent wake. It would be an interesting challenge for theoreticians to recover these maps.

Several questions remain to be answered experimentally, which have not been fully addressed due to project schedule considerations and also problems of availability of proper equipment (such as high-speed PIV):

- Complex boundary layer history, which changes significantly with the Reynolds number of the flow.
- Shear layer thickness at formation length, which remains elusive due to the unsteady nature of the wake. This contributes significantly to the global mode frequency selection.
- Primary wake and control cylinder wake interaction, and the effect of this on the global frequency.

Sometimes, one would travel the entire road leading to a conclusion of one issue, only to be faced with a new dilemma. Still, considering how many degrees of freedom are inherently contained in the problem of bluff-body turbulent wakes, we believe that the answers one might possibly

find in this work make a solid contribution to our comprehension of the involved phenomena. We hope that this work not only consolidates our knowledge of 2D wakes, but also opens venues for investigations of steady perturbation control of wakes behind 3D bodies, such as axis-symmetric cylinders or the "Ahmed body". A successful experimental investigation with such goals, followed up by the 3D sensitivity predicting theory would make a huge impact in the possibilities of practical application of the bluff-body wake control.

7. CONCLUSION

Appendix A

Jet

One of the experiments performed during the investigation of the relationship between the drag and the length of the mean recirculation bubble involved injection of momentum into the recirculation bubble by a jet blowing from the base of the main cylinder. Similar experiments with the aim of drag reduction have been performed using passive wake ventilation by [Suryanarayana *et al.* \(1993\)](#) and [Grosche & Meier \(2001\)](#).

In section [4.2](#) we have seen that when the control cylinder of a certain size is placed at specific locations, the high velocity fluid is deflected between the trailing edge of the main cylinder and the control cylinder, directly into the low velocity recirculation region. This causes the mean bubble to expand downstream; ie. the shear layers roll up later, in order to increase the length of entrainment so as to be able to absorb the additional momentum. Please refer to chapter [4.4](#) for the detailed description of this mechanism.

The objective of this experiment was to see what would happen if we artificially injected additional momentum into the recirculation bubble, when the control cylinder is not present in the wake. How does the mean bubble adjust to this imbalance in momentum? How does the base pressure change because of the jet at the trailing edge, since the jet creates a region of low pressure immediately behind the main cylinder?

The experiment was performed by attaching a perforated tube to the $3mm$ circular control cylinder. Figure [A.1](#) shows some details of the hardware setup. The perforated tube was too short to be mounted directly on to the support frame, so we had to keep the control cylinder as support. The control cylinder and the additional tube are placed at $x_c = 0, y_c = 0$. The openings on the tube are facing downstream, so that the jet will blow into the Ox positive direction. The perforated tube is $2mm$ in diameter, and has 15 holes of $\phi 0.5mm$ along a span of $300mm$. Its ends are connected to plastic tubes which supply it with air from the PIV particle dispersal unit. We didn't measure any specifics of the jet like its mass flux or speed, since it is not relevant in our case. What we are interested in is to compare a case where the jet is active and when it is not, and see how does the mean recirculation bubble adapt.

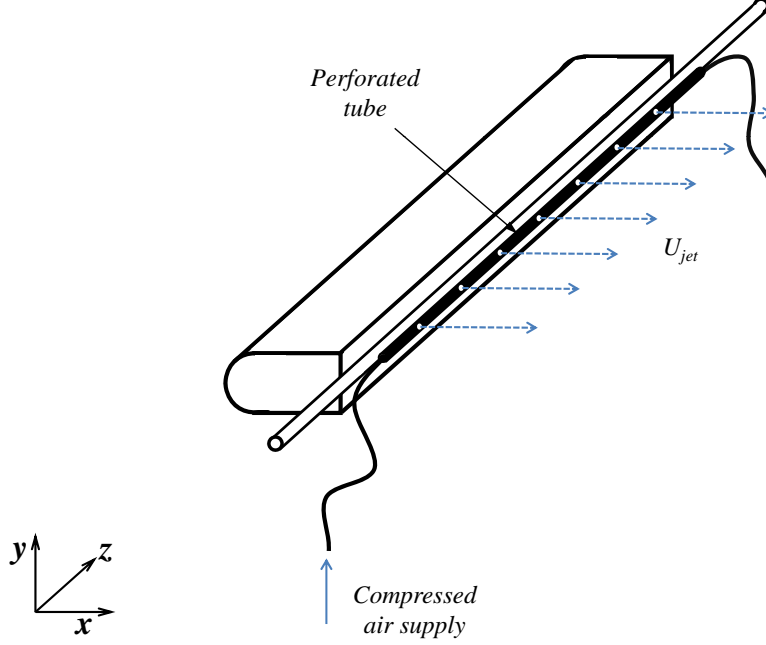


Figure A.1: Experimental setup with the perforated tube attached to the control cylinder.

Figure A.2 shows the pressure distribution for the case of no jet depicted in hollow circles, and when the jet is switched on shown with filled circles. We can notice that the difference between the two cases is noticeable for pressure recorder by the ports at the base of the main cylinder. The case with the active jet shows a higher base pressure and if the mechanism of bubble equilibrium is still at work here, we expect to see an enlarged mean bubble.

Indeed, the PIV measurements of the two cases, shown as mean modulus of velocity in figure A.3, shows different mean bubble sizes for the two cases. For the first case, when the control cylinder and the perforated tube are present, but the jet is not active, the recorded base pressure is $C_{pb(passive)} = -0.56$. This is not exactly the same as the natural value, but it is expected since the jet tube is present in the wake. From the PIV mean velocity field, we obtain the length of the recirculation bubble as $L_b(passive) = 0.86D$. In the case of the activated jet, these values are $C_{pb(active)} = -0.44$ and $L_b(active) = 1.13D$. These points can also be seen in figure 4.29, where we have plotted the relationship between base pressure and recirculation bubble length.

In conclusion, this short study confirms that the recirculation bubble equilibrium of momentum is maintained by the same mechanism we have described previously, regardless of how the momentum is changed, whether by outside flow being deflected into the wake, or by directly adding momentum from a separate source. Whatever the source of added momentum, the shear layers which are forming the recirculation region will adapt their length.

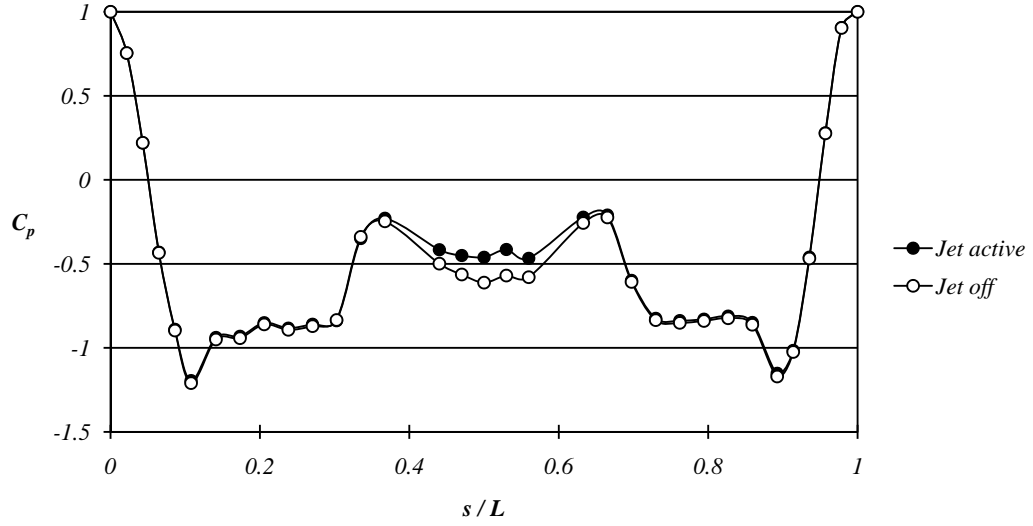


Figure A.2: Pressure distribution around the main cylinder for activated (filled circles) and deactivated (hollow circles) base bleed.

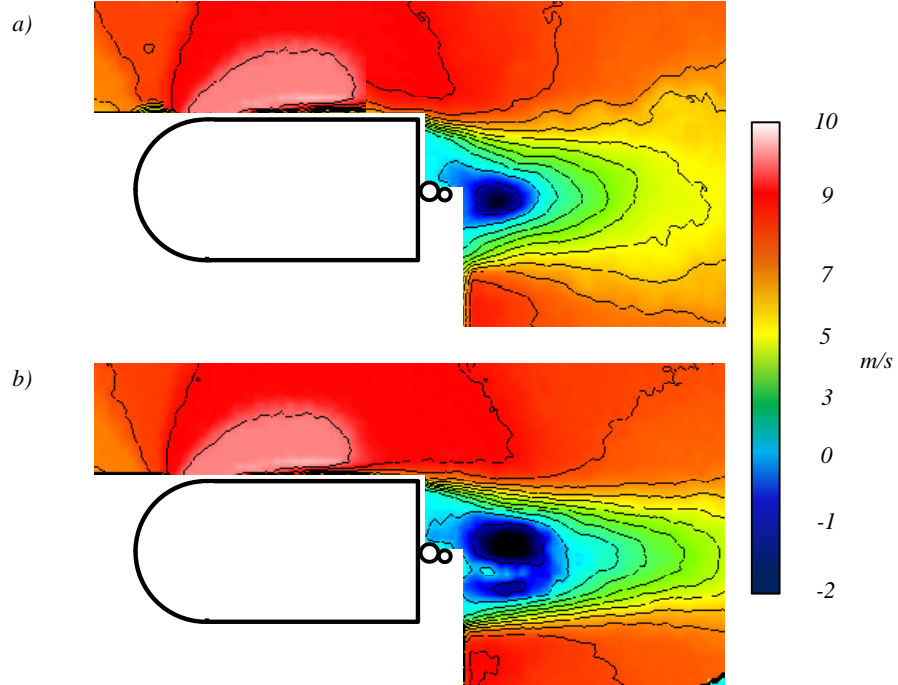


Figure A.3: Mean streamwise \bar{u} velocity fields obtained by PIV for (a) no base bleed and (b) base bleed in effect.

A. JET

Appendix B

Trailing edge flap

Splitter plates and trailing edge plates are very frequently used in experimental investigations of bluff body wakes. While the former is a completely different influence on the wake, and not very compatible for comparison with our investigation, a trailing edge plate, or a flap is especially of interest to us, since it too interacts with the shear layers before their roll-up. We performed an experiment involving a flat plate attached to the lower trailing edge of the main cylinder, and we have measured its effect on the pressure distribution and the recirculation bubble.

The dimensions of the flap are $10mm \times 0.5mm$ ($l_{flap} \times h_{flap}$) with an equal span as the main cylinder, ie. $24D$. Figure B.1 shows the details of the flap position. The flap has five angular positions with regard to the horizontal axis: $\alpha = 0^\circ$, $\alpha = \pm 15^\circ$ and $\alpha = \pm 45^\circ$.

We have recorded the pressure distribution for each of these positions and for a natural wake, as shown in figure B.2. From the pressure measurements we can see that the main modification is on the bottom side of the main cylinder, as expected, since the flap is attached to the bottom trailing edge. The biggest modification of pressure on the bottom of the main cylinder is caused by the flap deflected outwards at $\alpha = 45^\circ$. For this position we can even notice a change in the pressure at the head of the main cylinder, near $s/L = 1$. However, the biggest modification of the base pressure comes when the flap is deflected inwards at $\alpha = -15^\circ$. These pressure modifications are much clearer after the analysis of the PIV measurements shown in figure B.3. Here we present the mean velocity in the wake with an overlay of streamlines, for each case. Natural case for this experiment is given as a reference. As before, from the PIV mean velocity fields, we can obtain the length of the mean recirculation bubble L_b/D . Table B.1 shows the base pressure coefficient, mean and fluctuating drag, lift and recirculation bubble length for each case.

From all of the above data, we can make several observations. Firstly, the recirculation bubble is increased in streamwise length in each case, compared to the natural wake, and correspondingly, the base pressure is higher. Secondly, the height of the wake is strongly

B. TRAILING EDGE FLAP

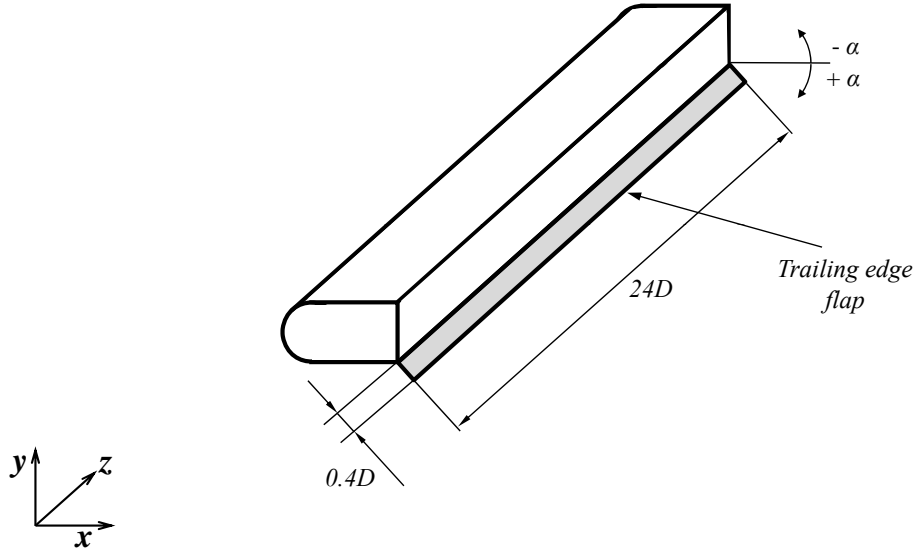


Figure B.1: Experimental setup details with the trailing edge flap attached to the main cylinder.

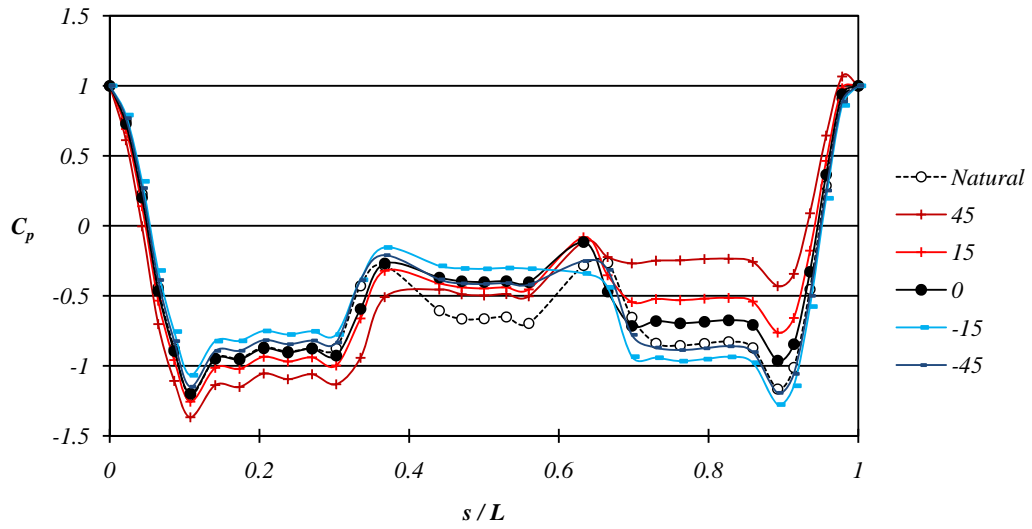


Figure B.2: Pressure coefficient $\overline{C_p}(s)$ distribution around the main cylinder for different angles of the trailing edge flap.

| | <i>Natural</i> | $\alpha = 45^\circ$ | $\alpha = 15^\circ$ | $\alpha = 0^\circ$ | $\alpha = -15^\circ$ | $\alpha = -45^\circ$ |
|------------|----------------|---------------------|---------------------|--------------------|----------------------|----------------------|
| C_{pb} | -0.656 | -0.486 | -0.438 | -0.392 | -0.301 | -0.408 |
| C_x | 0.759 | 0.681 | 0.602 | 0.531 | 0.407 | 0.516 |
| C_{xrms} | 0.0284 | 0.0129 | 0.0113 | 0.008 | 0.007 | 0.009 |
| C_l | -0.03 | 1.40 | 0.61 | 0.19 | -0.52 | -0.22 |
| L_b/D | 0.83 | 1.99 | 1.63 | 1.59 | 1.19 | 1.17 |

Table B.1: Base pressure, aerodynamic coefficients and recirculation bubble lengths for the trailing edge flap at different angles.

modified for the positive angles of the flap, and also the positive lift is substantially increased for these positions. Although the recirculation bubble length is biggest for these cases, the base pressure is not the lowest. Thirdly, the negative angles of the flap are capable of both increasing the length of the bubble, as well as decreasing the height of the wake, which results in the largest increase in base pressure and also in strong reduction of fluctuations of drag. The reduction in fluctuation is expected whenever the recirculation bubble is enlarged, and we can see that in all cases shown here, these fluctuations are reduced compared to the natural case. However, an interesting feature is that when the bubble is not the longest, as is for the case of $\alpha = -15^\circ$, we have the highest base pressure and lowest drag fluctuations. This implies that the amplitude of the global mode is much more damped in this case than in the case of the longest bubble, for $\alpha = 45^\circ$.

Figure B.4 is an extended version of figure 4.29, with added for the $d = 4mm$ circular cylinder (violet circles) and the trailing edge flap marked as yellow squares with "x". As we have seen, the trailing edge flap makes a strong modification of D^* so we have added another version of the data which corresponds to the bubble size being non-dimensionalized by D^* (L_b/D^*), which is marked by green squares with "x". The D^* here is calculated for each angle of the flap as $D^* = D + l_{flap} \sin(\alpha)$. The values for $\alpha = 0^\circ$ and $\alpha = -45^\circ$ are not changed, because they do not modify the initial height of the wake.

A common feature of all the points which lie on the curve of the power law $n = -1.09$, is that their $D^* \approx D$. In other words, the wake modification in these cases is small, or is mostly dedicated to the change of the bubble length, while the height of the bubble remains the height of the bluff cylinder, or very close to it. We can see that the change of the bubble length by the flap is spread across our power law fits, when divided by D . If we divide with an appropriate D^* for each angle of the flap, we obtain the distribution depicted by green squares. The angles for which the D^* changes ($+45^\circ, +15^\circ$ and -15°) give values that are closer to the two power laws, when a correct D^* is used. In the case of $\alpha = -15^\circ$ the D^* is reduced because the flow stays attached on the flap, and the height of the wake is reduced, as can be seen in the corresponding position in figure B.3. This effect on the wake height is very similar to the effect that the *OS* flow configuration has with the $3mm$ circular control cylinder, as can be confirmed in figure 4.13(a) for the *OS* configuration. Hence, this point (green square $\alpha = -15^\circ$)

B. TRAILING EDGE FLAP

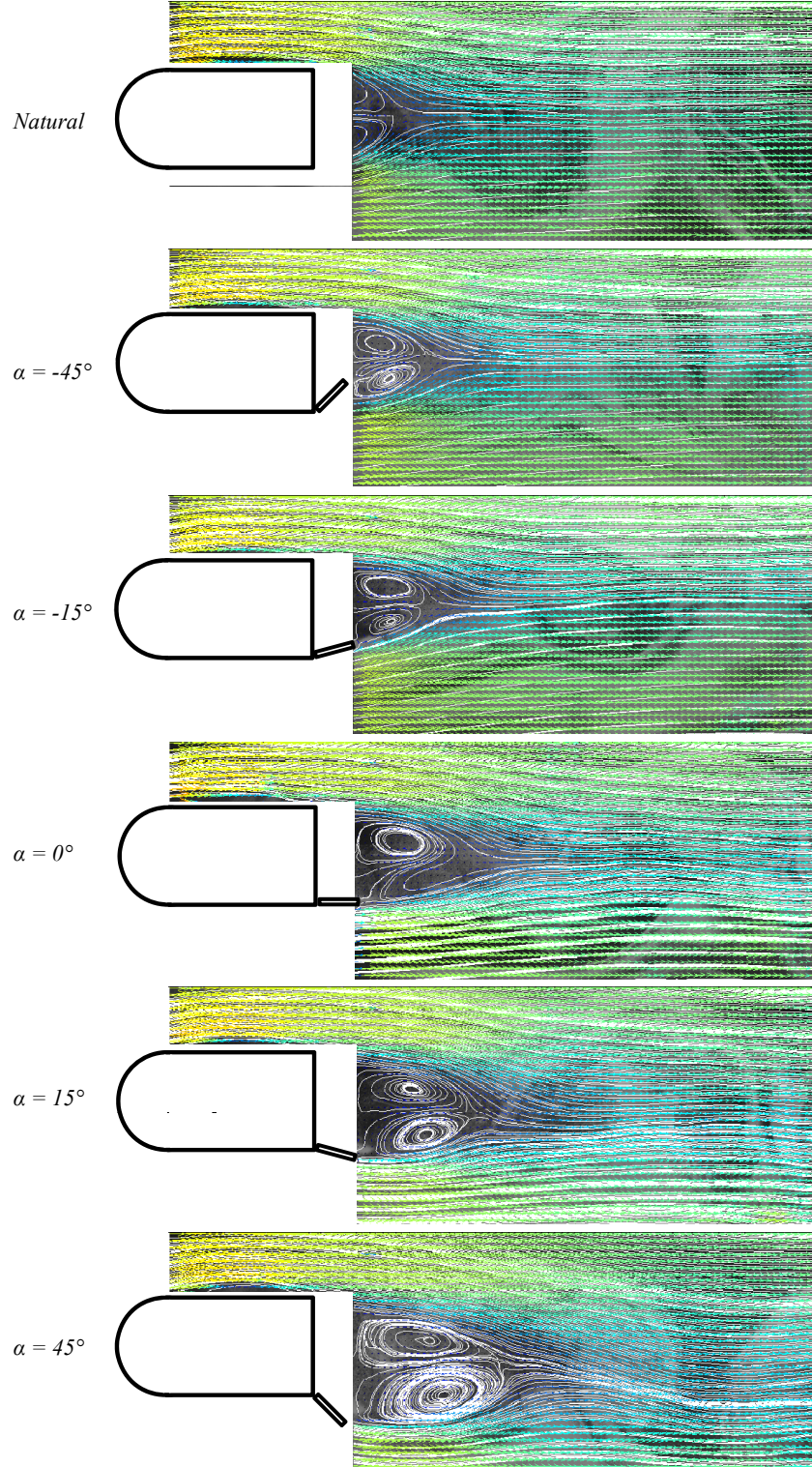


Figure B.3: PIV mean velocity vector fields and streamlines for the trailing edge flap at different angles.

corresponds better with the power law with exponent $n = -0.85$. The values for $\alpha = +15^\circ$ and $\alpha = +45^\circ$ are now closer to the fit $n = -1.09$.

Results for the $d = 4mm$ attached to the control cylinder $x_c/D < 1.2$ follow the $n = -0.85$ power law fit. From the mean streamwise velocity \bar{u} shown in figure 4.18(a), we can see that the bubble is indeed longer and slender (smaller D^*), much like the bubble for the positions of the $3mm$ cylinder, which correspond to the same power law. The second set of results for $4mm$ cylinder at $x_c/D > 1.2$ should perhaps not be commented upon because they are mean results of two very different flow configurations typical of a bi-stable position.

Perhaps we can conclude that the exponent in the power law of the cavity models depends a lot on the wake height. If we could retrieve a correct D^* for each position of the $3mm$ circular control cylinder, we might find a universal power law fit.

B. TRAILING EDGE FLAP

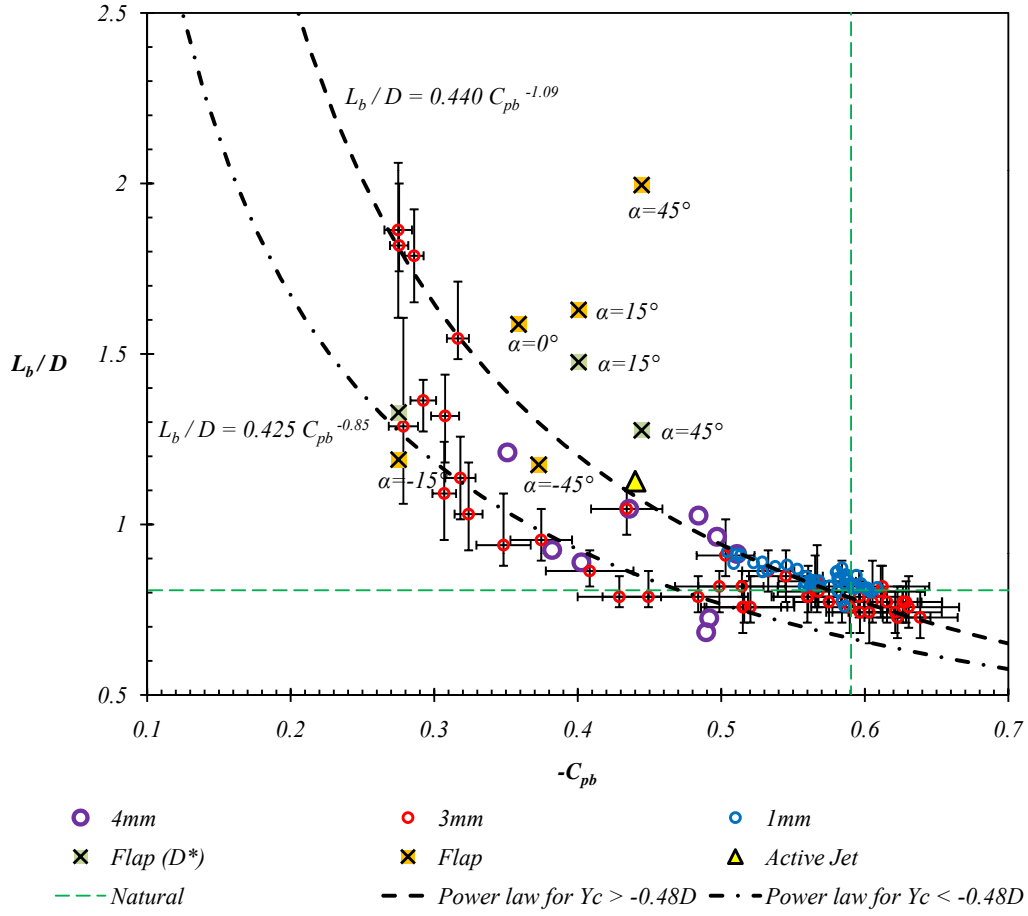


Figure B.4: Results of base pressure as a function of the mean recirculation bubble length, compiled for experiments with 1mm, 3mm and 4mm circular control cylinders, the trailing edge flap and the blowing jet.

Appendix C

End plates

Several attempts of global properties mapping and wake visualization have been made with the end-plates attached to the main cylinder. The objective was to bring our study more into the 2D frame of thought, by reducing the interference of the 3D instabilities.

The positions and shape of the end-plates are shown in figure C.1. The leading edge or front end-plates are a semi-circle of $5D$ in diameter. They have a profiled groove by which they are fitted onto the main cylinder. The trailing or back end-plates are rectangular in shape, with a rectangular opening on one side, which allows them to be fitted to the trailing edge of the main cylinder and also to allow limited control cylinder displacement. The size of the back end-plate is $5D \times 6D$ and they can be placed at $\alpha = 0^\circ$ or $\alpha = 30^\circ$ angles with regard to the xOy plane. The end-plates are made of cardboard, and have a thickness of $2mm$.

In our mapping experiment, only the rear end-plates were fitted, at $\alpha = 0^\circ$ angle. The opening in the back plates, whose dimensions can be seen in the same figure, allowed a limited displacement of the control cylinder, hence the maps in figure C.2 are slightly smaller than the usual. The experiment involved a standard $d = 3mm$ circular control cylinder. As we can see from the sensitivity maps in figure C.2, the structure of the sensitive regions and the envelopes of some global quantities are very different compared to a corresponding $d = 3mm$ experiment without end-plates (see for ex. figure 4.9). The maps of the Strouhal number (figure C.2a) and of the base pressure (figure C.2c) clearly show that the regions where the shear layers can re-attach to the control cylinder are much longer in this wake. The envelope of the Strouhal number is significantly shifted compared to the usual values. It is also much greater since the difference between the maximum and the minimum recorded Strouhal number is $\Delta S_t = 0.118$. The envelope of the base pressure is anchored at the same maximum as usual but the minimal base pressure is much higher, indicating again that the natural state with the end-plates is a much longer recirculation bubble, and higher base pressure. That also implies a lower natural drag. The lift sensitivity map in figure C.2(b) doesn't show any new information, and the base pressure *rms* sensitivity map in figure C.2(d) shows some fluctuation in the near wake,

C. END PLATES

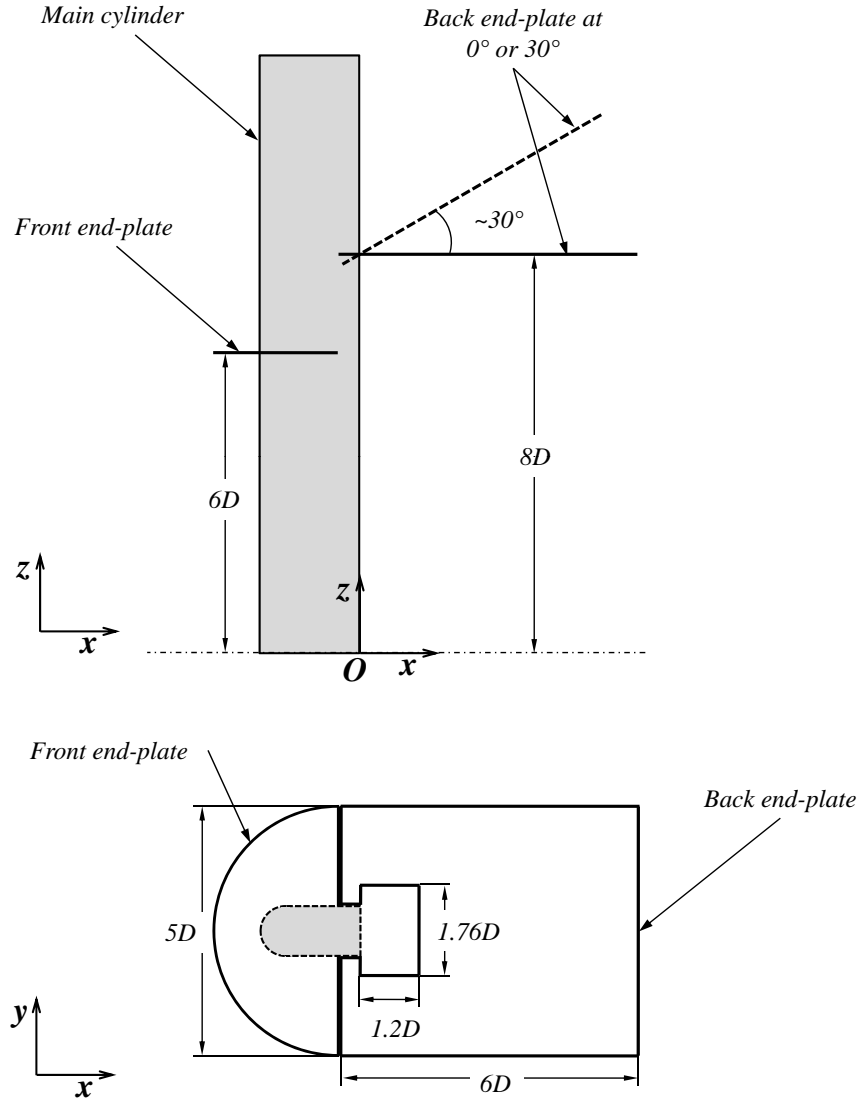


Figure C.1: Disposition and shapes of end-plates used in the experiments.

but generally lower than usual. The fluctuations are probably diminished as a consequence of plates (among other reasons), since they remove the 3D perturbations present in the wake. The regions of slightly higher pressure fluctuations coincide with regions of lowest mean base pressure. This probably means that since the bubble is smallest, the pressure ports at the cylinder base can register some of the fluctuations from the vortex shedding. The fluctuations in the natural wake without the plates are around 0.028, so the maximum of 0.046 in this case is not much greater than the natural value.

Smoke visualization of the wake in xOz plane was performed for two characteristic positions of the control cylinder. Figure C.3 shows the wake behind (a) "clean" main cylinder and (b) cylinder with rear end-plates attached at a $\alpha = \pm 30^\circ$ angle. The control cylinder in both cases is placed at $x_c/D = 0.4$, $y_c/D = -0.46$, which corresponds to an *IS* position for the "clean" bluff cylinder in the main experiment (see chapter 4). The resulting visualization shows dislocations and V-shaped vortex tubes in the "clean" case, and parallel vortex shedding in the case of end-plates. However, the recirculation bubble in the first case is much longer (depicted by a fine dashed line). For the *IS* flow configuration, a large bubble is a common feature, but in this case, the presence of the end-plates are changing the mean flow, and the *IS* configuration is no longer at the same control cylinder positions as before.

Figure C.4 shows four different configurations of the end-plates and their corresponding typical patterns of the wake, for a 3mm control cylinder in *RF* configuration (middle of the wake). As we have seen in chapter 5, when the control cylinder is in this position we observe periodic vortex dislocations, as observable here for the "clean" main cylinder in (a). Placement of front end-plates typically causes inverse V-shaped vortex tubes as in (b). Rear end-plates at $\alpha = 0^\circ$ angle can be very successful in forcing a parallel vortex shedding (c), while when placed at $\alpha = \pm 30^\circ$, as in (d), they cause slight V-shaped bending of the vortex tubes.

We can conclude that the use of the end plates strongly changes the global properties of the wake. This is a consequence of significant modifications to the 3D properties of the wake, as shown in this appendix. However, as much as they might be useful in eliminating 3D components of the flow, the experimental problems they impose far outweighed their usefulness. The reproducibility of these experiments was very low, mostly because of the crude design of the end-plates and their mountings. Improving them wasn't considered worthwhile, since the use of the end-plates significantly limits the movement and mounting of the control cylinder, and makes PIV imaging of the near wake all but impossible due to line-of-sight obstruction.

C. END PLATES

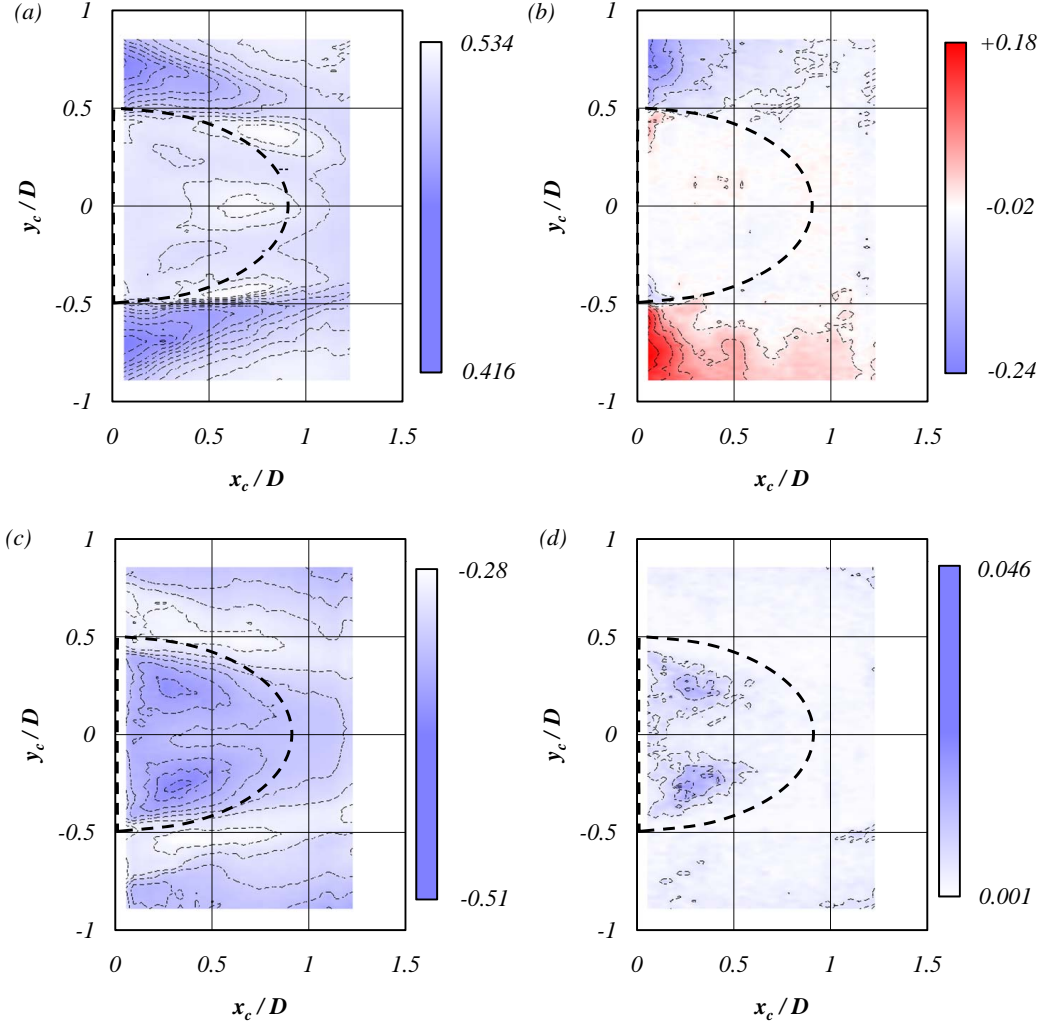
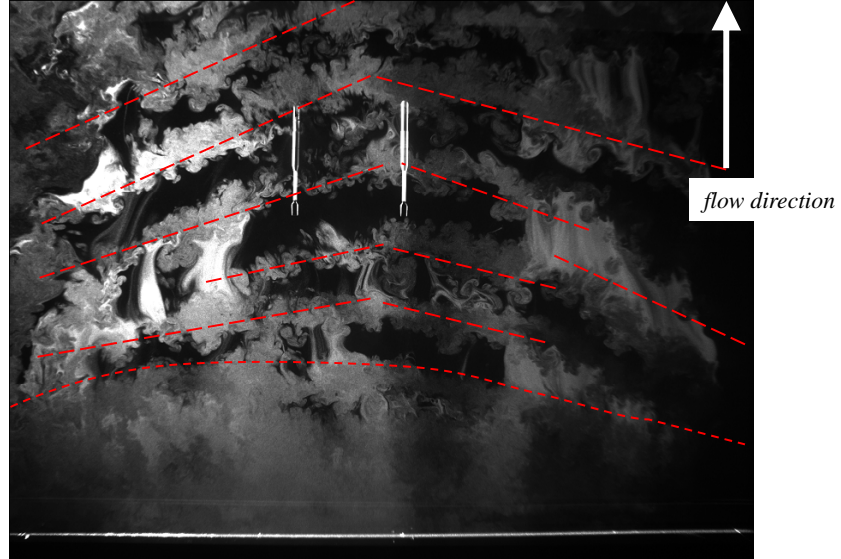


Figure C.2: Sensitivity maps for the 3mm circular control cylinder with the end-plates attached to the main cylinder. (a) Strouhal number St , (b) mean lift coefficient C_l , (c) mean base pressure coefficient C_{pb} and (d) rms of base pressure $C_{pb(rms)}$.

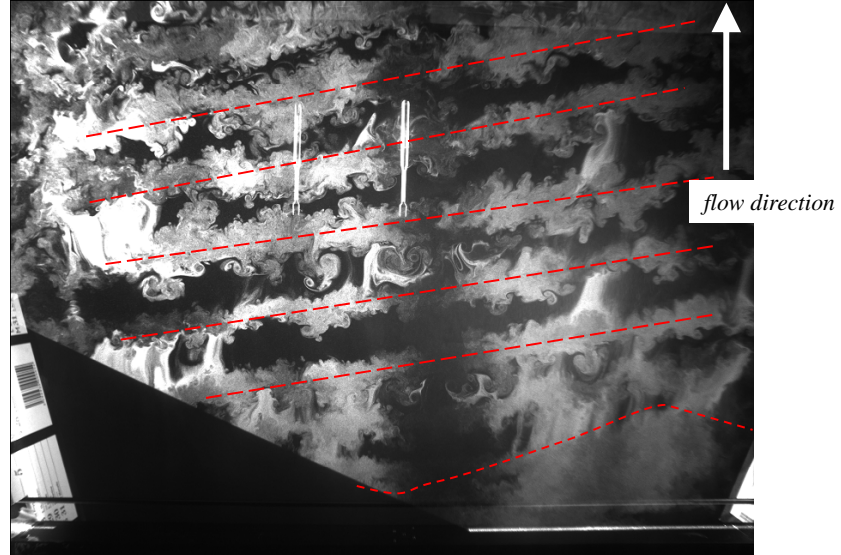
(a)



Clean cylinder



(b)



Angled rear end-plates

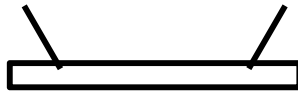


Figure C.3: Visualization of the turbulent wake with a $d = 3mm$ control cylinder in *IS* configuration for (a) "clean" bluff cylinder and (b) bluff cylinder with rear end-plates at $\alpha = \pm 30^\circ$.

C. END PLATES

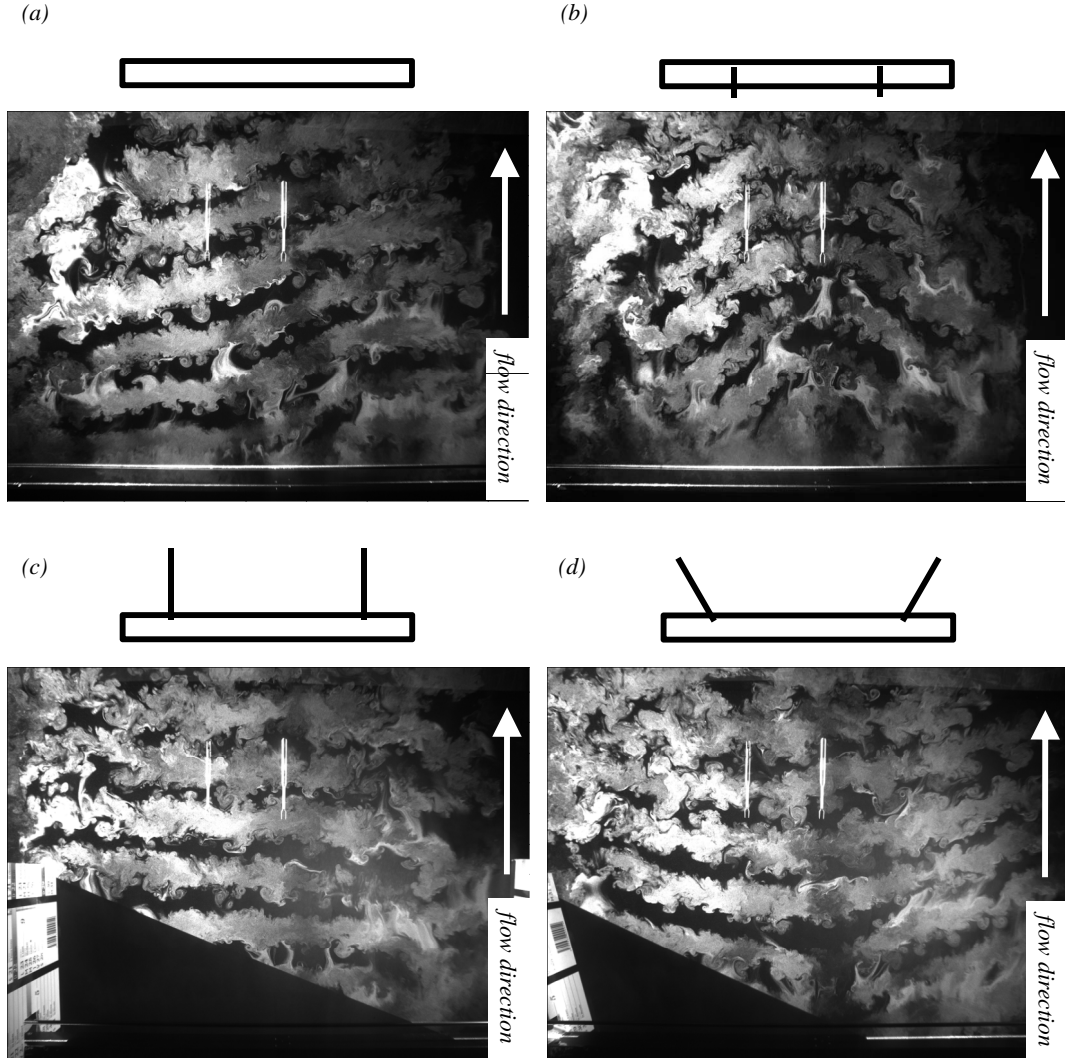


Figure C.4: Visualization of the turbulent wake with a $d = 3\text{mm}$ control cylinder in RF configuration for (a) "clean" bluff cylinder, (b) front end-plates, (c) rear end-plates at $\alpha = 0^\circ$ and (d) rear end-plates at $\alpha = \pm 30^\circ$.

Bibliography

- ADRIAN, R. J. 1991 Particle-imaging techniques for experimental fluid-mechanics. *Ann. Rev. Fluid Mech.* **23**, 261–304. [27](#)
- AHLBORN, B., SETO, M. L. & NOACK, B. R. 2002 On drag, Strouhal number and vortex-street structure. *Fluid Dynamics Research* **30**, 379–399. [10](#)
- APELT, C. J. & WEST, G. S. 1975 The effects of wake splitter plates on bluff-body flow in the range $10^4 \leq R \leq 5 \times 10^4$. Part 2. *J. Fluid Mech.* **71**, 145–160. [10](#), [12](#)
- APELT, C. J., WEST, G. S. & SZEWCZYK, A. A. 1973 The effects of wake splitter plates on the flow past a circular cylinder in the range $10^4 \leq R \leq 5 \times 10^4$. *J. Fluid Mech.* **61**, 187–198. [10](#)
- BATCHELOR, G. K. 1967 *An introduction to fluid dynamics*. Cambridge Univ. Press. [30](#)
- BEARMAN, P. W. 1965 Investigation of the flow behind a two-dimensional model with a blunt trailing edge and fitted with splitter plates. *J. Fluid Mech.* **21**, 241–255. [10](#)
- BENTLEY, J. P. & MUDD, J. W. 2003 Vortex shedding mechanisms in single and dual bluff bodies. *Flow Measurement and Instrumentation* **14** (1-2), 23 – 31. [119](#)
- BLOOR, M. S. 1964 The transition to turbulence in the wake of a circular cylinder. *J. Fluid Mech.* **19**, 290–304. [98](#)
- CADOT, O., THIRIA, B. & BEAUDOIN, J.-F. 2009 Passive drag control of a turbulent wake by local disturbances. In *Unsteady Separated Flows and their Control* (ed. M. Braza & K. Hourigan), pp. 529–537. [17](#)
- CHOMAZ, J.-M. 2005 Global Instabilities in Spatially Developing Flows: Non-Normality and Nonlinearity. *Ann. Rev. Fluid Mech.* **37**, 357–392. [15](#)
- COUAIRON, A. & CHOMAZ, J. M. 1999 Fully nonlinear global modes in slowly varying flows. *Phys. Fluids* **11** (12), 3688–3703. [77](#)
- CROUCH, J. D., GARBARUK, A., MAGIDOV, D. & TRAVIN, A. 2009 Origin of transonic buffet on aerofoils. *J. Fluid Mech.* **628**, 357–369. [15](#)

BIBLIOGRAPHY

- DALTON, C., XU, Y. & OWEN, J. C. 2001 The Suppression of Lift on a Circular Cylinder due to Vortex Shedding at Moderate Reynolds Numbers. *J. Fluid Structures* **15**, 617–628. [13](#)
- FEY, U., KÖNIG, M. & ECKELMANN, H. 1998 A new Strouhal-Reynolds-number relationship for the circular cylinder in the range $47 < Re < 2 \times 10^5$. *Phys. Fluids* **10**, 1547–1549. [10](#), [11](#)
- FRANC, J.-P. & MICHEL, J.-M. 2005 *Fundamentals of Cavitation*. Springer. [81](#)
- GERRARD, J. H. 1966 The mechanics of the formation region of vortices behind bluff bodies. *J. Fluid Mech.* **25**, 401–413. [13](#), [15](#), [72](#), [76](#), [77](#)
- GIANNETTI, F. & LUCHINI, P. 2007 Structural sensitivity of the first instability of the cylinder wake. *J. Fluid Mech.* **581**, 167–197. [15](#), [125](#)
- GOUJON-DURAND, S., JENFFER, P. & WESFREID, J. E. 1994 Downstream evolution of the Bénard–von Kármán instability. *Phys. Rev. E* **50** (1), 308–313. [77](#)
- GROSCHKE, F.-R. & MEIER, G.E.A. 2001 Research at DLR Göttingen on bluff body aerodynamics, drag reduction by wake ventilation and active flow control. *J. Wind Eng. Ind. Aerodyn.* **89** (14-15), 1201 – 1218. [129](#)
- HILL, D. C. 1992 A theoretical approach for analyzing the restabilization of wakes. *NASA Tech. Rep.* **92**, 29394. [15](#)
- IGARASHI, T. & TERACHI, N. 2002 Drag reduction of flat plate normal to airstream by flow control using a rod. *J. Wind Eng. Ind. Aerodyn.* **90** (4-5), 359 – 376. [10](#)
- KIRCHHOFF, G. 1869 Zur theorie freier flüssigkeitsstrahlen. *Journal für die reine und angewandte Mathematik* **70**, 289–298. [9](#)
- KUO, C.-H., CHIOU, L.-C. & CHEN, C.-C. 2007 Wake flow pattern modified by small control cylinders at low Reynolds number. *J. Fluid Structures* **23** (6), 938–956. [13](#), [15](#)
- LEE, S.-J., LEE, S.-I. & PARK, C.-W. 2004 Reducing the drag on a circular cylinder by upstream installation of a small control rod. *Fluid Dynamics Research* **34**, 233–250. [10](#)
- LOMAS, C. G. 1986 *Fundamentals of hot wire anemometry*. Cambridge University Press. [27](#)
- LUCHINI, P., GIANNETTI, F. & PRALITS, J. 2008 Structural sensitivity of linear and nonlinear global modes. In *Proceedings of Fifth AIAA Theoretical Fluid Mechanics Conference, Seattle, Washington, AIAA Paper 2008-4227*. [15](#), [16](#), [125](#)
- LUCHINI, P., GIANNETTI, F. & PRALITS, J. 2009 Structural Sensitivity of the Finite-Amplitude Vortex Shedding Behind a Circular Cylinder. In *Unsteady Separated Flows and their Control* (ed. M. Braza & K. Hourigan), pp. 151–160. [15](#), [125](#)

- MAEKAWA, H. & ABE, S. 2002 Study of vortex dislocations in the wake of a flat plate with finite thickness. *JSME International Journal Series B Fluids and Thermal Engineering* **45** (4), 843–849. [101](#)
- MARQUET, O., SIPP, D. & JACQUIN, L. 2008 Sensitivity analysis and passive control of cylinder flow. *J. Fluid Mech.* **615**, 221–252. [15](#), [125](#)
- MITTAL, S. 2001 Control of Flow Past Bluff Bodies Using Rotating Control Cylinders. *J. Fluid Structures* **15**, 291–326. [13](#)
- MITTAL, S. & RAGHUVANSHI, A. 2001 Control of vortex shedding behind circular cylinder for flows at low Reynolds numbers. *Int. J. Numer. Methods Fluids* **35**, 421–447. [13](#)
- NORBERG, C. 2001 Flow around a circular cylinder: aspects of fluctuating lift. *J. Fluid Structures* **15**, 459–469. [39](#), [98](#)
- PAREZANOVIĆ, V. & CADOT, O. 2009a The impact of a local perturbation on global properties of a turbulent wake. *Phys. Fluids* **21** (7), 071701. [17](#)
- PAREZANOVIĆ, V. & CADOT, O. 2009b Modulated global mode of a controlled wake. In *Advances in Turbulence XII* (ed. B. Eckhardt), pp. 217–220. [17](#)
- PAREZANOVIĆ, V. & CADOT, O. 2011 Experimental sensitivity analysis of the global properties of a 2D turbulent wake. *Submitted to J. Fluid Mech.* . [17](#), [51](#)
- PASTOOR, M., HENNING, L., NOACK, B. R., KING, R. & TADMOR, G. 2008 Feedback shear layer control for bluff body drag reduction. *J. Fluid Mech.* **608**, 161–196. [34](#)
- PERRIN, R., CID, E., CAZIN, S., SEVRAIN, A., BRAZA, M., MORADEI, F. & HARRAN, G. 2007 Phase-averaged measurements of the turbulence properties in the near wake of a circular cylinder at high reynolds number by 2c-piv and 3c-piv. *Experiments in Fluids* **42**, 93–109. [28](#)
- PRALITS, J. O., BRANDT, L. & GIANNETTI, F. 2010 Instability and sensitivity of the flow around a rotating circular cylinder. *J. Fluid Mech.* **650**, 513–536. [15](#)
- PRASAD, A. & WILLIAMSON, C. 1997 A method for the reduction of bluff body drag. *J. Wind Eng. Ind. Aerodyn.* **69-71** (0), 155 – 167. [10](#)
- PRASAD, A. & WILLIAMSON, C. H. K. 1997 Three-dimensional effects in turbulent bluff-body wakes. *J. Fluid Mech.* **343**, 235–265. [39](#), [98](#)
- RIABOUCHINSKY, D. 1921 On steady fluid motion with free surfaces. *Proc. London Math. Soc.* pp. 206–215. [9](#)
- ROSHKO, A. 1954a On the development of turbulent wakes from vortex streets. *Technical Report TN 1191, NACA* . [10](#)

BIBLIOGRAPHY

- ROSHKO, A. 1954*b* On the drag and shedding frequency of two-dimensional bluff bodies. *Technical Report TN 3619, NACA* . [10](#), [13](#), [15](#), [72](#)
- ROSHKO, A. 1993 Perspectives on bluff body aerodynamics. *J. Wind Eng. Ind. Aerodyn.* **49** (1-3), 79 – 100. [10](#), [11](#)
- ROWE, A., FRY, A. L. A. & MOTALLEBI, F. 2001 Influence of Boundary-Layer Thickness on Base Pressure and Vortex Shedding Frequency. *AIAA Journal* **39**, 754–756. [34](#), [114](#)
- SAKAMOTO, H. & HANIU, H. 1994 Optimum suppression of fluid forces acting on circular cylinder. *J. Fluids Eng.* **113**, 183–189. [15](#), [16](#)
- SAKAMOTO, H., HANIU, H. & TAN, K. 1991 An optimum suppression of fluid forces by controlling a shear layer separated from a square prism. *ASME Trans. J. Fluids Eng.* **113**, 183–189. [15](#), [16](#)
- SHAO, C. P. & WEI, Q. D. 2008 Control of Vortex Shedding from a Square Cylinder. *AIAA Journal* **46**, 397–407. [15](#)
- STRYKOWSKI, P. J. & SREENIVASAN, K. R. 1985 The control of transitional flows. In *AIAA Shear Flow Control Conference*, pp. Paper 85–0559. [10](#), [13](#), [15](#), [125](#)
- STRYKOWSKI, P. J. & SREENIVASAN, K. R. 1990 On the formation and suppression of vortex ‘shedding’ at low Reynolds numbers. *J. Fluid Mech.* **218**, 71–107. [10](#), [13](#), [14](#), [15](#), [16](#), [125](#)
- SURYANARAYANA, G. K., PAUER, H. & MEIER, G. E. A. 1993 Bluff-body drag reduction by passive ventilation. *Experiments in Fluids* **16**, 73–81. [129](#)
- THIRIA, B., CADOT, O. & BEAUDOIN, J.-F. 2009 Passive drag control of a blunt trailing edge cylinder. *J. Fluid Structures* **25**, 766–776. [16](#)
- THIRIA, B., GOUJON-DURAND, S. & WESFREID, J. E. 2006 The wake of a cylinder performing rotary oscillations. *J. Fluid Mech.* **560**, 123–147. [77](#)
- THIRIA, B. & WESFREID, J. E. 2007 Stability properties of forced wakes. *J. Fluid Mech.* **579**, 137–161. [77](#)
- TSUTSUI, T. & IGARASHI, T. 2002 Drag reduction of a circular cylinder in an air-stream. *J. Wind Eng. Ind. Aerodyn.* **90** (4-5), 527 – 541. [10](#)
- WILLIAMSON, C. H. K. 1992 The natural and forced formation of spot-like ‘vortex dislocations’ in the transition of a wake. *J. Fluid Mech.* **243**, 393–441. [54](#)
- WILLIAMSON, C. H. K. 1996a Vortex dynamics in the cylinder wake. *Ann. Rev. Fluid Mech.* **28**, 477–539. [39](#)
- WU, T. Y. T. 1972 Cavity and Wake Flows. *Ann. Rev. Fluid Mech.* **4**, 243–284. [79](#), [125](#)

BIBLIOGRAPHY

- YILDIRIM, I., RINDT, C. C. M. & STEENHOVEN, A. A. 2010 Vortex dynamics in a wire-disturbed cylinder wake. *Phys. Fluids* **22** (9), 094101. [13](#)
- ZDRAVKOVICH, M. 1997 *Flow Around Circular Cylinders, Vol. 1: Fundamentals*. Oxford Univ. Press. [10](#)
- ZDRAVKOVICH, M. 2003 *Flow Around Circular Cylinders, Vol. 2: Applications*. Oxford Univ. Press. [10](#)
- ZIELINSKA, B. J. A. & WESFREID, J. E. 1995 On the spatial structure of global modes in wake flow. *Phys. Fluids* **7**, 1418–1424. [16](#), [77](#)